Universidad de Valladolid

Programa de Doctorado en Tecnologías de la Información y las Telecomunicaciones

Tesis Doctoral

Optimized acquisition and estimation techniques in diffusion MRI for quantitative imaging

Presentada por:

Óscar Peña-Nogales

para optar al grado de Doctor por la Universidad de Valladolid

Dirigida por:
Dr. Santiago Aja-Fernández
Dr. Rodrigo de Luis García

Valladolid, España, 2020

Título:
Title:
Optimized acquisition and estimation techniques in diffusion MRI for quantitative imaging

Autor:
Author:
Msc. Óscar Peña-Nogales

Director:
Director:
Dr. Santiago Aja-Fernández

Codirector:
Codirector:
Dr. Rodrigo de Luis García

Departamento:
Department:
Teoría de la Señal Comunicaciones e Ingeniería Telemática

Información de contacto:
Contact information:

✉ **Óscar Peña-Nogales**
Laboratorio de Procesado de Imagen (LPI)
Dept. Teoría de la Señal Comunicaciones e Ingeniería Telemática
ETS. Ingenieros de Telecomunicación
Universidad de Valladolid
Campus Miguel Delibes sn. 47011
Valladolid, Spain
`opennog@lpi.tel.uva.es`
`http://www.lpi.tel.uva.es/opennog`

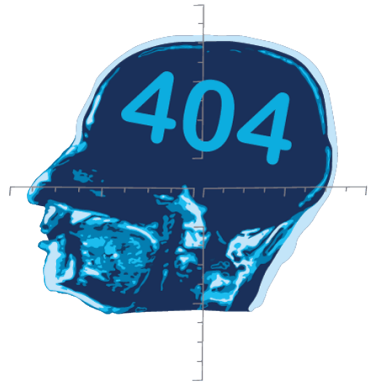

"Oops, ~~Brain~~ Page Not Found!"
ISMRM Error 404 Page

Summary

Diffusion-Weighted Magnetic Resonance Imaging (DW-MRI) is able to measure intrinsic properties of tissue structure non-invasively. By applying diffusion-weighting, DW-MRI is sensitive to microscopic water displacements, with multiple applications for tissue characterization, diagnosis and treatment monitoring. Nevertheless, the application of these long and powerful diffusion-weighting gradients results in compelling imaging challenges. Consequently, this Thesis focuses on the optimization of the Spin Echo (SE) Diffusion-Weighted Imaging (DWI) sequence to improve image quality and estimation of the diffusion-related parametric maps.

As far as image quality is concerned, traditional SE DWI acquisition experiences artefacts from signal dephasing due to bulk motion, Concomitant Gradients (CGs), and Eddy Currents (ECs) which decrease image quality and complicate image interpretation. Additionally, it also suffers from severe signal attenuation due to the long Echo Time (TE) needed to achieve strong diffusion-weightings. Multiple approaches have been proposed to diminish these DWI artefacts, from synchronization, gating and complex DWI sequences such as the Twice Refocused Spin Echo (TRSE) to the application of diffusion-weighting gradients with nth-order motion-nulling and/or EC-nulling. Nevertheless, these techniques generally result in suboptimal acquisitions with long TEs. In this Thesis, we propose a versatile formulation for the design of optimized diffusion-weighting gradient waveforms that alleviates the previous drawbacks while minimizing the TE of the acquisition.

The estimation of the diffusion-related parametric maps is usually affected by several confounding factors such as low accuracy and precision and lack of repeatability and reproducibility, partially caused by the previous artefacts. These confounding factors appear in both the monoexponential and the Intravoxel Incoherent Motion (IVIM) Diffusion-Weighted (DW) signal models, and hinder the establishment of their diffusion-related parametric maps as quantitative imaging biomarkers. Accuracy of the estimates, particularly of the Apparent Diffusion Coefficient (ADC) of the monoexponential DW signal model, can be increased by using the appropriate estimator. However, the set of diffusion-weightings (i.e., set of b-values) that increases the precision of the estimated parametric maps remains unclear. In this Thesis, we derive the Cramér-Rao Lower Bound (CRLB) of both DW signal models under the assumption of DW to be affected by Rician distributed noise, and propose a formulation for the optimization of the set of b-values that maximizes the noise performance (i.e., minimizes the variance and maximizes the precision) of the estimated diffusion-related parametric maps.

Resumen

La resonancia magnética de difusión (DW-MRI, es sus siglas en inglés) es una modalidad de imagen médica capaz de medir las propiedades intrínsecas de la estructura de los tejidos de forma no invasiva. A través de una ponderación en difusión, la DW-MRI es sensible a los desplazamientos microscópicos de agua, lo que la dota de múltiples aplicaciones tanto para la caracterización de los tejidos como para el diagnóstico y el seguimiento de tratamientos. No obstante, la aplicación de los gradientes necesarios para realizar la ponderación de la difusión (muy potentes y duraderos) da lugar a problemas en las imágenes adquiridas. Por consiguiente, esta tesis se centra en la optimización de las secuencias de DW-MRI basadas en adquisiciones *spin-echo* (SE) para mejorar la calidad de las imágenes de difusión y la estimación de los mapas paramétricos relacionados con la difusión.

En lo que respecta a la calidad de la imagen, la secuencia tradicional de DW-MRI basada en SE experimenta considerables artefactos de desfase de la señal debido al movimiento, a los gradientes concomitantes y a las corrientes de Foucault, lo que disminuye la calidad de las imágenes adquiridas y complica su interpretación. Además, las imágenes también sufren de una severa atenuación de la señal debido al largo tiempo necesario para lograr las fuertes ponderaciones de difusión, es decir, necesita de largos tiempos de eco (TE). Se han propuesto múltiples enfoques para disminuir los anteriores artefactos de la DW-MRI. Por ejemplo, se han utilizado desde técnicas de sincronización, y secuencias complejas de DW-MRI como la secuencia SE con doble reenfoque, hasta la aplicación de gradientes de ponderación de la difusión con anulación de movimiento de orden n-ésimo y/o anulación de las corrientes de Foucault. Sin embargo, estas técnicas generalmente dan como resultado adquisiciones subóptimas con largos TEs. En esta tesis, proponemos una formulación versátil para el diseño de formas de onda para los gradientes de ponderación de la difusión optimizadas que disminuyan los problemas anteriormente mencionados de las adquisiciones y las imágenes de DW-MRI y al mismo tiempo minimicen el TE de la adquisición.

Por otro lado, la estimación de los mapas paramétricos relacionados con la difusión suele verse afectada por varios factores perjudiciales como son la baja precisión y baja exactitud, la falta de repetibilidad y falta de reproducibilidad, causados, en parte, por los artefactos descritos anteriormente. Estos factores perjudiciales aparecen tanto en los mapas de difusión estimados a partir del modelo monoexponencial de señal como en los mapas estimados a partir del modelo de movimiento incoherente intravoxel, lo que dificulta el establecimiento de biomarcadores cuantitativos a partir de los mapas paramétricos estimados. La precisión de las estimaciones, y

en particular la precisión de los mapas de difusión aparente del modelo de señal monoexponencial de DW-MRI, puede aumentarse utilizando el estimador apropiado. Sin embargo, el conjunto de ponderaciones de la difusión a realizar (es decir, el conjunto de valores b) que aumentan la precisión de los mapas paramétricos estimados sigue sin estar claro. En esta Tesis se deriva la cota inferior de Cramér-Rao de ambos modelos de señal de DW-MRI bajo el supuesto de que las imágenes adquiridas de DW-MRI se ven afectadas por un ruido con distribución Rician y a su vez se propone una formulación para la optimización del conjunto de valores b que maximizan el nivel de señal (es decir, minimizan la varianza y maximizan la precisión) de los mapas paramétricos estimados relacionados con la difusión.

Acknowledgements

I would like to thank all the people that have helped me during the process of accomplishing this Thesis dissertation. Firstly, I would like to start with my advisors Santiago Aja and Rodrigo de Luis for their advice and the multiple opportunities they gave during all this time. Their advice and support unquestionably helped and pushed me to successfully complete this work.

Secondly, I must devote a few lines to the other advisors I have had during my abroad experiences. I must particularly mention Dr. Diego Hernando for his kindness and encouragement that led me and my work to my first international congress and first international journal publication. After that kick-off experiences I certainly say that my work progressed smoothly achieving plenty of milestones. In these lines I also want to recognize the support received by all the colleagues of these international groups, for making the experience abroad more extraordinary.

Thirdly, I would also like to acknowledge my sponsor the Consejería de Educación of Junta de Castilla y León and the Fondo Social Europeo for my predoctoral grant, the Universidad of Valladolid for the facilities and the access to the MR scanner, and the different institutions I have collaborated with for providing my with access to their MR scanners and with data.

Fourthly, I want to express my endless gratitude to all the staff that has been at the Laboratorio de Procesado de Imagen during these years. I like to remember the *long* shifts, the mutual support and help and, last but not least, the *few* beers and nights out we have definitively enjoyed together. I notably need to mention everyone that has been working at the lab as well as at the Zulo. Some of these are Javi, Rosa, Iñaki, Álvaro, Carlos, Susana and Alex. I need to pinpoint 13, Santi, Elena and Elisa for the shared laughters and the best memories.

A su vez, me gustaría expresar mis más sinceros agradecimients a mis padres, hermana, abuela, Elisa y demás familia. Por todas las veces que me han preguntado que a qué me dedico y qué cuando voy a buscar un trabajo de verdad. Por último, quisiera dar las gracias a toda esa gente de Valdeande, Aranda, Valladolid y del Erasmus por, simplemente, estar ahí.

Thank you all very much,

Óscar

Acronyms

This section lists (in alphabetic order) all the acronyms that have been used in this Thesis dissertation.

ADC Apparent Diffusion Coefficient

CG Concomitant Gradient

CGs Concomitant Gradients

CHESS Chemical Shift Selective

CODE Convex Optimized Diffusion Encoding

CPMG Carr-Purcell-Meiboom-Gill

CRLB Cramér-Rao Lower Bound

CT Computerized Tomography

DFT Discrete Fourier Transform

DKI Diffusion Kurtosis imaging

DTI Diffusion Tensor Imaging

DW Diffusion-Weighted

DW-MRI Diffusion-Weighted Magnetic Resonance Imaging

DWI Diffusion-Weighted Imaging

EC Eddy Current

ECs Eddy Currents

EP Error Propagation

EPI Echo Planar Imaging

FID Free Induction Decay

FIM Fisher Information Matrix

FOV Field-of-View

FT Fourier Transform

GRAPPA Generalized Autocalibrating Partially Parallel Acquisition

GRE Gradient Echo

IQR Interquartile Range

IR Inversion Recovery

IRB Institutional Review Board

IVIM Intravoxel Incoherent Motion

LS Least Squares

ML Maximum Likelihood

MOCO Motion-Compensated

MONO Monopolar

MR Magnetic Resonance

MRI Magnetic Resonance Imaging

ms-EPI multishot Echo Planar Imaging

MSD Mean Squared Displacement

NMR Nuclear Magnetic Resonance

ODGD Optimized Diffusion-weighting Gradient Waveform Design

PD Proton Density

PDF Probability Density Function

PET Positron Emission Tomography

PGSE Pulse Gradient Spin Echo

PI Parallel Imaging

PNS Peripheral Nerve Stimulation

RF Radio-Frequency

ROI Region of Interest

SE Spin Echo

SE-EPI Spin Echo Echo Planar Imaging

SENSE Sensitivity Encoding

SNR Signal-to-Noise-Ratio

SQP Sequential Quadratic Programming

ss-EPI single shot Echo Planar Imaging

STE Stimulated Echo

STEAM Stimulated Echo Acquisition Mode

SWI Susceptibility-Weighted Imaging

TE Echo Time

TR Repetition Time

TRSE Twice Refocused Spin Echo

WLS Weighted Least Squares

Contents

Part I

Background

1 Introduction

Contents

1.1 Motivation

Magnetic Resonance Imaging (MRI) is a powerful medical image modality used to obtain images of a broad range of tissues and properties. It is based on the combined application of a strong magnetic field with Radio-Frequency (RF) pulses and magnetic field gradients, which make it genuinely versatile and sensitive to a wide variety of tissue properties and characteristics. During the past decades MRI has become a conventional image modality in the medical routine due to its physical foundations, which make it a non-invasive, innocuous and harmless image modality in comparison to other techniques such as Computerized Tomography (CT). However, MRI also presents various disadvantages. Particularly, it is a slow technique, and really sensitive to artefacts.

Within the realm of MRI we can probe different physical and physiological phenomena that exist in biological tissues depending on the sequence applied. These

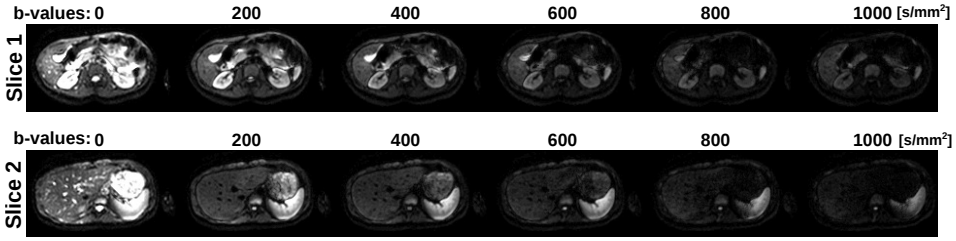

Figure 1.1: Example of two slices of body diffusion-weighted images at b-values of [0, 200, 400, 600, 800, 1000] s/mm^2.

sequences are a particular combination of the aforementioned RF pulses and magnetic field gradients to obtain an image. Generally grouped by their image modality, T_1-weighted or T_2-weighted MRI, Susceptibility Imaging, Magnetic Resonance Tagging, CINE MRI or Diffusion-Weighted Magnetic Resonance Imaging (DW-MRI) are some of the modalities with more distinct clinical applications. DW-MRI or Diffusion-Weighted Imaging (DWI) is a particularly valuable modality due to its sensitivity to the microscopical motion of diffusing water throughout the tissues. The DWI sequence was initially proposed in 1965 by Stejskal and Tanner (Stejskal and Tanner, 1965). It is based on the application of a 90° excitation RF pulse and a 180º inversion RF pulse interleaved with two strong diffusion-weighting magnetic field gradients. This RF pulse configuration is named Spin Echo (SE) since the measured signal is generated by the refocusing of the spins after the 180° inversion. On the other hand, the gradients describe the sensitivity to diffusion in a term named b-value and encode the phase of stationary and moving spins resulting in a signal dephase proportional to the overall motion. Besides its apparent simplicity, it was not until 1985 that the first diffusion-weighted images of a brain were obtained by Dennis le Bihan with a 0.5T MRI (Le Bihan and Breton, 1985), with maximum gradient strengths of 10 mT/m, b-values up to 200 s/mm^2 and a standard SE sequence which took close to 10 min to acquire a single b-value (Le Bihan, 2007a). At the beginning, it had little appeal due to its slowness and extreme sensitivity to motion artefacts. However, due to the MRI hardware advancement and sequence development in the past 35 years, DWI has become one of the most reliable MRI techniques in the clinical routine. Nowadays, a standard clinically-available MRI scanner can have a static magnetic field of 3T, a maximum gradient strength between 40 and 70 mT/m, achievable b-values up to several thousand s/mm^2 and scanning times close to 100 ms per b-value. An example of liver diffusion-weighted images at various b-values is shown in Figure 1.1.

During this time, DWI has continuously proved to be able to facilitate diagnosis, characterization and monitoring of multiple pathologies all over the human body. Head, liver, breast and prostate are some commonplace target tissues and stroke, hepatic metastasis, and prostate cancer are some example pathologies. Nevertheless, further pathologies and more detailed explanations of DWI applications are described later in Section 2.3.

During the past three decades the applications of MRI, and particularly of DWI,

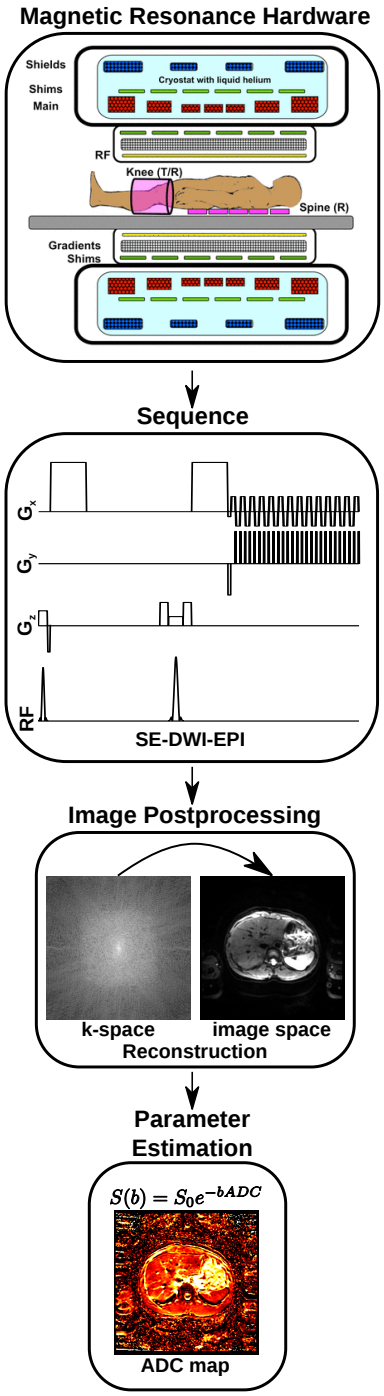

Figure 1.2: Magnetic resonance imaging (MRI) pipeline. Magnetic Resonance (MR) Hardware, image acquisition sequence, postprocessing and quantitative parameter estimation. (*MRI cross-sectional scanner figure was courtesy of Allen D. Elster, MRIquestions.com.*)

have been multiplied by thousands as shown in previous paragraphs due to the continuous advancements in each of the different elements involved in the acquisition and image interpretation pipelines. These elements can be divided into:

1. MRI hardware.
2. Sequence acquisitions.
3. Image postprocessing.
4. Parameter estimation.

A graphical depiction of this idea is shown in Figure 1.2. The advancement of DWI-related hardware (1) has made it possible to increase the diffusion-weighting within reasonable scanning times. The development of new sequence acquisitions (2) have considerably reduced the scanning time per image. The improvement of the image postprocessing methods (3) has increased image quality facilitating image interpretation, and has paved the way towards novel image perceptions. Finally, the creation of advanced signal models together with the development of new estimation methods (4) have expanded the possibilities for diagnosis, characterization and treatment monitoring of a vast number of pathologies. This has been possible due to the estimation of new parameters that attain some remarkable properties that make them suitable to be used as biomarkers.

On the one hand, an imaging biomarker is a biologic qualitative feature detectable in an image that is relevant to establish the presence or severity of a disease (Smith et al., 2003). On the other hand, with quantitative imaging biomarkers we refer to "the extraction of quantifiable features from medical images for the assessment of normal or the severity, degree of change, or status of a disease, injury, or chronic condition relative to normal. Quantitative imaging includes the development, standardization, and optimization of anatomical, functional, and molecular imaging acquisition protocols, data analyses, display methods, and reporting structures. These features permit the validation of accurately and precisely obtained image-derived metrics with anatomically and physiologically relevant parameters, including treatment response and outcome, and the use of such metrics in research and patient care." (Buckler et al., 2011).

Thus, a quantitative imaging biomarker is an objectively measurable characteristic of the tissue. Note that not all the measures taken from medical imaging can be used as quantitative biomarkers. To be valid, they must fulfill the following requirements:

1. Precise: the measurement must be repeatable for the same subject and within subjects in the same session and between sessions.
2. Accurate: in terms of estimation theory, it means that the bias of the estimation is small.
3. Reproducible: low variability across sites and platforms. This is critically important for multi-center studies.

4. Robust: the measurement is insensitive to platform scan parameters and to the estimation algorithm.

5. Clinical utility: the measurement can only be considered a quantitative imaging biomarker if it demonstrates an important role in diagnosis or treatment monitoring. To become so, it must be submitted to clinical validation. This clinical utility also means that a new quantitative imaging biomarker must imply a measurable clinical improvement.

In a more practical way, a quantitative imaging biomarker needs to be obtained at the lowest possible costs (low-priced) and in the shortest time (fast), and it must be safe and harmless to the patient. The main limitations of medical image measurements that can interfere with the definition of possible quantitative imaging biomarker are:

1. Long acquisition times and complexity: we usually need to acquire multiple images, with very complex and specific acquisition processes.

2. Limited spatial and temporal resolution: there are limitations basically due to the scanning hardware, physical properties, and the allotted scanning time per subject.

3. Presence of confounding factors: there are some acquisition factors (such as noise, patient motion, image artefacts) that will introduce systematic error in the parametric estimates. These factors must be studied and taken into account in order to reduce the variability of a measure to make it accurate, robust and repeatable, and thus make it feasible to be used as a quantitative imaging biomarker.

At the beginning of this chapter we mentioned that the first images that gave birth to DWI were brain images and were acquired by Le Bihan and Breton (1985), however, as he mentions in his historical account (Le Bihan, 2007a) the original target tissue in which everything started was the liver in 1984. Due to the difficulty of Diffusion-Weighted (DW) liver imaging, he eventually gave up and switched to the brain. Since then, DWI has greatly evolved and it is nowadays successfully applied to any tissue. Nevertheless, in order to obtain quantitative imaging biomarkers from DW liver imaging multiple artefacts, limitations and pitfalls still need to be addressed and diminished. Some of these are motion, Concomitant Gradients (CGs), and Eddy Currents (ECs), which generally appear simultaneously. In general, they may cause signal dephasing, image ghosting, signal attenuation, shine-through effects, image distortions (i.e., shifting, shearing, scaling, blurring), bias and variance on the quantitative diffusion-related parametric maps, and even patient discomfort. A detailed explanation of these effects along with their causes is provided in Section 2.4. Consequently, DWI is in no way a direct and simple image acquisition technique, making it difficult to find diffusion descriptors that can be used as quantitative imaging biomarkers. This is precisely the purpose of the present Thesis.

1.2 Objectives

The main objective of this Thesis is to **optimize acquisition and estimation techniques for liver Diffusion-Weighted Imaging (DWI) that may grant viable quantitative imaging biomarker computation in the clinical routine. Specifically, we will focus on (a) the improvement of DW image quality by maximizing the signal intensity while reducing physical and physiological confounding factors affecting the DW images and on (b) the precise estimation of the diffusion-related parametric maps.**

The main objective can be break down into the following individual objectives:

1. To develop a formulation for the optimization of the diffusion-weighting gradient waveforms of spin-echo DWI to improve DW image quality. The proposed formulation will maximize the Signal-to-Noise-Ratio (SNR) of DWI acquisitions for a given b-value while diminishing motion-related artefacts and Concomitant Gradient (CG) effects. The formulation will be based on the natural b-value definition while considering the physics of other physical and physiological effects.

2. To extend previous formulation for the design of optimized diffusion-weighting gradient waveforms of SE DWI to improve DW image quality with the purpose of diminishing Eddy Current (EC) artefacts and Peripheral Nerve Stimulation (PNS) effects while preserving all previous properties.

3. To develop a formulation for the determination of the optimized set of b-values that maximizes the noise performance (i.e., maximizes the precision and minimizes the variance) of the Apparent Diffusion Coefficient (ADC) maps of the monoexponential diffusion signal model of liver DWI, and to establish a methodology towards their quick determination. The formulation will be based on the minimization of the Cramér-Rao Lower Bound (CRLB) of the estimator and the methodology will rest on the optimized b-value convergence properties.

4. To adapt the previous formulation for the determination of the optimized set of b-values that maximizes the noise performance (i.e., maximizes the precision and minimizes the variance) of the Intravoxel Incoherent Motion (IVIM) diffusion-related parametric maps (i.e., pseudodiffusion, diffusion, and pseudodiffusion fraction) in liver DWI.

The first two objectives pursue the optimization of DWI acquisition to pave the way towards the computation of quantitative imaging biomarkers, while the last two objectives pursue the computation of precise measures that fulfill the requirements to be considered as quantitative imaging biomarkers for their respective signal models.

As a final remark, it must be noted that the qualitative and quantitative validation of each of the previous formulations is, in many cases, a challenging task which could be an objective by itself.

1.3 Methodology

In this Thesis we adopt a post-positivism worldview, which is is turn an evolution of the positivism worldview. In post-positivism, the ethical principles that guide research are based on good conduct and good research, and it is assumed that, although reality exists, it can only be known in a flawly manner and upon a probability basis. Thus, theories and hypotheses exist, but they can be imperfect and may bias researchers. In this context, the methodology of this Thesis is based on the engineering research method initially described by Adrion (1993) and later refined by Glass (1995). The engineering method consists in observing existing solutions, proposing a better solution and developing it to subsequently measure, analyse and repeat until no further improvements are possible. The particular steps followed throughout this Thesis can be described as follows:

The informational phase consists in observing the state-of-the-art solutions of a given problem via a literature survey. From the five steps of the image acquisition pipeline described in Section 1.1 we detected the multiple artefact sources and technique limitations that hinder the extraction of biomarkers based on DWI. Thus, we decided to pay further attention to the acquisition and estimation steps because vital work could be done on DW sequence design in favor of image quality and parameter estimation. Existing solutions to reduce motion artefacts were based on triggering, which considerably increases the acquisition time, and on motion-compensated diffusion-weighting gradient waveforms, which typically result in longer Echo Time (TE). With regard to other physical and physiological effects such as concomitant gradients or eddy currents, correction methods were based on both complex and frequently longer sequences and on postprocessing techniques that do not account for intravoxel dephasing. On the other hand, proposed techniques of sequence optimization for precise parameter estimation often rely on inaccurate noise assumptions or require long computation times.

The propositional phase consists in proposing a hypothesis or a method, or formulating an algorithm or a theory. We proposed to increase diffusion-weighted image quality, reduce motion artefacts, concomitant gradient artefacts, eddy current induced image distortions and peripheral nerve stimulation through the design of optimized diffusion-weighting gradient waveforms. The application of these optimized gradients may allow reductions of some of the artefacts at the source without triggering, thus overcoming some of the limitations of state-of-the-art methods. In order to increase the precision of the diffusion-related parametric maps we proposed to optimize the set of diffusion-weightings (i.e., set of b-values) that minimizes the variance and increases the noise performance in parameter mapping.

The analytical phase consists in analysing and exploring a proposition. Regarding DWI sequence optimization the proposition was materialized with the design of a constraint nonlinear formulation based on the pure b-value mathematical expression to design optimized diffusion-weighting gradient waveforms. The optimized gradients depend on linear and nonlinear constraints while iteratively minimize the TE for a given b-value to increase SNR. For instance, a linear constraint is

included to achieve moment-nulling and to reduce motion artefacts, a nonlinear constraint is included to achieve phase cancelation at both sides of the inversion pulse to reduce concomitant gradients, and a linear constraint is included to cancel out remanent gradient fields and diminish image distortions due to eddy currents. As for the optimization of parameter estimation to obtain precise parametric maps, the optimized set of diffusion-weightings (i.e., set of b-values) is obtained using the CRLB under the assumption diffusion-weighted images polluted with Rician distributed data.

The evaluative phase consists in evaluating a proposition through experimentation. The proposed and implemented formulations were validated through simulations, phantom experiments and in-vivo acquisitions.

- Simulations were performed on synthetic datasets in order to have ground truth images to compare the results with, and to deduce the relative performance of each formulation.
- Phantom experiments were carried out in order to have real acquisitions in a controlled environment. These images show to what extent the confounding factor is present, and how much it can be diminished. Further, these acquisitions pave the way for the design of in-vivo acquisitions.
- In-vivo acquisitions of the brain and the liver of various volunteers were used to clinically validate the performance of both formulations.

In addition, throughout the progress of this Thesis we have carried out an additional phase known as the **dissemination phase**. In this last phase we shared with the community our motivation, final propositions, methods, and results with a thorough comparison with the state-of-the-art. This dissemination was done for the research community on specialized international journals and conferences and on regional non-specialized journals for the local community.

1.4 Materials: MRI scanners

To prove the validity of the proposed formulations throughout this Thesis, all the experiments were carried out with acquisitions performed in various MR scanners from three different vendors and with two different external magnetic field B_0 intensities. These scanners are described next:

- MR 750
  - Institution: University of Wisconsin-Madison, Wisconsin, USA
  - **GE Healthcare**, Waukesha, Wisconsin, USA
  - Nominal B_0: **3T**
  - Maximum Gradient Strength: 50 mT/m
  - Maximum Slew Rate: 200 T/m/s

- Signa Premier
  - Institution: University of Wisconsin-Madison, Wisconsin, USA
  - **GE Healthcare**, Waukesha, Wisconsin, USA
  - Nominal B_0: **3T**
  - Maximum Gradient Strength: 70 mT/m
  - Maximum Slew Rate: 150 T/m/s/axis
- Achieva 3T
  - Institution: Universidad de Valladolid, Valladolid, Spain
  - **Philips Healthcare**, Best, The Netherlands
  - Nominal B_0: **3T**
  - Maximum Gradient Strength: 80 mT/m
  - Maximum Slew Rate: 200 T/m/s
- Signa HDxt 1.5T
  - Institution: University of Wisconsin-Madison, Wisconsin, USA
  - **GE Healthcare**, Waukesha, Wisconsin, USA
  - Nominal B_0: **1.5T**
  - Maximum Gradient Strength: 33 mT/m
  - Maximum Slew Rate: 120 T/m/s
- Aera 1.5T
  - Institution: Universidade de Lisboa, Lisbon, Portugal
  - **Siemens**, Erlangen, Germany
  - Nominal B_0: **1.5T**
  - Maximum Gradient Strength: 43 mT/m
  - Maximum Slew Rate: 180 T/m/s

1.5 List of Publications

Below we include a list of publications related to this thesis, which is also shown as a diagram in Figure 1.3. Each contribution is related with one of the aforementioned objectives although more than one publication can be related with the same objective.

- Core publications of this Thesis:
  - Publications in indexed international journals

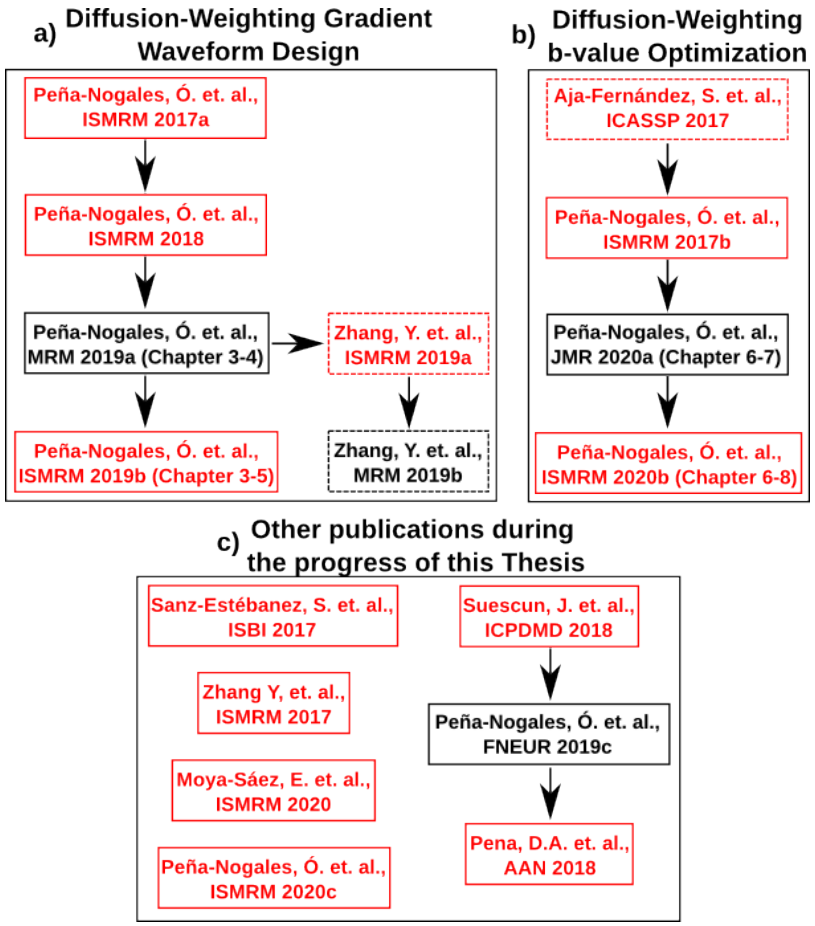

Figure 1.3: Relation between each of the contributions related to this Thesis grouped by the two major objectives (a) and b)) and other publications carried out during this PhD (c). In each contribution related to this Thesis we tackle an individual objective and the chapter indicates its location within this Thesis dissertation. Some contributions do not form a chapter by themselves thus they are contained within the next corresponding journal contributions. Dashed lines indicate contributions of another author that are in line with our work on both diffusion-weighting gradient waveform design and b-value optimization. As such, they are not included in this Thesis. The red-color publications were published on international conferences while black-color publications were published on international journals.

- **Peña-Nogales, Ó.**, Zhang, Y., Wang, X., de Luis-Garcia, R., Aja-Fernández, S., Holmes, J.H. and Hernando, D. Optimized Diffusion-Weighting Gradient Waveform Design (ODGD) formulation for motion compensation and concomitant gradient nulling. *Magnetic resonance in medicine*. 2019a; 81(2), 989-1003.

- **Peña-Nogales, Ó.**, Hernando, D., Aja-Fernández, S. and de Luis-Garcia, R. Determination of optimized set of b-values for Apparent Diffusion Coefficient mapping in liver Diffusion-Weighted MRI. *Journal of Magnetic Resonance*. 2020a; 310, 106634.

◦ Publications in international conferences

- **Peña-Nogales, Ó.**, de Luis-García, R., Aja-Fernández, Zhang, Y., S., Holmes, J.H. and Hernando, D. Optimal design of motion-compensated diffusion gradient waveforms. *ISMRM 25th annual Meeting and Exhibition*, Honolulu, USA, April 2017a; 3340.

- **Peña-Nogales, Ó.**, Hernando, D., Aja-Fernández, S. and de Luis-García, R. Determination of the optimal set of b-values for ADC mapping under a Rician noise assumption. *ISMRM 25th annual Meeting and Exhibition*, Honolulu, USA, April 2017b; 3341.

- **Peña-Nogales, Ó.**, Zhang, Y., de Luis-García, R., Aja-Fernández, S., Holmes, J.H. and Hernando, D. Optimal diffusion-weighting Gradient Waveform Design (ODGD): Formulation and Experimental Validation. *ISMRM 26th annual Meeting and Exhibition*, Paris, France, June 2018; 685.

- **Peña-Nogales, Ó.**, Zhang, Y., de Luis-García, R., Aja-Fernández, S., Holmes, J.H. and Hernando, D. Reduced Eddy Current induced image distortions and Peripheral Nerve Stimulation based on the Optimal Diffusion-weighting Gradient Waveform Design (ODGD) formulation. *ISMRM 27th annual Meeting and Exhibition*, Montreal, Canada, May 2019b; 3488.

- **Peña-Nogales, Ó.**, Aja-Fernández, S., and de Luis-García, R. Determination of the optimal set of b-values for Intravoxel Incoherent Motion (IVIM) parameter mapping in liver Diffusion-Weighted MRI. *ISMRM 28th annual Meeting and Exhibition*, Paris, France, August 2020b; 4314.

In the subsequent list we also include other contributions accomplished during the progress of this Thesis. These publications originated from collaborations with colleagues and other international institutions. Although at least some of them are related to the scope of this Thesis, they have been left out for coherence and practical purposes, or because the the author of this Thesis was secondary in some of these publications. Two collaborations have been particularly fruitful:

that with the University of Wisconsin-Madison, WI, USA, and the one with the University of Texas – Health Science Center at Houston, TX, USA, which led to two publications in indexed international journals aiming at the determination of quantitative imaging biomarkers in the liver and the brain, respectively.

- Other publications accomplished during the progress of this Thesis:
  - Publications in indexed international journals
    - Zhang, Y., **Peña-Nogales, Ó.**, Holmes, J.H. and Hernando, D. Motion-Robust and Blood-Suppressed M1-Optimized Diffusion MR Imaging of the Liver. *Magnetic resonance in medicine.* 2019b; 82(1), 302-311.
    - **Peña-Nogales, Ó.**, Ellmore, T.M., de Luis-García, R., Suescun, J., Schiess, M.C. and Giancardo, L. Longitudinal connectomes as a candidate progression marker for prodromal Parkinson's disease. *Frontiers in neuroscience.* 2019c; 12, 967.
  - Publications in international conferences
    - Aja-Fernández, S., **Peña-Nogales, Ó.**, and de Luis-García, R. Effect of the Sampling on the Estimation of the Apparent Diffusion Coefficient of Diffusion in MRI. *42nd IEEE International Conference on Acoustics, Speech and Signal Processing*, New Orleans, USA. March 2017; 2521.
    - Sanz-Estébanez, S., **Peña-Nogales, Ó.**, de Luis-García, R., Aja-Fernández, S., and Alberola-López, C. Groupwise non-rigid registration on multiparametric abdominal DWI acquisition for robust ADC estimation: Comparison with pairwise approaches and different multimodal metrics. *IEEE International Symposium on Biomedical Imaging*, Melbourne, Australia. April 2017; 325.
    - Zhang, Y., **Peña-Nogales, Ó.**, Holmes, J.H. and Hernando, D. Monte-Carlo Analysis of Quantitative Diffusion Measurements Using Motion-Compensated Diffusion Weighting Waveforms. *ISMRM 25th annual Meeting and Exhibition*, Honolulu, USA, April 2017; 1377.
    - Suescun, J., **Peña-Nogales, Ó.**, Ellmore, T.M., de Luis-García, R., Schiess, M.C. and Giancardo, L. Tracking RBD and PD progression with longitudinal structural brain connectomes. *International Congress of Parkinson's Disease and Movement Disorders*, Hong Kong. 2018;
    - Zhang, Y., **Peña-Nogales, Ó.**, Holmes, J.H., and Hernando, D. Motion-Robust and Blood-Suppressed M1-Optimized Diffusion MR Imaging of the Liver. *ISMRM 27th annual Meeting and Exhibition*, Montreal, Canada, May 2019a; 116.

- Pena, D.A., **Peña-Nogales, Ó.**, Ellmore, T.M., de Luis-García, R., Suescun, J., Schiess, M.C. and Giancardo, L. Longitudinal Connectivity Outperforms Volumetric Change As A Marker For Prodromal Parkinson's Disease. *American Academy of Neurology 71st Annual Meeting*, Philadelphia, USA. 2018; 4186.

- Moya-Sáez, E., **Peña-Nogales, Ó.**, Sanz-Estébanez, S., de Luis-García, R., and Alberola-López, C. CNN-based synthesis of T_1, T_2, and PD parametric maps of the brain with a minimal input feeding. *ISMRM 28th annual virtual Meeting and Exhibition*, Paris, France, August 2020; 3806.

- **Peña-Nogales, Ó.**, Castillo-Passi, C., Lizama, C., de Luis-García, R., Aja-Fernández, S., and Irarrazaval, P. Anomalous Diffusion estimation through the solution of the Fractional Time order Bloch-Torrey equation. *ISMRM 28th annual Meeting and Exhibition*, Paris, France, August 2020c; 4398.

1.6 Thesis Overview

In order to best reflect the research work that has resulted in this Thesis dissertation, this document is divided into four Parts. On the one hand, the specific objective of improving DW image quality by maximizing the signal intensity while reducing physical and physiological confounding factors affecting the DW images is tackled in Part II. On the other hand, the objective of achieving precise estimation of the diffusion-related parametric maps is addressed in Part III. Each of these Parts is further divided in three Chapters, the first one introducing and motivating the corresponding problem and the latter two presenting our methodology and solutions. Finally, this Thesis dissertation is further completed with Part I, which acts as a background that introduces the basement of our work, and finishes with Part IV, which introduces some some final remarks and conclusions.

A more detailed description is portrayed next:

- **Part I:** Background, which introduces and motivates this Thesis dissertation.
  - **Chapter 2** contains the background knowledge needed to fully understand the different issues addressed throughout this dissertation. It starts by explaining the principles of Magnetic Resonance Imaging (MRI) and the fundamentals of Diffusion-Weighted Imaging (DWI) together with a brief list of its applications and limitations, and finishes with the elemental knowledge needed to perform parameter estimation.
- **Part II:** This part contains the first contribution of this Thesis dissertation, and focuses on the optimization of DW image quality through the design of diffusion-weighting gradient waveforms. It is divided in the following three chapters:

- **Chapter 3** introduces some of the artefacts and limitations DWI is subjected to due to the lengthy acquisitions, patient motion, Concomitant Gradients (CGs), Eddy Currents (ECs) and the nerve stimulation effects. It shows some procedures to diminish them and the trade-off they pose. Then we provide an extended more theoretical description of previous artefacts and limitations, which acts as the basement of the formulation we propose to tackle them.
- **Chapter 4** focuses on the validation of the proposed formulation to increase the quality of the diffusion-weighted images and of the corresponding diffusion-related parametric maps by reducing the artefacts introduced by the lengthy DWI acquisitions, patient motion, and the CGs. In this Chapter we perform analytical experiments, simulations, and both phantom and in-vivo experiments to assess the proposal.
- **Chapter 5** focuses on the validation of the proposed formulation to increase the quality of the diffusion-weighted images by reducing the artefacts introduced by the ECs and to reduce the effects of Peripheral Nerve Stimulation (PNS) while preserving all properties described in the previous chapter. In this chapter we perform analytical experiments and two different phantom acquisitions to assess the goodness of the proposed formulation to decrease ECs artefacts. On the other hand, the proposed formulation to reduce PNS is introduced and evaluated through analytical experiments.

- **Part III:** This section contains the second contribution of this Thesis dissertation and focuses on the precise estimation of the diffusion-related parametric maps through the optimal selection of the diffusion-weighting b-values. It is divided in the following three chapters:
  - **Chapter 6** motivates the problems of the estimation of diffusion-related parametric maps and provides an overview of the multiple techniques proposed to optimize the set of b-values used in DWI with different objectives and for various diffusion signal models. At the same time it indicates the pros and cons of each technique. Next, it introduces the Cramér-Rao Lower Bound (CRLB), which will be the mathematical foundation of the formulations proposed in the next two chapters.
  - **Chapter 7** introduces the CRLB of the monoexponential DW signal model and the mathematical methods used to optimize the set of b-values for increased noise performance (i.e., precision increase and variance reduction) in the estimated Apparent Diffusion Coefficient (ADC) maps. This chapter continues with a validation carried out with analytical simulations and both phantom and in-vivo DWI experiments.
  - **Chapter 8** introduces the CRLB of the Intravoxel Incoherent Motion (IVIM) biexponential DW signal model and the mathematical methods used to optimize the set of b-values for precise estimation of the three diffusion-related parametric maps of the IVIM model. This chapter ends with an in-vivo liver DWI validation of the proposed formulation.

- **Part IV:** Backmatter part, which concludes this Thesis dissertation.
  - **Chapter 9** winds up this Thesis dissertation with a comprehensive discussion and conclusion of our work. It includes our contributions but also pinpoints our limitations as well as hypothesizes on some future lines of research.

2

Background

Contents

2.1 Introduction to Magnetic Resonance Imaging

2.1.1 MR physics

Current Magnetic Resonance Imaging (MRI) is based on the early discovery of Nuclear Magnetic Resonance (NMR) carried out by Bloch (1946) and Purcell et al.

(1946), which was originally of interests for the fields of physics and chemistry to study the atomic properties of nuclei. Both MRI and NMR techniques are based on the interactions of nuclear spins with an external magnetic field, thus, in order to completely describe the undergoing physical phenomenon quantum mechanics are usually employed. Nevertheless, when using the macroscopic limit of quantum mechanics to study the nuclear spins it reduces to classical mechanics. Thus, a complete explanation of the Magnetic Resonance (MR) phenomenon can be accomplished with classical mechanics (Hanson, 2008) as briefly described next.

As aforementioned, MR is based on the interaction between an external static magnetic field B_0 and a nucleus with a non-zero spin angular momentum. This physical property depends on the protons, neutrons and electrons of the nuclei, but only those with an odd number of them are eligible for MR. Some of these are the helium atom (3He), the fluorine atom (19F) and the phosphorus atom (31P). However, the most abundant nuclei in organic samples is the hydrogen atom (1H) due to its presence in water molecules, converting it into the most commonly used for imaging in MR and, as such, it will be the considered nucleus hereinafter. When a sample is not within a B_0, all of its spins are randomly distributed leading to a null macroscopic magnetization. On the other hand, when the sample is within a static magnetic field B_0, the spins reorganize to create a net magnetization (M_0) in the direction of the B_0 and start a rotation movement called precession around the same direction. By convention, the direction of the B_0 is the longitudinal (z) axis. Thus, the relation between the M_0 and B_0 can be written as:

$$\frac{\partial \mathbf{M}}{\partial t} = \mathbf{M} \times \gamma \mathbf{B}_0, \tag{2.1}$$

implying that the precession of M_0 around B_0 will be at an angular frequency on the transverse plane 'xy', also known as the Larmour frequency (ω_0) given by

$$\omega_0 = \gamma B_0 \quad [\text{rad/s}], \tag{2.2}$$

where γ is the gyromagnetic ratio specific to the nucleus. For 1H it is 42.58 MHz/T.

In addition to the external static magnetic field B_0, in MRI there are also time varying Radio-Frequency (RF) fields. These RF fields are short electromagnetic pulses (B_1) applied in the transverse plane that rotate at the Larmour frequency in phase with the magnetization M. With the application of the B_1 rotating magnetic field, the spins absorb energy, which will produce another rotation to the net magnetization modelled by:

$$\frac{\partial \mathbf{M}}{\partial t} = \mathbf{M} \times \gamma(\mathbf{B}_0 + \mathbf{B}_1), \tag{2.3}$$

where $\mathbf{B} = \mathbf{B}_0 + \mathbf{B}_1$. The new precession around the $\mathbf{B}_1$ magnetic field will tip the magnetization vector away from the longitudinal direction in a spiral way towards the transverse plane. The amount of rotation from the longitudinal axis 'z' is fixed by the intensity and duration of the $\mathbf{B}_1$, and is accounted for as the flip angle α.

Thus, the application of any RF pulse is considered to be an excitation of the system. Once part of the net magnetization is excited and tilted to the transverse plane 'M_{xy}', it can be measured by the proper receiving coil (i.e., receiving antenna) according to Faraday's law of induction. Note that, for convenience, RF pulses are named after the flip angles they produce.

Following the end of the RF pulse, the spins release the absorbed energy from the RF pulse through a time-varying signal named Free Induction Decay (FID) and, with time, return to equilibrium by restoring the net magnetization back into the longitudinal axis and fading away the transverse magnetization 'M_{xy}'. The process of returning to equilibrium is called relaxation, and is driven by the relaxation time constants T_1 and T_2, respectively. Both relaxations occur simultaneously, however, they are driven by different underlying interactions.

On the one hand, the longitudinal relaxation, i.e., the process of restoring the net magnetization into the longitudinal axis, is due to the interaction between the spins and the surrounding medium, i.e., spin-tissue interactions. This medium is composed of different lattices with different compositions, having each of them a different longitudinal relaxation time or T_1.

On the other hand, the transverse relaxation, i.e., the process of fading away the magnetization of the transverse plane, is due to the interactions between the micro magnetic fields generated by neighbouring spins, i.e., spin-spin interactions, and the spins with the field inhomogeneities of the external magnetic field $\mathbf{B}_0$. During the application of the RF pulse, all the spins precess in coherence, however, after its conclusion spins progressively lose their coherence depending on the neighbouring spins having each lattice a different transverse relaxation time or T_2. If the field inhomogeneities are also considered, the lost of coherence is faster, leading to a shorter transverse relaxation time name T_2^*.

The equation modelling MR dynamics of the magnetization M is the well-known Bloch equation which is based on the extension of Eq. (2.4) by including the dynamics of the previous relaxation phenomena. The Bloch equation is described next:

$$\frac{\partial \mathbf{M}}{\partial t} = \mathbf{M} \times \gamma \mathbf{B} - \frac{M_x \mathbf{i} + M_y \mathbf{j}}{T_2} - \frac{(M_z + M_0)\mathbf{k}}{T_1}, \tag{2.4}$$

where M_z is the longitudinal magnetization, M_0 is the equilibrium magnetization, and M_x and M_y are both components of the transverse magnetization. Particularly, the equations describing both relaxation phenomena can be independently described by:

$$\begin{cases} \frac{\partial M_z}{\partial t} = -\frac{M_z + M_0}{T_1} \\ \frac{\partial M_{xy}}{\partial t} = -\frac{M_{xy}}{T_2} \end{cases} \tag{2.5}$$

where the longitudinal relaxation is described by:

$$M_z(t) = M_0 + (M_z(0) - M_0)e^{-\frac{t}{T_1}}, \tag{2.6}$$

and the transverse relaxation is described by:

$$M_{xy}(t) = M_{xy}(0)e^{-\frac{t}{T_2}} \tag{2.7}$$

Further, if we also take into account the incoherences introduced by the fields inhomogeneities in the transverse relaxation phenomena, Eq. (2.7) transforms into

$$M_{xy}(t) = M_{xy}(0)e^{-\frac{t}{T_2^*}}, \tag{2.8}$$

where $\frac{1}{T_2^*} = \frac{1}{T_2} + (\gamma * \Delta B_{\text{inho}})$, being ΔB_{inho} the field inhomogeneities across the voxel.

2.1.2 MR image formation

In MRI, in order to obtain information of a particular plane of the sample, i.e., of the human body, we need to code its information through the usage of spatial field gradients. Firstly, we need to be able to perform a selective excitation of the corresponding plane. Secondly, we need to be able to form an image out of the excited plane. These techniques were initially proposed by Lauterbur (1973) and Mansfield and Grannell (1973) to obtain the first MR images.

Since the whole sample is affected by the same magnetic field B_0, all spins are processing at the same Larmor frequency proportional to the B_0 as shown in Eq. (2.2). Thus, to perform a selective excitation of a particular plane, we need to apply a spatial magnetic field gradient to obtain a magnetic field that depends on the position as:

$$\mathbf{B}(\mathbf{r}) = \mathbf{B}_0 + \mathbf{G} \cdot \mathbf{r}, \tag{2.9}$$

where G is the magnetic field gradient. This way, the new resonance frequencies of the spins will also depend on their position as:

$$w(\mathbf{r}) = \omega_0 + \gamma \mathbf{G} \cdot \mathbf{r} \tag{2.10}$$

Note that if a specific gradient is applied in one direction, i.e., x, y, z, or any linear combination of them, all the spins that lie at a particular perpendicular position of that direction will precess at the same resonance frequency ω(r). Therefore, if we apply a spatial field gradient perpendicular to the plane of the slice by adjusting the resonance frequency of the B_1 pulse to the Larmor frequency of the plane, we excite only that plane and avoid that the spins of other planes absorb energy.

In MRI, the orientation of the excited plane depends on the target tissue to be imaged. Traditional plane orientations are axial (plane 'xy'), coronal (plane 'xz'), and sagittal (plane 'yz') although oblique orientations can also be used. Also, the excited plane is considered a slice when its thickness is in the order of millimetres, or a slab if its thickness is in the order of centimetres.

Once a slice has been excited and there is magnetization in the transverse plane, all the spins of that slice will be precessing in phase generating a current in the receiver coil. A priori, the receiver coil is not able to distinguish between the currents generated from each point of the slice, thus, the application of spatial magnetic field gradients, i.e., imaging encoding gradients, is required to form an image.

For example, to form an image of an axial slice the application of imaging encoding gradients in both x and y directions is needed. One gradient is considered to be the phase encoding gradient, and the other one is the frequency encoding gradient. Thus, from ingenious combinations of both encoding gradients we can take advantage of the previously mentioned Larmour frequency modifications they introduce along the encoding gradient direction and of the phase accrual they introduce. This phase accumulated is given as:

$$\phi(x, y, t) = \omega_0 t + \gamma \int_0^t G_x(\tau)\partial\tau x + \gamma \int_0^t G_y(\tau)\partial\tau y \tag{2.11}$$

Finally, the signal throughout the slice is coded in both frequency and phase steps enabling its reconstruction.

The measured signal by the receiver coil will be the ensemble of all signals from all points of the image as shown next

$$s(t) = \int_x \int_y m(x, y) e^{-i2\pi[k_x(t)x + k_y(t)y]} \partial x \partial y, \tag{2.12}$$

where $m(x, y)$ is the spin density distribution, and

$$k_x(t) = \frac{\gamma}{2\pi} \int_0^t G_x(\tau)\partial\tau, \tag{2.13}$$

$$k_y(t) = \frac{\gamma}{2\pi} \int_0^t G_y(\tau)\partial\tau, \tag{2.14}$$

are the k-space trajectories along each axis. Eq. (2.12) is the 2D Fourier Transform (FT), which relates the measured signal in the image space with the sampled signal acquired by the receiver coils in the k-space as shown in Figure 2.1. Thus, the relationship between the image and the sampled data depends on the sampled k-space trajectory made by the imaging encoding gradients. It is to be noted that both the k-space and the image space signals are complex, albeit the final form of the image space usually is the magnitude image after discarding its phase information.

Traditionally, RF excitation pulses are repeated every Repetition Time (TR) to acquire a different line of the k-space at each repetition as shown in Figure 2.2. This way, the frequency encoding gradient is kept the same throughout each repetition to traverse the full width of the k-space, G_x in Figure 2.2, and the phase encoding gradient is varied to correctly point to the beginning of each new k-space line, G_y in Figure 2.2. This technique is named Spin-Warp Imaging. Subsequently, once the full k-space is acquired on a rectilinear cartesian trajectory, the Discrete Fourier Transform (DFT) is used to reconstruct the final image.

2.1.3 Rapid Imaging Techniques

The traditional line-by-line technique to acquire the k-space described in previous Section and shown in Figure 2.2 requires long acquisition times due to the need

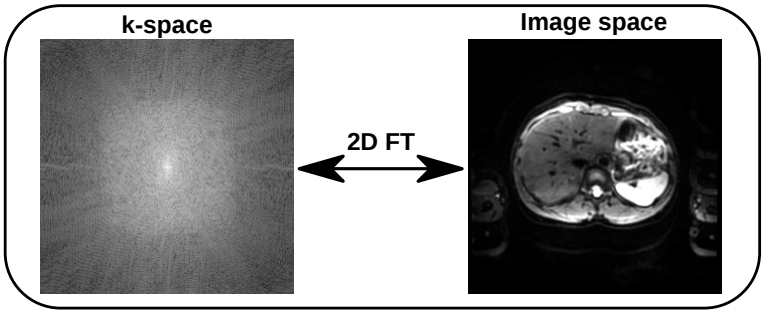

Figure 2.1: 2D Fourier Transform (2D FT) of an MR image of an in-vivo liver on both k-space (left) and image space (right).

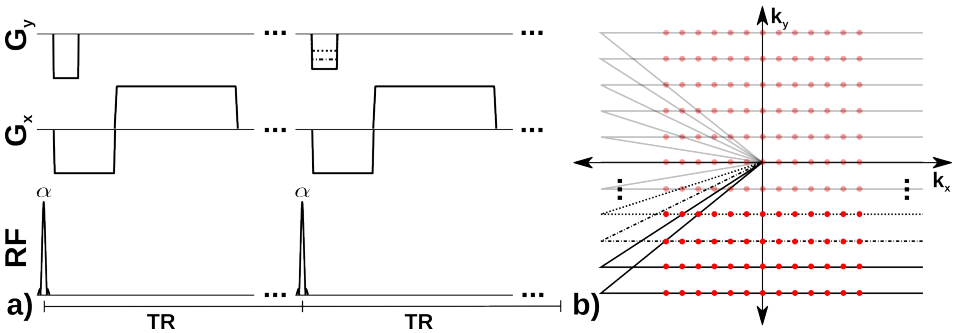

Figure 2.2: MR sequence example. a) Timing diagram of a sequence repeated every Repetition Time (TR) with a different phase encoding gradient. b) k-space trajectory and samples acquired (red dots) at each TR. Shaded k-space trajectories and samples correspond to repetitions of the sequence not shown on the timing diagram a) but needed to acquire the whole k-space.

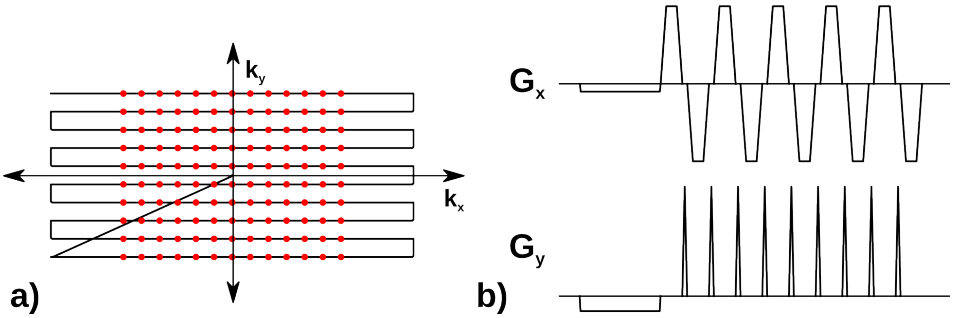

Figure 2.3: Echo Planar Imaging (EPI) sequence. a) k-space trajectory and samples acquired (red dots). b) Imaging encoding gradient waveforms on both x and y axis during signal acquisition.

to perform multiple RF excitations. These long times may further introduce the appearance of different artefacts such as motion. Thus, several techniques to reduce the time needed to sample the k-space have been proposed.

Echo Planar Imaging (EPI) is one of the most common techniques used to sample the whole k-space in a single RF excitation pulse, also known as single shot Echo Planar Imaging (SS-EPI), reducing the time needed to sample the image from minutes to milliseconds at the expense of demanding large efficiency operation to the MRI hardware. EPI was originally described by Mansfield (1977) and it consists on the location of the k-space on the bottom left corner by the application of rephasing gradients and on the subsequent application of multiple frequency and phase encoding gradients to cycle traverse from side to side of the k-space in a zig-zag pattern until all lines have been sampled. The phase encoding gradients to jump from line to line of the k-space are called blips. The frequency encoding gradients are also called readout gradients since they are the only ones activated when the analogue to digital converter samples the signal. An example of this k-space reading technique is shown in Figure 2.3.

Besides reducing the image scanning time, acquiring the whole k-space in a single RF excitation may introduce several artefacts into the reconstructed image. One of the most common artefacts of EPI appears due to the misalignments between the sampling of odd and even lines. These misalignments are produced by the differences between the frequency encoding gradients of consecutive lines due to having opposing polarity and introduce an artefact known as Nyquist ghosting (see Figure 2.14). As its very name indicates, this artefact consists of a ghost of the image along the phase encoding direction. Several correction methods have been proposed being the standard one the implementation of a reference scan without phase encoding gradients to measure the phase inconsistencies between odd and even lines. Another artefact that appears along the phase encoding direction is the chemical shift artefact (see Figure 2.10). It appears due to the different resonance frequency between water and lipid spins and results in a substantial shifting of the signal generated by the lipids. A simple way to correct these artefacts consists of implementing lipid suppression techniques prior to the RF

excitation pulses. Further, in EPI image distortions frequently appear along the phase encoding direction due to its low bandwidth. These distortions can occur due to off-resonance effects caused by field inhomogeneities or magnetic susceptibility variations and result image compressions, dilatations and/or shifting. These artefacts are commonly corrected by reconstructing the images taking into account the B_0 map. Finally, since the different k-space lines are acquired consecutively at different relaxation times, each of them carry a different T_2^* weighting which also causes blurring along the phase-encoding direction. This blurring can be corrected through multishot Echo Planar Imaging (MS-EPI), which reduces the time needed to acquire the k-space per shot, in spite of suffering from other problems such as motion-induced artefacts.

Another common technique for rapid imaging is Parallel Imaging (PI). PI is commonly used in combination with EPI and is based on the simultaneous sampling of the k-space by various receiver coils located around the Field-of-View (FOV). This way, each coil acquires a different image with a different sensitivity, and all of them are later combined to reconstruct the final image. Thus, the availability of repeated data points sampled with various coils allows the reconstruction of the final image from subsampled k-spaces, i.e., k-spaces with lower number of phase encoding steps, reducing the overall acquisition time. If the data points were not sampled multiple times, the reconstruction of the subsampled k-space would result in an aliased image. The two main techniques to perform the combination of multiple coil images are Sensitivity Encoding (SENSE) and Generalized Autocalibrating Partially Parallel Acquisition (GRAPPA). The former one solves a pixelwise linear reconstruction problem on the image space (Pruessmann et al., 1999) while the latter one solves the reconstruction problem directly on the k-space (Griswold et al., 2002). Nevertheless, despite reducing the acquisition time, PI generally results in noise amplification in the reconstructed images due to the fewer number of samples and the propagation of errors along the reconstruction procedures.

2.1.4 Fundamental MR pulse sequences

In MRI, we can obtain images that look different depending on the combination of the timings, RF pulses and gradients introduced in previous sections. Each different combination of these means is called sequence, and each sequence will obtain an image whose intensities will depend to great or less extent to some properties of the tissue. To this end, the two most basic pulse sequences are described next:

Gradient Echo (GRE) is composed of an RF pulse with α typically lower than $90°$ and a sequence of gradients with different polarities that provide coherence to the spins of the excited slice, increasing the signal strength of the transverse magnetization. Particularly, the prephasing gradient lobe after the RF pulse dephases the excited spins which are subsequently rephased by the readout gradient lobe producing an echo peak signal. The time at which the echo peak occurs is the Echo Time (TE) and corresponds to the time at which the dephased introduced by the prephasing gradient lobe is compensated by the readout gradient lobe as shown in Figure 2.4.

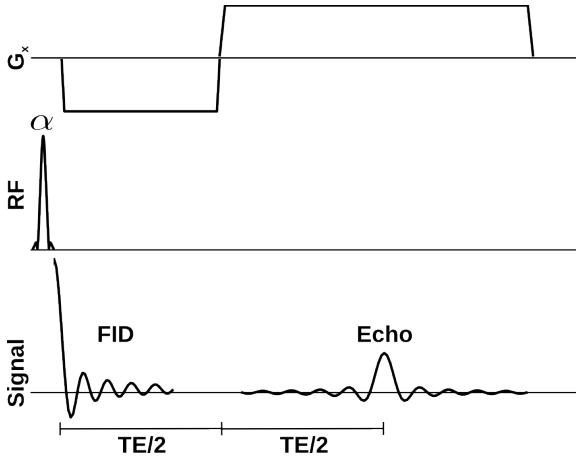

Figure 2.4: Standard gradient echo sequence with its Free Induction Decay (FID) and echo signal.

Table 2.1: "Combinations of TE and TR alues Used to Generate Various Contrast Weightings in Spin Echo Imaging" *(Table and caption taken from (Bernstein et al., 2004)).*

	Short TE ($\leq$ 20 ms)	Long TE ($\geq$ 80 ms)
Short TR (<700 ms)	T_1-weighted	Not commonly used
Long TR (>2000 ms)	Proton density-weighted	T_2-weighted

In GRE, the intensity of the echo peak will be primarily weighted by the T_2^* relaxation time as shown in Eq. (2.8). Nothe that the T_2^* relaxation not only depends on the tissue properties but also on the field inhomogeneities and susceptibility effects. These sequences are usually used for their speed as a result of their low TE, however their T_2^* weighting causes severe signal losses that hinder their utility.

Spin Echo (SE) is composed of two RF pulses, an initial one that acts as an excitation RF pulse with α typically of 90° and a successive one that acts as a refocusing RF pulse with α typically of 180°. The phase inversion introduced by the refocusing RF pulse refocuses the accrued phase from chemical shift, field inhomogeneities and susceptibility effects. Thus, the echo peak occurs at twice the time between both RF pulses, meaning that the refocusing RF pulse is located at time TE/2. See Figure 2.5 for details.

In SE, the intensity of the echo peak can be weighted by the T_1, T_2, and the proton density (Proton Density (PD)), i.e., spin density, depending on the combination of TE and TR as shown in Table 2.1. These sequences are used for their robustness, however they have considerably longer TE than GRE sequences.

Nevertheless, nowadays there are multiple imaging techniques and sequences de-

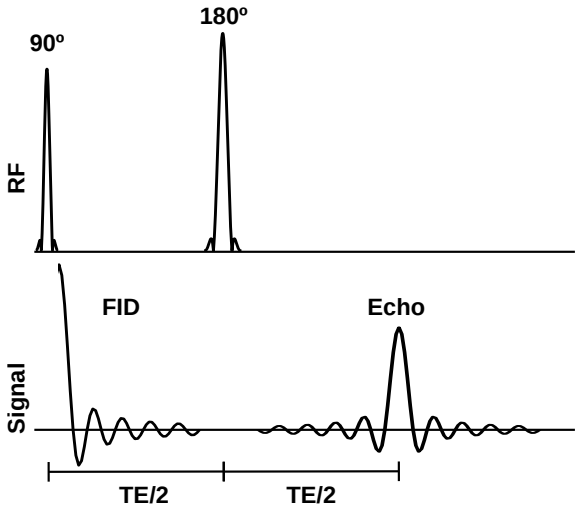

Figure 2.5: Standard spin echo sequence with its Free Induction Decay (FID) and echo signal.

signed to obtain different tissue contrasts or to overcome faults of the existing ones. Some of these are Inversion Recovery (IR) sequences, Chemical Shift Selective (CHESS) sequences, Susceptibility-Weighted Imaging (SWI) or Diffusion-Weighted Imaging (DWI) which will be the anchor point of this thesis on the following sections.

2.2 Diffusion-Weighted Imaging

2.2.1 Diffusion definition

Diffusion corresponds to the random displacement of molecules due to their thermal energy, i.e., energy present when temperature is above 0° K. This random displacement behaves as a random walking movement known as Brownian motion. It holds that name because it was initially noticed by Robert Brown in the early-19th when observing pollen grains randomly moving inside a static water solution.

Subsequently, in the mid-19th century Adolf Fick related the molecules random displacement to their concentrations throughout the sample. He established that there is a flux of molecules from regions with higher concentrations to regions with lower concentrations, being that flux proportional to the concentration gradient, which is directly related to the diffusion coefficient D whose units are in distance squared per time (i.e., mm^2/s). To model that phenomena, he introduced the Fick's law of diffusion, which in the early 20th century was extended on the PhD., thesis of Albert Einstein to create the diffusion equation (Eq. (2.15)). Einstein merged Fick's law of diffusion with Brownian motion defined following the statistics

of random walks.

$$\frac{\partial P(r,t)}{\partial t} = D\nabla P(r,t) \tag{2.15}$$

The previous equation can be easily solved through the FT to see that the probability distribution has the following Gaussian distribution:

$$P(r|\mu,\sigma) = \frac{1}{\sqrt{12\pi Dt}} e^{-\frac{(r-r_0)^2}{12Dt}} \tag{2.16}$$

This distribution indicates the probability of finding a particle in r that was originally in r_0 at time t. Thus, the Mean Squared Displacement (MSD) of particles along time in a three dimensional medium is:

$$\langle \Delta r \rangle^2 = 6Dt \tag{2.17}$$

In the previous equation we can see that the MSD is proportional to the diffusion time.

2.2.2 Diffusion Sensitive Sequences

Diffusion essentially consists of the displacement of molecules throughout the medium, thus, in the presence of a magnetic field gradient moving molecules will experiment different gradient intensities depending on their actual position causing phase dispersion throughout the slice. As a result, the induced phase dispersion will produce an attenuation of the transverse magnetization, hence a decrease of the echo peak.

Due to this phenomena, we can convert almost any MRI sequence into a diffusion sensitive sequence by introducing strong magnetic field gradients. These gradients are named diffusion-weighting gradients and, when introduced, the sequence becomes part of the family of diffusion imaging pulse sequences. Particularly, we can convert both GRE and SE sequences into diffusion imaging pulse sequences, however, due to the severe signal losses of GRE sequences, sequences whose echo peak is formed through the application of RF pulses, such as SE, are preferred on the clinical routine.

Stejskal and Tanner (1965) were the first who proposed the inclusion of diffusion-weighting gradients into the SE sequence. Originally, it was named Pulse Gradient Spin Echo (PGSE) and it is described in Figure 2.6.

Compared to the SE sequence introduced in Subection 2.1.4, the PGSE sequence includes a pair of diffusion-weighting gradients with the same amplitude (G), duration (δ), and polarity, separated by a time Δ and placed around the 180° RF pulse. With that gradient combination we are able to induce phase shifts that depend on the spin location to subsequently rephase them with the second diffusion-weighting gradient after the application of the 180° RF refocusing pulse. Consequently, at each voxel the accrued phase at the echo peak of static spins will be zero, while the accrued phase of moving spins will be different to zero because at both sides of the 180° RF pulse they have been subjected to different

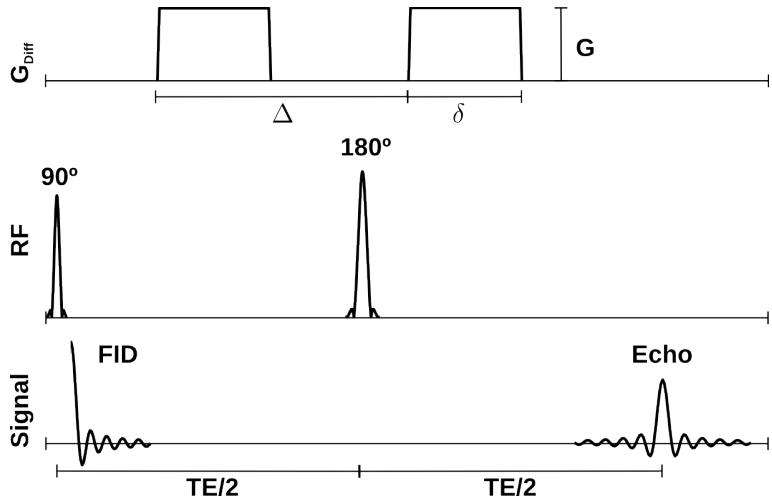

Figure 2.6: Pulse Gradient Spin Echo (PGSE) sequence for DWI (also known as SE-DWI).

gradient intensities. Hence, the decrease in the intensity of the echo peak due to intravoxel dephasing directly depends on the diffusion characteristics of the tissue. An illustrative display of moving and not moving spins under diffusion-weighting gradients is shown in Figure 2.7.

It is easy to notice that MRI does not measure the signal of each spin individually, but it measures macroscopic behaviour or an ensemble average of all spins within the voxel, i.e., spin density distribution. Therefore, from the probability density function of each spin given in Eq. (2.16), the ensemble-average diffusion propagator is:

$$P(r|t) = \int_{\Omega} \rho(x) P_s(r|r_0, t) \partial r, \tag{2.18}$$

where Ω is the physical volume of a voxel. This propagator can be further compared to the signal measured by diffusion imaging sequences in the scanner. If we consider the ideal case of the narrow pulse assumption when $\delta \ll \Delta$, which means that spins only move in the time between diffusion-weighting gradients, between the application of the diffusion-weighting gradients the spins might have moved from r_0 to r' following the $P(r|t)$. Consequently, compared to the sequences without diffusion-weighting gradients spins will have a phase deviation:

$$\varphi(r) = \gamma\delta \mathrm{G} r - \gamma\delta \mathrm{G} r_0 = \gamma\delta \mathrm{G}(r - r_0) \tag{2.19}$$

As a result, the signal measured when diffusion-weighting gradients are applied is proportional to the T_2 weighted signal obtained when there are no gradients, and given the macroscopic nature of DWI it is:

$$M_{xy} = M_0 \mathbb{E}\{e^{j\gamma\delta G(r-r_0)}\} = M_0 \int\int P(r, r_0|\Delta) e^{j\gamma\delta G(r-r_0)} \partial r \partial r_0 \tag{2.20}$$

Particularly for the PGSE sequence, we can see the effects of the RF pulses, diffusion-weighting gradients, relaxation phenomena and diffusion through by

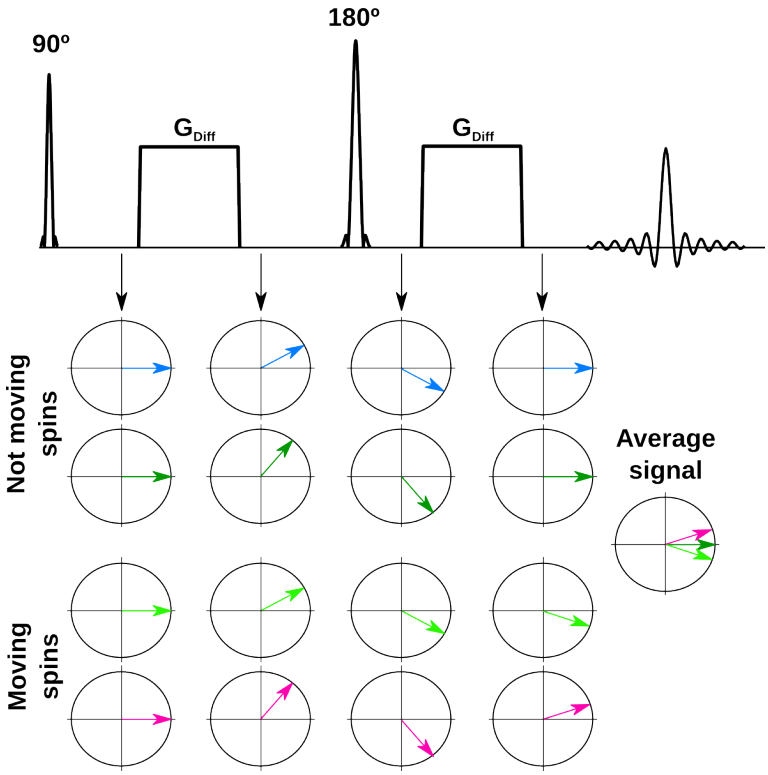

Figure 2.7: Evolution of various spin phases initially located in different positions along the SE-DWI acquisition. Not moving spins experiment the same gradient intensity at both sides of the RF-180 achieving complete rephasing by the end of the second diffusion-weighting gradient. Moving spins do not experiment the same gradient intensity at both sides of the RF-180 not achieving complete rephasing. The signal of a voxel corresponds to the ensemble of all moving and not moving spins within the voxel, being its attenuation related to the diffusivity.

analysing the Bloch-Torrey equation:

$$\frac{\partial \mathbf{M}}{\partial t} = \mathbf{M} \times \gamma \mathbf{B} - \frac{M_x \mathbf{i} + M_y \mathbf{j}}{T_2} - \frac{(M_z + M_0)\mathbf{k}}{T_1} + \nabla \cdot D \nabla \mathbf{M}, \tag{2.21}$$

where ∇ is the laplacian operator. For simplicity, solving the previous Bloch-Torrey equation without the T_1 and T_2 relaxation terms results in the measured signal at TE by the PGSE sequence:

$$S(\mathrm{TE}) = S_0 e^{-\int_0^{\mathrm{TE}} k(\tau)^T D k(\tau) \partial \tau} = S_0 e^{-\gamma^2 D \int_0^{\mathrm{TE}} [(\int_0^t \mathbf{G}(\tau)\partial\tau)^T (\int_0^t \mathbf{G}(\tau)\partial\tau)] \partial t}, \tag{2.22}$$

where $k(t)$ is:

$$k(t) = \gamma \int_0^t G(\tau) \partial \tau \tag{2.23}$$

If rectangular diffusion-weighting gradients are used, Eq. (2.22) can be further simplified to:

$$M_{xy} = M_0 e^{-\gamma^2 D G^2 \delta^2 (\Delta - \delta/3)} \tag{2.24}$$

Eq. (2.24) shows that the sensitivity of diffusion imaging sequences is characterized by Δ, δ, and the diffusion-weighting gradient shape which together conceive the term of b-value as:

$$\mathrm{b-value} \equiv \mathrm{b} = \gamma^2 G^2 \delta^2 (\Delta - \delta/3), \tag{2.25}$$

which in standard DWI simplifies the measured signal to:

$$S(b) = S_0 e^{-b \cdot D} \tag{2.26}$$

Essentially, by adding diffusion-weighting gradients to any sequence we can also make it sensitive to the diffusion properties of the medium in addition to being sensitive to its T_1, T_2 and PD properties. This is the case of several extensions of the SE such as the Twice Refocused Spin Echo (TRSE) or the Stimulated Echo (STE). The echo peak of these sequences is also formed from RF pulses and the diffusion-weighted measured signal essentially corresponds to the monoexponential signal of Eq. (2.26). The upside of these sequences is that they behave better when the MRI is subjected to strong eddy currents or that they achieve higher diffusion-weightings, i.e., higher b-value, albeit suffering from lower signal intensities, which is crucial in DWI.

Throughout the previous descriptions and derivations we assumed that the excited medium does not contain barriers and that the diffusion is homogeneous being the same in every direction. These mediums are called isotropic mediums and are characterized by a single diffusion constant D [mm^2/s]. A concur example of an isotropic medium is a glass of water where the diffusion constant is 3.00 mm^2/s at 37.5°C. On the other hand, if the medium contains barriers the diffusion will more likely happen along certain directions than along others. Due to this property, these mediums are called anisotropic mediums and are characterized by the diffusion tensor. As a result, to obtain all the information of the diffusion tensor diffusion imaging sequences need to be repeated several times by applying the diffusion-weighting gradients in different non-collinear directions. This direction

dependency transforms the b-value constant into the b-matrix and supposes a straightforward change of the diffusion imaging technique to Diffusion Tensor Imaging (DTI).

In order to pave the way for accessible MRI, several DWI sequences for both, isotropic and anisotropic mediums have been made available on GitHub by the author of this Thesis. These include SE-DWI, and TRSE-DWI sequences with different k-space trajectories developed on PyPulseq, an open source MRI pulse sequence design package for Python (Geethanath and Vaughan Jr, 2019; Ravi et al., 2019). These sequences can be run on any General Electric, Siemens, and Bruker MRI scanners provided that their Pulseq (Ravi et al., 2018) interpreters are available. Further, they provide the versatility to easily change any sequence parameter such as FOV, slice thickness, matrix size, number of slices, set of b-values, diffusion-weighting directions, TE and TR. Nevertheless, the available DWI sequences were only used in this Thesis when specifically stated.

2.2.3 Diffusion Models

So far in this chapter, we have described the diffusion phenomena in isotropic and anisotropic mediums under the assumption of free diffusion. In biological tissues, however, this assumption does not hold true due to the presence of multiple physiological underlying effects (Le Bihan, 2007b). Thus, due to the macroscopic nature of DWI the physical concept of diffusion (D) is replaced with the global concept of Apparent Diffusion Coefficient (ADC)) (Le Bihan et al., 1986). With this nomenclature, the measured diffusion equation is formulated as:

$$S(b) = S_0 e^{-b \cdot \mathrm{ADC}} \tag{2.27}$$

In the past three decades, the monoexponential diffusion Eq. (2.27) has been successfully applied in the clinical routine to help diagnose, characterize, and perform treatment monitoring of numerous pathologies non-invasively. For example, it is commonly used for the diagnosis of pathologies such as stroke in the brain and metastasis in the liver as shown earlier in Section 1.1.

This monoexponential diffusion signal model was proposed by Stejskal and Tanner in the 60s. Then, in the 80s, thanks to a better understanding of the biological tissues Le Bihan et al. (1988) proposed the Intravoxel Incoherent Motion (IVIM) signal model. This model separates the contribution of the Diffusion-Weighted (DW) signal into two terms. The first one corresponds to the signal of the diffusing spins, and the second one corresponds to the signal coming from the microcirculation or pseudodiffusion of blood flow in the capillary network. The IVIM signal model is:

$$S(b) = S_0 \left[f e^{-b \cdot D^*} + (1 - f) e^{-b \cdot D} \right], \tag{2.28}$$

where f is the pseudodiffusion fraction, D^* the pseudodiffusion coefficient and D the diffusion coefficient. The pseudodiffusion fraction (f) relates to the percentage of a voxel volume occupied by capillaries and the pseudodiffusion coefficient (D^*) relates to the blood velocity, which is about ten times greater than D.

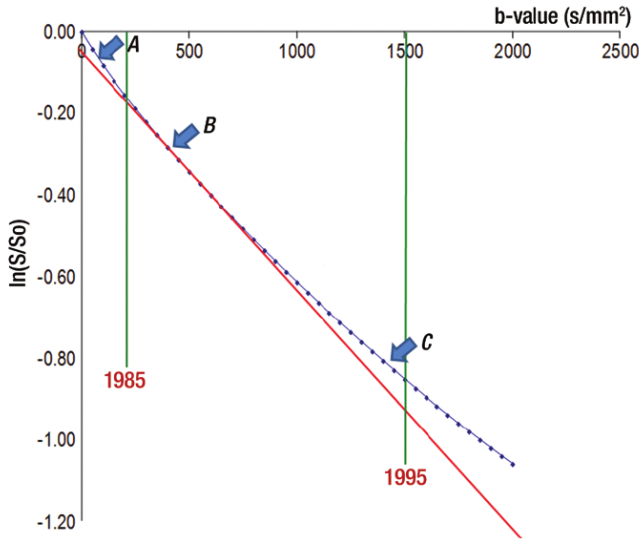

Figure 2.8: "Plot of the diffusion MR imaging signal attenuation (S/S0) against the b-value. The plot is straight only with intermediate b-values (arrow B). The slope is then the ADC. At very low b-values (arrow A), the slope is higher, with the inclusion of perfusion (intravoxel incoherent motion effect). At higher b-values (arrow C), the plot gets curved and the slope (ADC) decreases with the b-value, reflecting its non-Gaussian nature in tissues (hindrance of diffusion by tissue elements, such as cell membranes). Around 1985, only very low b-values were available. Around 1995, b-values around 1500 s/mm^2 became common, while today very high b-values (5000 s/mm^2 and higher) can be reached." (*Figure and caption taken from Le Bihan (2013)*).

Later on, with the advancement of MRI hardware, particularly due to the improvement of gradient coils and amplifiers, the sensitivity of the diffusion imaging sequences considerably increased. The application of higher b-values (either due to stronger gradients or longer diffusion times) has shown that the diffusion signal deviates from the monoexponential signal decay, which implies a deviation from the Gaussian behaviour described before. This signal deviation from the Gaussian model, as well as the maximum achievable b-values along the past four decades, is shown in Figure 2.8. Consequently, there has been considerable research in the development of new diffusion signal models to try to explain that deviation phenomenologically.

One of the earliest empirical models proposed to explain that non-Gaussian behaviour was introduced by Bennett et al. (2003). This is the stretched exponential model which includes the dimensionless stretching parameter α. α can be in the range [0, 1] and is known as the heterogeneity index or the anomalous index. The lower the α the more heterogeneous is the medium. The stretched exponential model is:

$$S(b) = S_0 e^{-(b\cdot \mathrm{ADC})^{\alpha}} \quad \text{where} \quad \alpha \in [0, 1] \tag{2.29}$$

Later in 2005, a second model was proposed by Jensen et al. (2005) to account for

the non-Gaussian behaviour of biological tissues at high b-values. This model is a straightforward extension of the exponent of the monoexponential model through the Taylor series by the inclusion of the kurtosis term (K). In the case of Gaussian diffusion, the kurtosis term would be 0, however, in the case of non-Gaussian diffusion K is greater than 0. This novel signal model is named Diffusion Kurtosis imaging (DKI) and is as follows:

$$S(b) = S_0 e^{-b \cdot \mathrm{ADC} + \frac{b^2 \mathrm{ADC}^2 K}{6}} \tag{2.30}$$

It is to be noted that all previous signal models have been described as having constant parameters, still they can be transformed into their tensor form similarly to the standard monoexponential and DTI models.

2.3 Medical Applications of DWI

DWI has proven to be a magnificent technique for the diagnosis, characterization and monitoring of multiple pathologies. Initially applied to diagnose brain strokes, it rapidly extended to target other tissues such as liver, breast, prostate, and kidneys among others. Below we show some pathologies and applications to which DWI is applied to. Further details and applications can be found in (Koh and Thoeny, 2010; Padhani et al., 2009a; Taouli et al., 2016).

Hepatic Metastasis is better diagnosed with DWI than with T_2-weighted MRI (Bruegel et al., 2008a). Particularly, low diffusion-weighting b-values facilitate lesion detection, while high b-values are used for the characterization of the metastasis.

Diffuse Hepatic Disease. It is believed that DWI can contribute to diagnose the grade of hepatic fibrosis (Lewin et al., 2007). It can also be studied with more complex diffusion models such as IVIM, where the pseudo-diffusion parameter has been shown to decrease in cirrhotic livers compared to healthy volunteers (Chow et al., 2012; Luciani et al., 2008).

Breast Lesion Detection. The application of DWI to the identification of breast benign and malignant lesions has been thoroughly studied. The diffusion coefficient has been shown to be lower in malignant breast lesions than in benign breast lesions as reported by Guo et al. (2002); Woodhams et al. (2005). This diffusion coefficient decrease might be caused by the increase of cellularity of malignant breast lesions.

Acute Pancreatitis can be diagnosed with DWI without the usage of contrast agents with better sensitivity than with Computerized Tomography (CT) (Shinya et al., 2009). If using the diffusion coefficients, care must be taken because even though the diffusion coefficients of the acute pancreatitis are low in comparison to the parenchyma, the coefficients of the pancreas gland seems to change with age due to the presence of fat and atrophy (Herrmann et al., 2013).

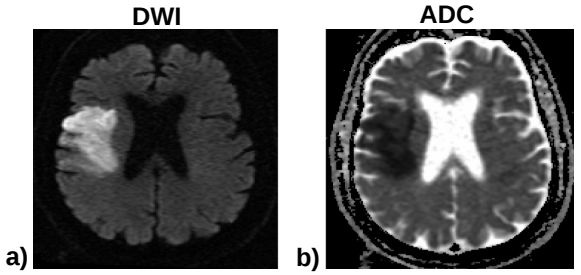

Figure 2.9: Diffusion-weighted imaging (DWI) of a patient with acute stroke (a) and the corresponding ADC map (b). The stroke affected area is shown bright on the DW image and dark on the apparent diffusion coefficient map. (*Figure taken from Birenbaum et al. (2011)*).

Prostate Cancer can be better diagnosed and characterized in the prostate gland by including DWI acquisitions to the standard T_2-weighted MRI. The diffusion coefficient improves detection of the prostatic carcinoma in the peripheral zone (Haider et al., 2007). In addition, DWI in the prostate helps with the localization of the lesion that sometimes fails with other methods such as ultrasound-guided biopsy (Park et al., 2008).

Myocardial Edema Detection can be detected with DWI thanks to the later hardware advancement (Luna et al., 2012). Due to the strong cardiac motion, the application of DWI to the heart requires strong diffusion-weighting gradients and low b-values to diminish motion artefacts. Further, it requires a modification of the standard Stejskal and Tanner DWI sequence to synchronize the sequence with the cardiac phases. The diffusion coefficient of the edema in acute infarcted myocardium is lower than in healthy myocardium.

Lung Cancer detection with DWI is as challenging as the application of DWI to the previous myocardial edema detection. The diagnostic accuracy of nodal metastasis in the mediastinum has shown to be higher with DWI than with Positron Emission Tomography (PET) scans (Nomori et al., 2008), while it is also effective for a precise lesion localization. On the other hand, the diffusion coefficient parameter needs to be treated carefully since there is considerable overlap in the ranges of different lung pathologies (Matoba et al., 2007).

Stroke Detection is one of the first successes of DWI (Moseley et al., 1990). While early detection of acute stroke is neither feasible with T_1-weighted or T_2-weighted MR Imaging nor with CT. The former imaging modalities need up to 6 hours while the latter one needs days for stroke detection. With DWI acute stroke can be diagnosed after a few minutes of arterial blockage, and the diffusion coefficient varies through the subsequent phases. An example of a DWI acquisition of a patient that suffers from acute stroke with the corresponding diffusion coefficient map is shown in Figure 2.9.

Brain Diseases. The application of DWI and its extension to DTI, same sequence that DWI's although applied in multiple diffusion-weighting directions, to the brain has evolved from stroke and tumor diagnosis and characterization to the

diagnosis of neurological and neurodegenerative diseases. For example, it has been shown that DTI might be helpful for the identification of the structural brain mapping in migraine (Planchuelo-Gómez et al., 2020) and that it might be useful for the early diagnosis of Parkinson's disease on its prodromal stage (Peña-Nogales et al., 2019a). Other applications of DWI/DTI target Alzheimer's disease, schizophrenia or epilepsy. However, while all these are promising applications of DTI they are still in their early research stages.

2.4 Artefacts, Limitations, and Pitfalls

In Section 1.1 we defined a quantitative imaging biomarker as an objectively measurable characteristic of the tissue that needs to fulfill various requirements (i.e., precision, accuracy, reproducibility, robustness and of clinical utility). However, in order for a measure to achieve these requirements there are some artefacts, limitations and pitfalls of the MR images, and particularly, of the DW images, that need to be overcome. Some of these are described next:

B_0 field inhomogeneities. One of the main components of the MR scanners is the strong static magnetic field B_0. Ideally, the B_0 magnetic field is designed to be as homogeneous as possible within the scanner bore when no patient is present. However, B_0 field inhomogeneities are always present due to the presence of metallic components, the size and shape of the room, and the lack of ideal magnets. In turn, the magnetic field varies across the FOV producing spatially-dependent variations of the Larmor frequency, which contribute to the formation of some image artefacts such as shading, spatial distortions, image blurring or signal loss. Note that all of these artefacts will be more noticeable for larger FOVs since magnetic field variations will also be larger. In order to increase the homogeneity of the B_0 magnetic field active and passive shimming is commonly used. Also, artefacts can be corrected with image postprocessing methods since the B_0 field map can be obtained with specialized sequences.

Susceptibility artefacts are another source of magnetic field inhomogeneities that, opposite to the B_0 field inhomogeneities, originate from the sample or patient to be imaged. Each material has different susceptibility properties (χ) depending on how they behave in the presence of an external magnetic field. It the material disperses the magnetic field it is called diamagnetic, while if it concentrates the magnetic field it is called paramagnetic or even ferromagnetic if the effect is strong. This dependency is also present in biological tissues being most of them diamagnetic with different degrees of susceptibility. On the contrary, air is slightly paramagnetic. As a result, when a patient is in the MR scanner it will create spatially-dependent variations of the Larmour frequency that will contribute to similar artefacts to the ones explained above. These are particularly strong next to metallic implants due to their ferromagnetic properties. In order to diminish susceptibility artefacts, spin-echo sequences, as the ones traditionally used for DWI, are prefered over gradient echo sequences, and similar postprocessing methods than those implemented for the B_0 field inhomogeneities can be applied.

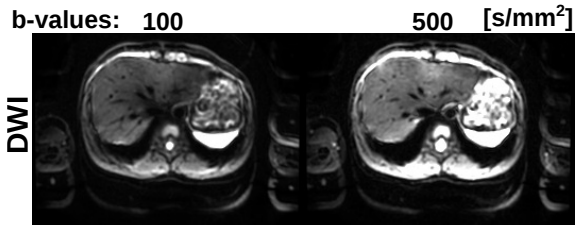

Figure 2.10: Chemical shift artefact in the phase encoding direction of a liver Spin Echo Echo Planar Imaging (SE-EPI) acquisition at b-values [100, 500] s/mm^2.

B_1 inhomogeneities are also related to the artefacts caused by B_0 field inhomogeneities and susceptibility artefacts. Firstly, if the spins precess at a frequency slightly different to the Larmor frequency the B_1 RF pulse, applied at the Larmor frequency, will not be in resonance with them. Secondly, if the spins precess at the Larmor frequency but the B_1 RF pulse varies spatially throughout the FOV the spins will not be in resonance either. In either case, these off-resonance effects will produce the net magnetization to precess around an effective field (B_{eff}) oriented at an angle between B_0 and B_1. From these, the first problem was tackled on the description of previous two artefacts, and the second one can be tackled by using complex amplitude- and frequency-modulated RF pulses that can be made almost insensitive to B_1 inhomogeneities.

Chemical shift is caused by the small shifts in the resonant frequency of some spins due to the different chemical environment of their nuclei. The most frequent case in MRI can usually be seen around the interfaces of water-containing structures surrounded with fat. In this case, the hydrogen protons of fat are partially shielded from the external magnetic field due to their atomic structure, which translates into a reduction of their Larmor frequencies. For instance, at 3T the spins of fat protons resonate at around 430 Hz lower than spins of water protons. Thus, since the MRI is tuned to excite and measure at the Larmor frequency of water protons the different resonance frequency of fat compared to the water may produce a displacement of several voxels of the fat on the acquired images hindering image interpretation. The direction of the displacement will depend on the acquisition sequence, being stronger in the low-bandwidth imaging encoding directions. Hence, this artefact can be tackled by increasing the receiver bandwidth, or by incorporating fat suppression techniques into the acquisition sequence. An example of a chemical shift artefact is shown in Figure 2.10.

Motion is inherently one of the most severe artefacts in MRI due to the long acquisition times. There are several types of motion that can introduce ghosting artefacts into the MR images such as cardiac motion, respiratory motion or patient movement as shown in Figure 2.11. On the other hand, some other types of motion can also be valuable for MRI techniques such as Brownian motion, i.e., diffusion, or blood flow, i.e., perfusion. In any case, the motion sources that introduce artefacts into the MR images should be controlled and the artefacts diminished in order to facilitate image interpretation. There is a large number of techniques to eliminate or diminish motion artefacts (Norris, 2001) 1) some focus on the minimization of

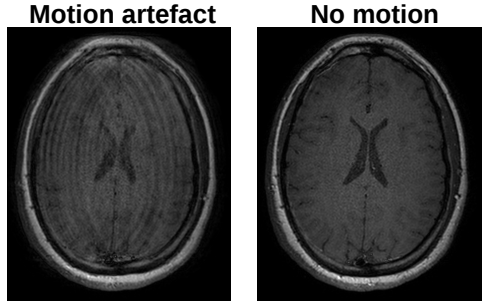

Figure 2.11: Patient motion artefact on a T_1-weighted Spin Echo Echo Planar Imaging (SE-EPI) brain acquisition with Repetition Time (TR) of 637 ms.

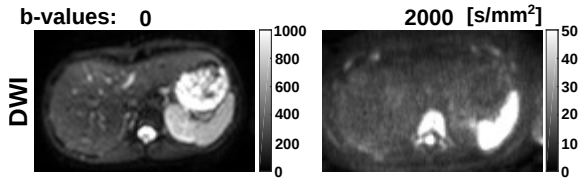

Figure 2.12: Diffusion-weighted (DW) image of the liver at b-values [0, 2000] s/mm^2. The DW image at b-value 2000 smm^2 shows poor SNR.

motion through sedation or stabilization, 2) some on signal suppression through the use of saturation pulses, 3) others use faster imaging sequences such as EPI, flow-compensated sequences, low motion-sensitive acquisition sequences or perform multiple acquisitions of the same sequence, 4) other techniques involve triggering, gating or navigator echos to perform different parts of the acquisition at the same motion instant, and 5) finally, there are also postprocessing techniques to estimate and correct for motion.

Noise are signal fluctuations inherent to any scientific measurement. In MRI, these fluctuations are due to thermal noise, which is included by the voltage fluctuations in the scanned object and in the receiver coils while measuring the k-space signal. MRI and particularly DWI are image modalities with intrinsically low signal intensities due to the acquisition procedure and the relaxations phenomena as shown in Figure 2.12. As a result, they achieve low Signal-to-Noise-Ratio (SNR) compared to other imaging modalities such as Computerized Tomography. The SNR in MRI is proportional to the static magnetic field B_0, the voxel size and the number of samples. It is also inversely proportional to the receiver bandwidth. Thus, the SNR can be increased by accordingly varying previous parameters in the sequence. Further, the noise distribution depends on the acquisition procedure, coil system and on the image formation. In order to remove its effects on the acquired images it can be filtered out, and the actual noise distribution can be used for better parameter estimation (Aja-Fernández and Vegas-Sánchez-Ferrero, 2016).

Acoustic noise is generated in every MRI acquisition. Whenever a strong current is driven into a conductor placed in a magnetic field a Lorentz force is generated. If the current is switching rapidly a time-varying force distribution is generated as occurs in the gradient coils. These forces produce vibrations that are radiated into other physical parts of the scanner or into the air producing acoustic noise. According to the Lorentz force, the stronger the driven gradients and the faster they switch the more vibrations and more acoustic noise will be generated. Thus, DWI and EPI are some of the sequences that generate stronger acoustic noise which may cause patient discomfort, anxiety and may restrict fetal acquisitions due to possible hearing loss (Hutter et al., 2018). The simplest technique to reduce acoustic noise consists of providing ear plugs and/or headphones to the patient as well as acoustically isolating the MR room. Further, reducing the gradient strength and switching speed can also decrease the acoustic noise in spite of reducing image quality.

Eddy Currents (ECs), also known as Foucault currents, are generated according to the Faraday-Lenz Law of electromagnetism, where a varying magnetic field induces electric currents in nearby conductors, which in turn generate their own magnetic field with opposite polarity to the source one. In MRI the sources of the varying magnetic field are typically the gradients and the source of the eddy currents is any metallic component such as other coils, shields or wires. ECs are proportional to the gradient strength, the switching time, and persist after the gradients are switched off, which may result in severe image artefacts. ECs especially cause serious artefacts in DWI due to the strong diffusion-weighting gradients, which can introduce image shearing, shifting, scaling, and blurring due to the persistent eddy currents during the application of the imaging gradients (Jezzard et al., 1998). They might also cause misestimation of the diffusion coefficients due to a misinterpretation of the effective diffusion-weighting b-value applied, and image ghosting during the application of EPI sequences due to mis-registrations between even and odd echos. In order to reduce eddy currents and the artefacts they might produce, MR scanners implement active shielding gradients, gradient pre-emphasis to counteract a priori the induced eddy current, advanced sequences with low sensitivity to eddy currents as the TRSE DWI sequence (Reese et al., 2003) shown in Figure 2.13, reference scans and/or postprocessing techniques. An example of image ghosting and the corrected image is shown in Figure 2.14.

Concomitant Gradients (CGs) are a consequence of Maxwell's equation of the curl and the divergence. They are nonlinear and spatially dependent magnetic field gradients that appear any time we generate a magnetic field gradient. At the isocenter of the MR scanner they are zero but they increase parabolically away from it in standard symmetric MR scanners, thus, their effects will be stronger with larger gradient strengths and in larger FOVs. Some DWI sequences are prone to the artefacts CGs introduce due to the application of the strong diffusion-weighting gradients. These can be phase variations within the imaging plane that may result in k-space blurring and shifting, and phase variations through imaging plane that may result in signal attenuation due to the phase dispersions across a given voxel (Baron et al., 2012). In order to reduce these we can use adapted MR sequences, gradient derating or use postprocessing correction methods during

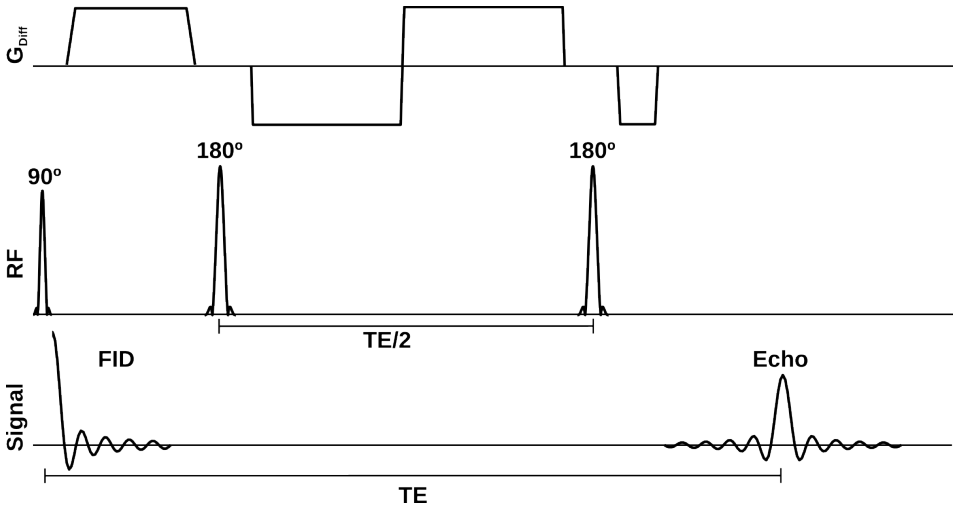

Figure 2.13: Twice Refocused Spin Echo (TRSE) DWI sequence. G_{Diff} are the diffusion-weighting gradients.

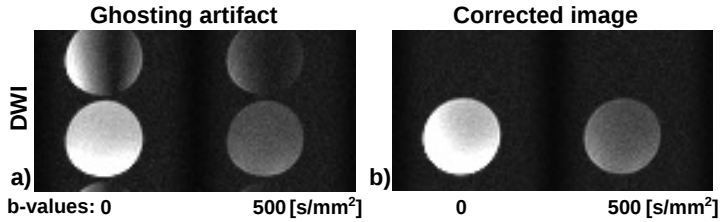

Figure 2.14: Ghosting artefacted image and corrected image, a) and b), respectively, of a doped water phantom SE-EPI DWI acquisition at b-values of [0, 500] s/mm^2. The ghosting artefact in the phase encoding direction was introduced due to the misalignment of even and odd echos of EPI due to induced Eddy Currents. The corrected image was obtained via postprocessing using a reference scan.

image reconstruction.

Gradient nonlinearities. Gradients are linearly varying magnetic fields that are zero at the scanner isocenter. However, similarly to the external magnetic field inhomogeneities, the linearity of the magnetic field gradients also lessens away from isocenter. It is important to note that some MRI vendors may sacrifice gradient linearity to increase other gradient characteristics such as rise time (Janke et al., 2004). The increment of gradient nonlinearities may introduce image distortions due to erroneous spatial encoding, blurring and phase variations that might turn into signal attenuation. Further, in DWI gradient nonlinearities may produce spatially dependent b-values which result in erroneous estimations of the diffusion coefficients (Malyarenko et al., 2014). Common procedures to correct these artefacts are applied during image reconstruction due to their known response.

Peripheral Nerve Stimulation (PNS) is caused by the fast switching of magnetic field gradients and consists of the stimulation of muscles and nerve cells. Any muscle or nerve cell can be stimulated, however, the stimulation is remarkably more intense in the peripheral nerves, and as such the effect is named PNS. For instance, the threshold for PNS is around one order of magnitude softer than the threshold for cardiac stimulation. In modern clinical scanners patients might suffer it in sequences where the magnetic field gradients are driven fast to large gradient strengths such as in DWI or PI and it can cause tingling, poking of the skin or even involuntary muscle movement which might produce patient anxiety (Schulte and Noeske, 2015). Since nerve stimulation appears due to the application of high performance gradient coils with short ramp times and high gradient strengths used for fast imaging an standard approach to reduce them is by simply increasing the ramp time used to drive the gradient to its maximum strength.

Blood signal. As previously mentioned, due to the cyclic respiratory and cardiac motions MRI acquisition of certain tissues is arduous. Thus, in order to reduce motion-induced signal losses in some tissues gradient moment-nulling techniques are commonly employed. These techniques are frequently included in DWI for target tissues such as the heart or the liver. However, while DWI should provide tissue characterization by only probing microscopic Brownian motion, if gradient moment-nulling techniques are implemented it also probes signal from moving blood as shown in Figure 2.15. This lack of signal suppression will result in bright spots in blood vessels of DW images, which might introduce biases in the diffusion coefficient maps (Zhang et al., 2019). Further, the bright spots of unsuppressed blood signal can mimic focal lesions, consequently hindering image interpretation.

Power cosumption. MRI uses highly specialized equipment (i.e., magnet, cryocoole, heat exchanger, patient table, gradient amplifier, RF units, computer and more modules). However, its high level of functionality and performance turns into huge energy demands since the quality of the generated images is directly related to the strength of the magnetic field and the power of the gradient amplifiers and RF untis. The power consumption of an MRI scanner can be divided into its three operational modes (Off, Ready-to-scan, and Scan). While the computation and the patient table average power consumption is below 5% of the power consumed by the scanner in one day, the power consumed by the magnet is 82%, 52%, and

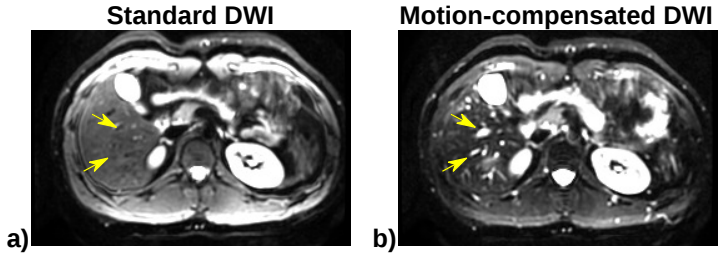

Figure 2.15: Diffusion-weighted images of a standard DWI acquisition (a) and a motion-compensated DWI acquisition with gradient moment-nulling (b). b-Value of both DW images is 100 s/mm^2. Yellow arrows point at blood vessels which show suppressed and unsuppressed signals on the standard and on the motion-compensated images, respectively.

38% in each operational mode, respectively. Subsequently, there is an increase off the other modules power consumption from 16% in the Off mode to 58% in the Scan mode (Herrmann and Annekristin, 2012). This increase of the power consumption in the Scan mode is mainly due to the gradient amplifiers and the RF units, considerably used in every acquisition. Traditional techniques to reduce power consumption consist in reducing the intensity of the gradient amplifiers and the RF units albeit degrading the acquired image. Also, novel imaging modalities (i.e., Magnetic Resonance Fingerprinting and Synthetic MRI) considerably reduce the scan time with the corresponding reduction of the power consumption (Ma et al., 2013; Moya-Sáez et al., 2020).

Signal models. In DWI the spins of water molecules are assumed to diffuse freely throughout the medium, that is, the diffusion distribution is Gaussian. Under that assumption the diffusion signal model equates to a monoexponential decaying signal where the diffusion coefficient is termed ADC. It holds that name because in biological tissues diffusion is known to be complex due to the presence of multiple compartments, cells, proteins, membranes, organelles . . . , and as such, it is conceived to summarize all hidden physical phenomena that occur at smaller scales still not available for DWI (Le Bihan, 2013). Also, the monoexponential model is valid at low diffusion-weightings, i.e., low b-values, but at higher b-values the signal model deviates from the monoexponential behaviour. Thus, these last two situations make it difficult to retrieve specific microstructure information from ADC measurements. As a consequence, to obtain added tissue information from DWI new diffusion-weighting signal models have been developed to try to connect phenomenologically the signal parameters with the underlying tissue structure.

Parameter estimation is a crucial aspect of some magnetic resonance imaging techniques such as relaxometry, susceptibility mapping or DWI. Parameter estimation from weighted images provides further information to the radiologist to assess the patient's pathology. However, parameter estimation entails controversy due to the choice of the appropriate acquisition parameters (i.e., b-value), the multiple parameters some signal models contain, and the low SNR of some weighted images which might make accurate and precise parameter estimation unfeasible in the

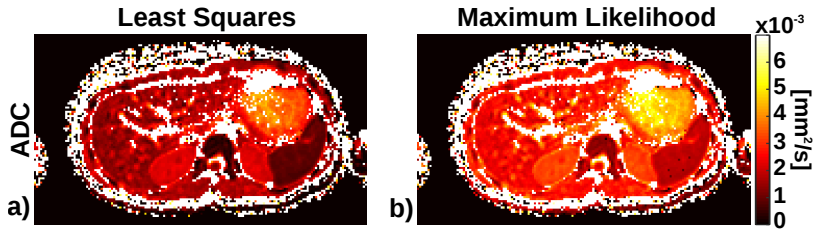

Figure 2.16: ADC estimated maps of a liver DWI acquisition estimated with a least squares estimator and a maximum likelihood estimator, a) and b), respectively, for a particular set of b-values. Note the differences on the estimated maps for both estimators.

clinical routine (Barbieri et al., 2016; Peña-Nogales et al., 2020). Note that in clinical practice the acquisition time is limited. In order to diminish the impact on the estimated maps, multiple signal weighting methods have been proposed based on the Error Propagation (EP) formulation or on the Cramér-Rao Lower Bound (CRLB), as well as estimators based on voxel-wise or Region of Interest (ROI) -wise analysis and deep learning. Figure 2.16 shows the variability of the estimated ADC maps from the monoexponential signal diffusion model across two different estimators for the same set of b-values.

Lack of standardization. In some tissues, the application of many MR sequences and reconstruction procedures lack standardization in terms of methodology, terminology and portrayal of the experiments carried out in publications; this is the case of DWI in the liver. This lack of standardization greatly limits its understanding and hinders the comparison between multiple studies performed at different research centers and clinics. Most of the factors that contribute to that diversity are related to how different publications tackle each of the aforementioned artefacts and pitfalls such as the actual implemented sequence, the image reconstruction techniques, the signal model and its parameters nomenclature or the estimator employed, among others. All these conceivable combinations affect DWI interpretation to such an extent that, for instance, liver DWI has been called 'the tower of Babel' by Guiu and Cercueil (2011), due to the difficulties to understand all the terminology and methodology of published studies. An example of methodology variation across six different studies is shown in Table 2.2.

Other artefacts in MRI include Gibbs artefacts, Zebra artefacts, Overflow artefacts, Dielectric effects or Zero fill artefact, among others. They fall however out of the scope of this dissertation.

2.5 Parameter estimation

2.5.1 Noise in MRI

In previous sections we have described the nature of the generated and acquired MR signal. However, while the generated signal was characterized in the strict sense,

Table 2.2: "Mean ADCs of normal liver and focal liver lesions, ADC cutoffs, and Sensitivity for diagnosing malignant lesions as reported across six different studies". Among other factors, the variability of the set of b-values of DWI produce large variability on the estimated ADC maps hindering the comparison between studies. (*Table and caption obtained from Taouli and Koh (2009)*).

Parameter	(Namimoto et al., 1997)	(Kim et al., 1999)*	(Taouli et al., 2003)†	(Bruegel et al., 2008b)	(Gourtsoyianni et al., 2008)	(Parikh et al., 2008)
No. of patients/lesions	51/59	126/79	66/52	102/204	38/37	53/211
b-values (s/mm^2)	30, 1200	$\leq$ 846	$\leq$ 500	50, 300, 600	0, 50, 500, 1000	0, 50, 500
ADC values						
Normal liver	0.69	1.02	1.83	1.24	1.25-1.31	Not applicable
Metastases	1.15	1.06 - 1.11	0.94	1.22	0.99	1.50
HCCs	0.99	0.97 - 1.28	1.33	1.05	1.38	1.31
Hemangiomas	1.95	2.04 - 2.10	2.95	1.92	1.90	2.04
Cysts	3.05	2.91 - 3.03	3.63	3.02	2.55	2.54
Adenomas - focal nodular hyperplasias	Not applicable	Not applicable	1.75	1.40	Not applicable	1.49
Benign lesions	1.95	2.49	2.45	Not applicable	2.55	2.19
Malignant lesions	1.04	1.01	1.08	Not applicable	1.04	1.39
ADC cutoff for diagnosis of malignant liver lesions‡	Not applicable	1.60	1.50	1.63	1.47	1.60
Sensitivity %	Not applicable	98	84	90	100	74
Specificity %	Not applicable	80	89	86	100	77

* ADCs for b $<$ 850 s/mm^2 are given.

† ADCs for b = 0 - 500 s/mm^2 are given.

‡ Lesions with ADC below the proposed cutoff value are considered malignant, while those with ADC above are considered benign.

the acquired signal was characterized in the loose sense. In addition to all previous phenomena, the acquired signal is also affected by noise as it always happens in any scientific measurement. Particularly, in MRI the main source of noise are the voltage fluctuations known as the thermal noise introduced by scanned object, followed by the thermal noise introduced by the receiving coils during acquisition of the k-space (Hoult and Lauterbur, 1979). These noise fluctuations are known to have a Gaussian distribution with zero mean and a variance proportional to

$$\sigma^2_{\text{thermal}} \approx 4k_B T R_{\text{eff}} B_W, \tag{2.31}$$

where k_B is the Boltzmann's constant, T is the temperature of the receiving coils, R_{eff} is the effective resistance of the coils and the scanned object, and B_W is the receiver bandwidth (Aja-Fernández and Vegas-Sánchez-Ferrero, 2016). Its presence in the acquired images may not only complicate visual assessment of the MR images, but it may also hinder further postprocessing steps such as the computation of the diffusion and related parameters, and thus, the extraction of quantitative imaging biomarkers.

Due to its random nature, the most common way to cope with the noise present in the measured complex k-space is through probabilistic modeling. Its accurate modeling will provide tools for processing the MR images and to estimate the aforementioned diffusion and related parameters.

In many fields the most common way to take advantage of noise modeling is through noise filtering techniques, however, in MRI we can use it for many other applications such as image reconstruction (Dolui et al., 2012; Michailovich et al., 2011), image segmentation (Roy et al., 2012; Wu et al., 2011) and particularly for parameter estimation (see Part III of this Thesis dissertation). Furthermore, if the appropriate noise modeling was not taken into account, this noise could be amplified, which could degrade the quality of the reconstructed images or complicate parameter estimation. Therefore, a thorough study of the effect of the noise in MRI is vital to guarantee the computation of quantitative imaging biomarkers.

Albeit being able to describe the noise model in MRI by a single receiving coil as a zero mean white Gaussian noise with the same value of the variance σ^2 for every pixel within the acquired data, i.e., the noise is stationary: the noise features do not depend on the position. The final noise probability model in the magnitude data will depend on the coil configuration of the MR scanner and on the different postprocessing steps the acquired data is submitted to.

In an antenna with L-coils, where L is the number of coils, the complex k-space acquired signal $\hat{s}_l(k)$ by the l-th coil is polluted by additive white Gaussian noise with zero mean and variance $\sigma^2_{k_l}$:

$$\hat{s}_l(k) = s_l(k) + n_l(k; \sigma^2_{k_l}), \quad l = 1, \cdots, L \tag{2.32}$$

where $s_l(k)$ is the DFT noise free acquired signal of Eq. (2.12), and $n_l(k; \sigma^2_{k_l}) = n_{l_r}(k; \sigma^2_{k_l}) + i \cdot n_{l_i}(k; \sigma^2_{k_l})$ the additive white Gaussian noise process on both the

real and imaginary canals which is assumed to be stationary. Finally, through the inverse DFT we obtain the signal in the complex image space:

$$\hat{S}_l(x) = S_l(x) + N_l(x; \sigma^2_{k_l}), \quad l = 1, \cdots, L \tag{2.33}$$

where $N_l(x; \sigma^2_{k_l})$ is also a complex additive white Gaussian noise (Thunberg and Zetterberg, 2007) with zero mean due to the linearity of the DFT. In this manner, the Probability Density Function (PDF) of the Gaussian noise distribution is:

$$P_{\hat{S}}(\hat{S}|S, \sigma) = \frac{1}{\sqrt{2\pi\sigma^2}} e^{-\frac{(\hat{S}-S)^2}{2\sigma^2}}, \tag{2.34}$$

where $\hat{S}$ and S are the intensity of the image and the true amplitude of the signal on the corresponding space. Further, the relation between the k-space and the image space noise variances is given by the number of points of the DFT as:

$$\sigma^2_l = \frac{1}{|\Omega|} \sigma^2_{K_l}, \tag{2.35}$$

where $|\Omega|$ is the number of voxels of the reconstructed FOV. Note that in this case there are no spatial correlations.

Next, in the case of PI the receiver antenna is composed of multiple coils used to accelerate the image acquisition process as explained in previous Section 2.1.3. This acceleration is achieved by subsampling the k-space data in each coil but results in the appearance of aliasing in the image space. Thus, to suppress this artefact PI techniques reconstruct the non-aliased image through the combination of the information acquired by the multiple coils of the antenna. However, the noise distribution of the reconstructed images depends on the way the information from each coil is combined.

In PI the relation between the noise variances in the k-space and the image space of Eq. 2.35 depends on the reconstruction process. If the $S^{\mathcal{S}}_l(x)$ is reconstructed directly through the inverse DFT of $S^{\mathcal{S}}_l(k)$, where the superscript $\mathcal{S}$ indicates the acquired signal is subsampled, Eq. 2.35 becomes:

$$\sigma^2_l = \frac{r}{|\Omega|} \sigma^2_{K_l}, \tag{2.36}$$

where r is the acceleration factor. On the contrary, if zero-padding is applied to the missing k-space lines (i.e., the lines of the k-space not acquired) Eq. 2.35 becomes:

$$\sigma^2_l = \frac{1}{|\Omega| \cdot r} \sigma^2_{K_l}, \tag{2.37}$$

As previously indicated in Section 2.1.3, SENSE and GRAPPA are methods to reconstruct the final image from subsampled versions of the signals in each coil. However, new methods that typically constitute a pipeline of linear operations over the subsampled signal $S^{\mathcal{S}}_l(k)$ are being continuously proposed, and they still are

the main cause of introducing non-stationary noise into the final reconstructed magnitude images. The reconstruction methods can be mainly grouped by two different approaches:

- **Reconstruction of a single complex image:** This reconstruction process applied in SENSE combines the subsampled data acquired by the different coils together with the sensitivity map of each coil and the covariance matrix, among other additional information, to obtain the final image

$$\hat{S}^{\mathcal{R}}(x) = f\left(\{S_l^{\mathcal{S}}(x), l = 1, \cdots, L\}; \Theta\right), \tag{2.38}$$

  where the $f(\cdot)$ is a linear reconstruction function (Blaimer et al., 2004), and Θ all the additional information needed. The linear reconstruction function applied over the Gaussian data reconstructs the final images but generates correlated Gaussian data whose variance depends on the position:

$$\hat{S}^{\mathcal{R}}(x) = S^{\mathcal{R}}(x) + N^{\mathcal{R}}(x; \sigma^2_{\mathcal{R}}(x)) \tag{2.39}$$

  where $N^{\mathcal{R}}(x; \sigma^2_{\mathcal{R}}(x))$ is a non-stationary complex additive white Gaussian noise. The final step to reconstruct the image corresponds to the computation of the magnitude image. This is partly due to its simpler visual interpretation and robustness:

$$M(x) = |\hat{S}^{\mathcal{R}}(x)| \tag{2.40}$$

  and therefore is polluted with a non-stationary Rician noise distribution. The PDF of this noise distribution is:

$$P_{\hat{S}}(\hat{S}|S, \sigma) = \frac{\hat{S}}{\sigma^2}\exp\left(-\frac{\hat{S}^2 + S^2}{2\sigma^2}\right) I_0(\frac{S\hat{S}}{\sigma^2}), \quad \text{where} \quad \hat{S} > 0, \tag{2.41}$$

  where I_0 is the 0th order modified Bessel function of the first kind.

- **Reconstruction of multiple complex images:** The reconstruction process obtains a reconstructed image per coil from the combination of the data from the different coils:

$$S_l^{\mathcal{R}}(x) = f_l\left(\{S_m^{\mathcal{S}}(x), m = 1, \cdots, L\}; \Theta\right), \quad \text{with } l = 1, \cdots, L. \tag{2.42}$$

  where $f_l(\cdot)$ is a linear reconstruction function over each coil (Blaimer et al., 2004; Griswold et al., 2002). Similarly to the previous case, the linear reconstruction function applied over the Gaussian data of each coil reconstructs the images but generates correlated Gaussian data for each coil whose variance depends on the position:

$$S_l^{\mathcal{R}}(x) = A_l^{\mathcal{R}}(x) + N_l^{\mathcal{R}}(x; \sigma^2_{\mathcal{R}_l}(x)), \quad \text{with } l = 1, \cdots, L. \tag{2.43}$$

  Then, the distribution of the final reconstructed magnitude image depends on the method used to combine the images from the different coils. Probably

the simplest procedure to perform this combination is the Sum-of-Squares (SoS):

$$M_{\mathrm{SoS}}(x) = \sqrt{\sum_{l=1}^{L} |S_l^{\mathcal{R}}(x)|^2}. \tag{2.44}$$

Note that Eq. (2.44) is equivalent to

$$M_{\mathrm{SoS}}(x) = |S^{\mathcal{R}}(x)| \sqrt{\sum_{l=1}^{L} |C_l(x)|^2}, \tag{2.45}$$

where $C_l(x)$ are the sensitivity maps of each coil. Thus, this procedure assumes that the coil sensitivities are constant through the image.

$$\sum_{l=1}^{L} |C_l(x)|^2 = \alpha. \tag{2.46}$$

In this case, since the $M_{\mathrm{SoS}}(x)$ is the sum of multiple signals, the Rician distribution is no longer valid, and it can be approximated by a non-stationary non-central chi (nc-χ) distribution if the variance of the noise is assumed to be the same for all coils, and no correlation exist between them (Aja-Fernández and Vegas-Sánchez-Ferrero, 2016). This is the case of GRAPPA acquisitions and the PDF of the nc-χ noise distribution is:

$$P_{\hat{S}}(\hat{S}|S,\sigma,L) = \frac{\hat{S}^L S^{1-L}}{\sigma^2} \exp\left(-\frac{\hat{S}^2 + S^2}{2\sigma^2}\right) I_{L-1}\left(\frac{S\hat{S}}{\sigma^2}\right), \quad \text{where} \quad \hat{S} > 0. \tag{2.47}$$

In antennas with multiple coils noise correlations do exist, but they are usually left aside due to their minimal effects and practical considerations (Constantinides et al., 1997). If the correlations were taken into account the PDF of the magnitude images could be accurately approximated by the standard nc-χ model of Eq. (2.47) with new effective parameters (i.e., reduced number of coils L and increased variance of the noise σ^2) (Aja-Fernández and Vegas-Sánchez-Ferrero, 2016).

Another common procedure linearly combines the complex signals of each coil using a Spatial Matched Filter (SMF) (McKenzie et al., 2002). However, this procedure requires extra information such as the sensitivity maps of each coil. An implementation of the SMF procedure is:

$$S_T^{\mathcal{R}}(x) = \sum_{l=1}^{L} S_l^{\mathcal{R}}(x) \cdot C_l(x). \tag{2.48}$$

In this case, the complex image $S_T^{\mathcal{R}}(x)$ still follows a complex Gaussian distribution whose magnitude image follows a non-stationary Rician distribution.

Table 2.3 shows a survey of noise models in the final magnitude images for different acquisition and reconstruction schemes. For further details about noise in MRI see Aja-Fernández and Vegas-Sánchez-Ferrero (2016).

Table 2.3: Survey of noise models in the final magnitude images for different acquisition and reconstruction procedures schemes. (*Table courtesy of Santiago Aja-Fernández* (Aja-Fernández and Vegas-Sánchez-Ferrero, 2016))

Coils	**Parallel**	**Reconstruction**	**Model**	**Stationarity**	**Params.**
Single	Single	–	Rician	Stationary	σ^2
Multiple (uncorrelated)	No	SoS	nc-χ	Stationary	σ^2 L
Multiple (correlated)	No	SoS	nc-χ (approx.)	Non-stationary	$\sigma^2_{\text{eff}}(x)$ $L_{\text{eff}}(x)$
Multiple (uncorrelated)	No	SMF	Rician	Stationary	σ^2
Multiple (correlated)	No	SMF	Rician	Non-stationary	$\sigma^2(x)$
Multiple	PI	SENSE	Rician	Non-stationary	$\sigma^2_{\mathcal{R}}(x)$
Multiple	PI	GRAPPA + SoS	nc-χ (approx.)	Non-stationary	$\sigma^2_{\text{eff}}(x)$ $L_{\text{eff}}(x)$
Multiple	PI	GRAPPA + SMF	Rician	Non-stationary	$\sigma^2_{\mathcal{R}}(x)$

2.5.2 Estimation Theory

In previous Section 2.2.3 we described a series of mathematical models that describe the behaviour of the diffusion signal depending on the voxel intensity of the DW images and the b-values. These models describe the diffusion process macroscopically, which will introduce unavoidable errors in the estimation of the diffusion parameters. Another source of error in the estimation of the diffusion parameters comes from the additive noise of the measurements. The thermal noise affects the voxels intensity converting them into random variables. As such, if multiple measurements are done under the same conditions, the corresponding voxels intensities will vary, i.e., observations, as well as the estimated diffusion parameters, i.e., estimates. These variations are inevitable, however they can be diminished through the application of the appropriate estimators i.e., the procedure to calculate an estimate from sampled data. In order to know which estimator is appropriate for DWI data, we need to work with the statistical parameter estimation theory (Kay, 1993).

Given a set of N observations of random variables $X = (X_1, X_2, ..., X_N)^T$ whose PDF is parametric with regard to an unknown parameter vector $\boldsymbol{\theta} \in \mathbb{R}^P$, the estimation consists in the computation of such parameter vector. Thus, from the vector of observations (i.e., realizations of the random variables) $x = (x_1, x_2, ..., x_N)^T$ we compose a vector of estimates $\hat{\boldsymbol{\theta}} = g(x_1, x_2, ..., x_N)$, where $g(\cdot)$ is a vector with P components and N variables. These estimates correspond to a realization of the random variable $\hat{\boldsymbol{\theta}} = g(X_1, X_2, ..., X_N)$, meaning that we will obtain different estimates for a new set of observations x. Hence, $\hat{\boldsymbol{\theta}} = g(X_1, X_2, ..., X_N)$ is an statistical estimator as defined by Papoulis and Pillai (2002).

Estimation theory defines several desired properties for statistical estimators.

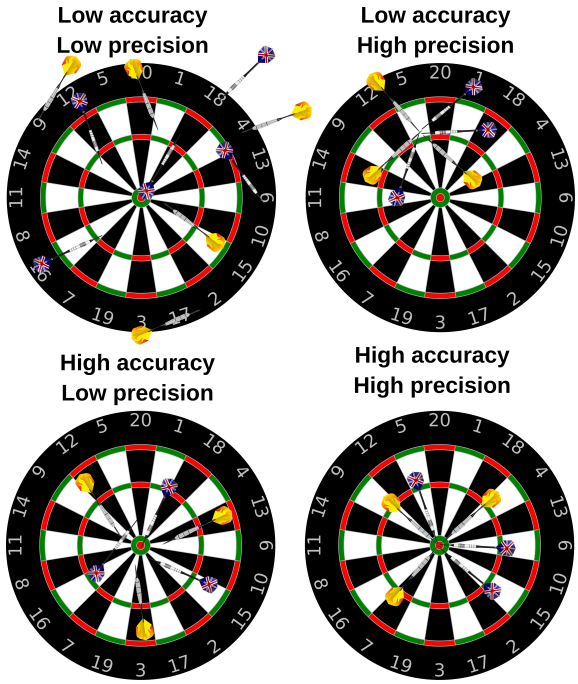

Figure 2.17: Graphical representation of accuracy and precision on a dartboard.

- An estimator should obtain estimates which are close to each other on average. This property is called **precision**, and is known as the variance of the estimates. Formally, the precision of an estimator is defined as

$$\text{var}(\hat{\boldsymbol{\theta}}(X)) = \left([C_{\hat{\boldsymbol{\theta}}(X)}]_{11}, [C_{\hat{\boldsymbol{\theta}}(X)}]_{11}, ..., [C_{\hat{\boldsymbol{\theta}}(X)}]_{PP}\right)^T, \tag{2.49}$$

  where $C_{\hat{\boldsymbol{\theta}}(X)}$ is the covariance matrix of the random vector $\hat{\boldsymbol{\theta}}(X)$. The lower the variance of the estimates, the higher the precision. A graphical representation of the precision is shown in Figure 2.17.

- An estimator should obtain estimates which are close to the real value on average. This property is called **accuracy**, and is known as the bias of the estimates. Formally, the bias of an estimator is defined as

$$\text{bias}(\hat{\boldsymbol{\theta}}(X)) = \mathbb{E}\{\hat{\boldsymbol{\theta}}(X)\} - \boldsymbol{\theta}, \tag{2.50}$$

  where $\mathbb{E}\{\cdot\}$ is the expectation operation. The lower the bias of the estimates, the higher the accuracy. Within this property, we can consider that an estimator is unbiased if the bias of its estimates is zero. If the bias tends asymptotically to zero when the number of samples increases towards infinity, the estimator is asymptotically unbiased. A graphical representation of the accuracy is shown in Figure 2.17.

In order to choose the optimal realizable estimator in terms of precision and accuracy, the standard procedure consists on selecting the estimators with the

maximum possible accuracy, this is, the unbiased estimators, and then selecting the one with the highest precision. This is basis of the procedure performed in Part III of this Thesis dissertation to increase the precision of the DWI diffusion-related parametric maps.

- An estimator should obtain estimates which are closer to each other and closer to the real value with an increasing number of samples. This property is called **consistency**, which is equivalent to an asymptotically unbiased estimator when its variance tends to zero. Formally, the consistency of an estimator is defined as

$$\lim_{N\to\infty} \Pr(||\hat{\boldsymbol{\theta}}(X)) - \boldsymbol{\theta}||_2 > \epsilon) = 0, \tag{2.51}$$

  where $\Pr(\cdot)$ is the probability of the estimates to converge to θ.

- An estimator should uniformly have the minimum variance as well as being unbiased. Such an estimator is called **uniformly minimum variance unbiased estimator (UMVUE)**, and the word uniformly implies that the estimator should have the minimum variance regardless of the values of θ. Formally, the UMVUE (Kay, 1993) is defined as

$$\text{var}(\hat{\boldsymbol{\theta}}_{UMVUE}(X)) \leq \text{var}(\hat{\boldsymbol{\theta}}(X)) \quad \forall\ \hat{\boldsymbol{\theta}}(X) \text{ with bias}(\hat{\boldsymbol{\theta}}(X)) = 0. \tag{2.52}$$

- An unbiased estimator should obtain the highest possible precision. Such an estimator is called **efficient**. Formally, an efficient estimator is defined as

$$C_{\hat{\boldsymbol{\theta}}(X)} > \boldsymbol{I}^{-1}(\boldsymbol{\theta}, \tag{2.53}$$

  when the following regularity condition holds true:

$$\mathbb{E}\{\frac{\partial \log P_x(x|\boldsymbol{\theta})}{\partial \boldsymbol{\theta_p}}\} = 0, \quad \text{with } p = 1, 2, ..., P, \tag{2.54}$$

  where $\boldsymbol{I}(\cdot)$ is the Fisher Information Matrix (FIM) further described later in Chapter 6, and $P_x(x|\boldsymbol{\theta})$ the joint PDF of the random variables $X = (X_1, X_2, ..., X_N)^T$ at observations x. However, the problem remains on establishing the existence of the upper bound of the precision of the estimates, i.e., a lower bound on the variance of the estimates. To establish that bound we can rely on the existence of the Cramér-Rao Lower Bound (CRLB) also described on Chapter 6. If the estimator achieves the highest possible precision as the number of samples increases towards infinity it is said to be asymptotically efficient.

Next, we describe two of the most common estimators that attain some of the previous properties.

Least Squares (LS) estimators are based on the estimation of the parameters by minimizing the squared discrepancies between the sampled data and their

expected values, i.e., their L_2-norm. These discrepancies are also known as residuals. Assuming we have a random variable X_n that depends on parameter θ as follows:

$$\mathbb{E}\{X_n\} = \phi_n(\boldsymbol{\theta}), \tag{2.55}$$

where $\phi(\boldsymbol{\theta})$ is a deterministic signal model for $n = 1, ..., N$. As such, LS estimator seeks to minimize the following residual

$$\hat{\boldsymbol{\theta}}_\mathrm{LS} = \arg\min_{\boldsymbol{\theta}} \sum_{n=1}^{N} (x_n - \phi_n(\boldsymbol{\theta}))^2, \tag{2.56}$$

where $\hat{\boldsymbol{\theta}}_\mathrm{LS}$ is the LS estimate when $\phi_n(\cdot)$ is a linear function of $\boldsymbol{\theta}$ and x_n for $n = 1, ..., N$ is the sampled data. If for any reason, we want to give a different importance to each residual, we can easily extend the LS estimator to Weighted Least Squares (WLS) estimator by multiplying each residual by a specific weight w_n. On the other hand, if $\phi_n(\cdot)$ is a nonlinear function of $\boldsymbol{\theta}$ the corresponding random LS estimator would be the Non Linear Least Squares (NLLS) estimator.

Maximum Likelihood (ML) estimators are based on the maximum likelihood principle to obtain the estimates of parameters $\boldsymbol{\theta}$ that most likely produced the sampled data x_n. To be able to construct this estimator we need prior information of the data, particularly, we need to know its PDF $P_x(x|\boldsymbol{\theta})$. From the PDF we construct the likelihood function from some given data x as $L(\boldsymbol{\theta}|x)$. The set of parameters most likely to produce the sampled data corresponds to the maximum point of the likelihood function. Thus, the ML estimate can be obtained as:

$$\hat{\boldsymbol{\theta}}_\mathrm{ML} = \arg\max_{\boldsymbol{\theta}} L(\boldsymbol{\theta}|x), \tag{2.57}$$

where $\hat{\boldsymbol{\theta}}_\mathrm{ML}$ is the ML estimate. The actual implementation of ML is usually based on the negative log-likelihood as:

$$\hat{\boldsymbol{\theta}}_\mathrm{ML} = \arg\min_{\boldsymbol{\theta}} \mathscr{L}(\boldsymbol{\theta}|x), \tag{2.58}$$

where $\mathscr{L}(\boldsymbol{\theta}|x) = -\log L(\boldsymbol{\theta}|x)$.

In the case of having sampled data with Gaussian distributed noise both the ML and the WLS estimators are equivalent if the weights (w_n) are wittily chosen and both share multiple of previously described properties. However, in the case of having Rician distributed noise only the ML estimator is consistent and asymptotically unbiased and efficient (Papoulis, 1977). These implications together with the nature of the DW magnitude data make the ML estimator the standard one to estimate the diffusion and related parameters throughout this Thesis dissertation.

Part II

Contribution I:

Diffusion-Weighting Gradient Waveform Design

3

Optimized Diffusion-Weighting Gradient Waveform Design (ODGD): Motivation and Theory

Contents

3.1 Introduction

Diffusion-Weighted Magnetic Resonance Imaging (DW-MRI) has a unique ability to non-invasively probe tissue microstructure as detailed shown in Section 1.1. By applying powerful diffusion-weighting gradient waveforms (Stejskal and Tanner, 1965), DW-MRI is sensitive to the microscopic Brownian motion of water molecules, with multiple applications for tissue characterization in health and disease (Koh

and Collins, 2007; Le Bihan et al., 1986; Padhani et al., 2009a; Taouli and Koh, 2009).

However, as briefly shown in Section 2.4, the application of these powerful diffusion-weighting gradients results in significant imaging challenges including:

- Signal dephasing due to bulk motion (Liau et al., 2012; Murtz et al., 2002; Taouli and Koh, 2009).
- Signal dephasing due to Concomitant Gradients (CGs)-induced fields, also known as Maxwell fields (Baron et al., 2012; Bernstein et al., 1998; Meier et al., 2008).
- Image distortions due to Eddy Currents (ECs) (Aliotta et al., 2018; Bernstein et al., 1998; Jezzard et al., 1998).
- Possible Peripheral Nerve Stimulation (PNS)(Den Boer et al., 1999; Reilly, 1989).

Bulk motion artefacts are particularly severe in organs that experience substantial physiological motion (e.g., heart and liver). In these organs, the presence of macroscopic elastic tissue motion during the application of the diffusion gradients can result in localized signal voids (Anderson and Gore, 1994; Murphy et al., 2013; Norris, 2001; Trouard et al., 1996). CGs are characterized by Maxwell's equations, and appear in sequences where the diffusion gradients are asymmetrical about the radiofrequency pulse (Baron et al., 2012), and can introduce large spatially dependent dephasing in diffusion MRI sequences. Lastly, ECs and PNS appear when the gradient amplifiers are switched fast to drive large gradient intensities. Switching gradients result in current inductions characterized by the Faraday-Lenz Law of electromagnetism that persist after the gradients are switched off (Bernstein et al., 1998; Weissenberger, 2002; Zhou, 1998), and can introduce large image distortions (i.e., shearing, shifting, scaling and blurring), misestimation of the b-value and ghosting. Switching gradients can also cause an electric depolarization that may lead to nerve stimulation (Glover, 2009; Schulte and Noeske, 2015; Zhang et al., 2003), which can cause tingling and involuntary muscle movement and might increase patient anxiety. The peripheral nerves are more prone to experience the stimulation, hence, it received the name of peripheral nerve stimulation (Feldman et al., 2009).

Bulk motion-, Concomitant Gradient (CG)-, and ECs-related signal dephasing can complicate the interpretation of DW images and introduce bias and variability in the quantification of diffusion parameters. In addition, PNS may increase patient discomfort.

Multiple approaches have been proposed to address the effects of bulk motion, CGs, ECs, and PNS in several Magnetic Resonance Imaging (MRI) applications. These approaches include both acquisition-based and reconstruction-based methods, as described next:

- Bulk motion artifacts can be reduced through the gating of the Diffusion-Weighted (DW) acquisition (Taouli and Koh, 2009). Synchronizing the

Diffusion-Weighted Imaging (DWI) acquisition with the bulk physiological motion (e.g., using cardiac and/or respiratory triggering) reduces motion artifacts, although these methods generally increase the overall acquisition time (Murtz et al., 2002). Further, elastic motion can occur regionally throughout the entire cardiac or respiratory cycle, and therefore triggered acquisitions are generally unable to completely avoid motion artefacts. Sensitivity to bulk motion can be further reduced by applying diffusion-weighting gradient waveforms that guarantee first- and/or second-order moment-nulling (Ozaki et al., 2013; Simonetti et al., 1991; Stoeck et al., 2016). Traditionally, first-order moment-nulling (i.e., velocity compensation) has been achieved with bipolar waveforms (Ozaki et al., 2013), and second-order moment-nulling (i.e., acceleration compensation) with 'motion-compensated' diffusion encoding gradient waveforms (Stoeck et al., 2016). However, first- and second-order moment-nulled diffusion waveforms have typically resulted in substantial increases in the achievable Echo Times (TEs), leading to low Signal-to-Noise-Ratio (SNR) efficiency in these acquisitions.

- CG-effects can be minimized using multiple different approaches, including: post-processing-based methods (Norris and Hutchison, 1990), shimming coils (Sica and Meyer, 2007), image gradients dephasing (Baron et al., 2012), and application of symmetric diffusion-weighting gradient waveforms such as monopolar gradients (Zhou et al., 1998), or waveform reshaping to guarantee phase cancellation (Meier et al., 2008).

- Eddy Current (EC) artefacts are commonly reduced through shielding gradients and additional wiring (Bernstein et al., 2004; Le Bihan et al., 2006). The image distortions they introduce can be mitigated prospectively by, for example, adapting the k-space trajectories by taking into account the residual EC on the corresponding directions (Xu et al., 2013; Zhou et al., 1999). Further, calibration and reference scans can be used to eliminate them with post-processing methods (Haselgrove and Moore, 1996; Koch and Norris, 2000; Zhou, 1998). Gradient derating, complex MR sequences and tuned diffusion-weighting gradient waveforms can be also used to diminish the image distortions (Aliotta et al., 2018; Finsterbusch, 2009, 2010) with the advantage of also achieving intravoxel rephasing. Some of these correspond to the use of bipolar (Alexander et al., 1997) gradient waveforms in spin-echo DWI, or the implementation of the Twice Refocused Spin Echo (TRSE) DWI sequence (Reese et al., 2003). However, these methods tipically result in substancial increases in the achievable echo times (TEs), deacreasing the SNR and the efficiency of these acquisitions. On the other hand, the misestimation of the diffusion-weighting b-value can be compensated with gradient pre-emphasis (Le Bihan et al., 2006), although this increases hardware demands.

- Nerve stimulation is usually diminished by limiting the maximum slew rate and/or the maximum gradient strength of the gradient waveform leading to sub-optimal waveforms (Bernstein et al., 2004; Hidalgo-Tobon, 2010). Further, the gradient waveform shape, i.e., monopolar vs. bipolar, also plays and

important role in diminishing PNS (Ham et al., 1997; Harvey and Mansfield, 1994; Schulte and Noeske, 2015) as well as the gradient orientation and the patient's position (Abart et al., 1997; Den Boer et al., 2002).

Recently, Aliotta et al. (2017) proposed a novel algorithm, termed Convex Optimized Diffusion Encoding (CODE), to design gradient waveforms with first- and/or second-order moment-nulling. By formulating the gradient waveform design problem as a constrained nonlinear optimization problem (with constraints including sequence timing, hardware limits, and moment-nulling), CODE enables flexible design of gradient waveforms and seeks to minimize the achievable Echo Time (TE) for a desired b-value (or conversely, to maximize the achievable b-value for a given TE). By approximating this constrained optimization formulation as a convex (linear) optimization problem (instead of the original nonlinear, non-convex quadratic problem), CODE results in simplified computation. However, because of this approximation, it is unclear whether CODE results in optimal waveforms, i.e., whether it achieves the minimum TE for a given desired b-value. This optimality is critical for moment-nulled diffusion-weighting waveform design, as it will determine the SNR of the DWI acquisition, particularly for organs with relatively short T_2 relaxation time (e.g., the liver). Further, CODE waveforms are generally asymmetric around the refocusing pulse and the gradient amplifiers are switched fast to drive large gradient intensities. Therefore, they may suffer from substantial CG-, EC-, and PNS-effects, which need to be addressed.

Therefore, in this part of the Thesis dissertation we propose a novel Optimized Diffusion-weighting Gradient Waveform Design (ODGD) method for diffusion-weighting gradient waveform design for any diffusion-weighting direction that seeks to overcome the limitations of previous methods. The proposed ODGD method consists of: 1) a constrained optimization formulation that minimizes the TE for a given b-value subject to moment-nulling, CG-nulling, EC-nulling, and PNS-nulling constraints, and 2) a quadratic optimization algorithm that directly solves the formulation without introducing approximations. The proposed method is described and evaluated in phantoms and in-vivo brain and liver diffusion MRI experiments in Chapters 4 and 5. Specifically, in the following section we describe the underlying theory of ODGD, and in Chapter 4 we validate the proposed optimization formulation to achieve moment-nulling and CG-nulling, while in Chapter 5 we validate the proposed optimization formulation to achieve EC-nulling, and PNS-nulling.

3.2 Theory

The proposed Optimized Diffusion-weighting Gradient Waveform Design (ODGD) formulation seeks to optimize the TE for a given b-value, under various linear and nonlinear constraints. These constraints are listed below.

3.2.1 Moments

In order to refocus the signal from static spins, all diffusion-weighting gradient waveforms require zeroth-order moment-nulling (M_0). Additionally, diffusion-weighting gradient waveforms with high-order moment-nulling are desirable in tissues affected by physiological motion in order to avoid motion-related signal dephasing (importantly, this dephasing will result in artifactual signal decay in voxels that experience elastic tissue motion). These moment constraints can be expressed as follows (Welsh et al., 2015):

$$\mathrm{M_n} = \gamma \int_0^{T_{\mathrm{Diff}}} t^{\mathrm{n}} G(t) \partial t = 0 \quad \text{where} \quad \mathrm{n} = 0, 1, 2... \tag{3.1}$$

where γ is the gyromagnetic ratio, and G(t) and T_{Diff} are the diffusion-weighting waveform (G(t)= [G_{x}(t), G_{y}(t), G_{z}(t)]) and the diffusion-weighting time, respectively. Under this constraint, $\mathrm{M_0} = 0$ rephases the static spins, $\mathrm{M_1} = 0$ rephases the spins moving with uniform speed, and $\mathrm{M_2} = 0$ rephases the spins moving with uniform acceleration.

In the present Thesis dissertation:

- ODGD-$\mathrm{M_0}$ stands for ODGD with $\mathrm{M_0} = 0$.
- ODGD-$\mathrm{M_1}$ stands for ODGD with $\mathrm{M_0} = \mathrm{M_1} = 0$.
- ODGD-$\mathrm{M_2}$ stands for ODGD with $\mathrm{M_0} = \mathrm{M_1} = \mathrm{M_2} = 0$.

3.2.2 Concomitant Gradients

As indicated in Section 2.4 Concomitant Gradients (CGs) are well-known nonlinear spatially dependent magnetic fields that appear, as a consequence of Maxwell's equations for the curl and divergence, anytime we generate a magnetic field gradient (Bernstein et al., 1998). In conventional MRI scanners (Bernstein et al., 1998; Meier et al., 2008), these CGs are orthogonal to the diffusion-weighting gradients, and have significant first- and second-order spatially varying terms as follows:

$$\begin{aligned} B_c(x,y,z,t) = &\frac{1}{2\mathrm{B_0}}[(G_{\mathrm{x}}^2(t) + G_{\mathrm{y}}^2(t))z^2 + G_{\mathrm{z}}^2(t)\frac{x^2+y^2}{4} - \\ &G_{\mathrm{x}}(t)G_{\mathrm{z}}(t)xz - G_{\mathrm{y}}(t)G_{\mathrm{z}}(t)yz] \end{aligned} \tag{3.2}$$

where B_{c} is the CG magnetic field and $\mathrm{B_0}$ is the amplitude of the static magnetic field. Importantly, CGs are small near isocenter, and increase in magnitude away from isocenter. These nonlinear and spatially dependent magnetic fields can cause a phase accrual throughout the gradient diffusion-weighting time (T_{Diff}) given by:

$$\phi_c(x,y,z) = \gamma \int_0^{T_{\mathrm{Diff}}} B_c(x,y,z,t) \partial t \tag{3.3}$$

Therefore, the application of gradients leads to a spatially dependent dephasing of the MRI signal. This dephasing may cause a blurring of the k-space due to parabolic phase variations within the imaging plane, and a shifting of the k-space due to the cross-terms $G_{\mathrm{i}}G_{\mathrm{j}}$, so called in-plane dephasing (Baron et al., 2012). In addition, through-plane phase dispersion resulting from CGs (Baron et al., 2012) may cause severe signal attenuation. Further, this additional signal decay will be larger for increasing b-values, which may introduce bias in quantitative diffusion measures.

Consequently, in order to address the effects of CGs, the CG-related phase accrual can be nulled ($\phi_c(x, y, z) = 0$) by incorporating the following nonlinear constraint into the diffusion-weighting gradient waveform design formulation:

$$\gamma \int_{A_1} G(t)^2 \partial t - \gamma \int_{A_2} G(t)^2 \partial t = 0 \tag{3.4}$$

where A_1 and A_2 are the time periods before and after the refocusing radiofrequency pulse. By including this constraint, the effects of Eq. (3.2) can be mitigated over the entire Field-of-View (FOV), since the proposed correction of Eq. (3.4) is not spatially-dependent.

In the present Thesis dissertation:

- ODGD-$\mathrm{M_n}$-CG where n∈[0, 1, 2] stands for ODGD with nth order moment-nulling with Concomitant Gradient (CG)-nulling.

3.2.3 Eddy Currents

Eddy Currents (ECs) are time-varying magnetic field gradients generated according to the Faraday-Lenz Law of electromagnetism by conducting parts of the scanners such as gradient and Radio-Frequency (RF) coils Bernstein et al. (2004). They build up during the time-varying part of the gradient waveform and decay on the gradient constant portions and when gradients are off, as earlier introduced in Section 2.4. The ECs are proportional to the slew rate of the waveform and have opposite sign (Le Bihan et al., 2006). They are characterized by their impulse responses given by the following decaying exponential functions:

$$e(t, \tau) = H(t) \sum_n \alpha_n e^{\frac{t}{\tau_n}}, \tag{3.5}$$

where τ_n is the characteristic time constant, α_n is the characteristic amplitude, n is the number of induced currents and $H(t)$ is the step function. In standard MRI scanners, the ECs time constants can be in the range of few microseconds to hundred of seconds. ECs can introduce k-space shifting and unwanted phase accumulation. In traditional k-space imaging these effects do not affect the magnitude images; however, in rapid imaging such as Echo Planar Imaging (EPI) it can cause image scaling, shearing or shifting.

Consequently, in order to address the effects of the ECs, the ECs with a given set of time constants τ can be nulled by incorporating the following linear constraint

into the diffusion-weighting gradient waveform design formulation:

$$g(t,\tau) = \frac{\partial G(t)}{\partial t} * e(t,\tau)\Big|_{T_{\text{Diff}}} = 0, \tag{3.6}$$

In the present Thesis dissertation:

- ODGD-M_n-EC where n∈[0, 1, 2] stands for ODGD with nth order moment-nulling with Eddy Current (EC)-nulling.

3.2.4 Peripheral Nerve Stimulation

Nerve stimulation can be caused by the rapid switch of field gradients that may induce an electric depolarization and hence, stimulation of the nerves. These effects are more prone in modern scanners and in rapid imaging techniques due to the need to drive large gradient intensities quickly. Every nerve can be stimulated, however, the threshold for cardiac or respiratory stimulation is approximately ten times higher than the threshold for Peripheral Nerve Stimulation (PNS) (Schulte and Noeske, 2015). As such, limiting the Magnetic Resonance (MR) acquisitions to the PNS threshold is a cautious margin to avoid more harmful stimulations. A conservative nerve impulse response to study PNS is given by:

$$n(t) = \frac{\alpha \cdot c}{r(c+t)^2}, \tag{3.7}$$

where the gradient-coil specific constants α, r, and c are the effective coil length, rheobase, and chronaxie time, respectively. Thus, for waveforms designs with the maximum slew rate supported by the MRI unit we can reduce the nerve stimulation (PNS-nulling) by adding the linear constraint:

$$R(t) = n(t) * \frac{\partial G(t)}{\partial t} < \mathrm{P}_{\text{Limit}} = 1, \tag{3.8}$$

where the PNS limit ($\mathrm{P}_{\text{Limit}}$) is established by the International Electrotechnical Commission (IEC-60601-2-33).

In the present Thesis dissertation:

- ODGD-M_n-PNS where n∈[0, 1, 2] stands for ODGD with nth order moment-nulling with Peripheral Nerve Stimulation (PNS)-nulling.

3.2.5 Additional Constraints

DW-MRI sequences need to satisfy additional hardware constraints such as the limitation on the maximum gradient intensity (G_{Max}) and maximum slew rate (SR_{Max}) of each gradient axes (note that the effective G_{Max} and SR_{Max} may be increased for oblique diffusion directions, i.e., when several gradient axes are active simultaneously). Further, diffusion-weighting gradient waveforms need to be zero at certain times during the pulse sequence (e.g., during the RF pulses). In this

work, we will only focus on the constraints imposed by the Spin Echo (SE) DWI sequence shown in Figure 2.7 (Aliotta et al., 2017):

$$G(\mathrm{T_{RF-90}}) = 0 \tag{3.9}$$

$$G(\mathrm{T_{RF-180}}) = 0 \tag{3.10}$$

$$G(\mathrm{T_{EPI}}) = 0 \tag{3.11}$$

$$|G(t)| \leq \mathrm{G_{Max}} \tag{3.12}$$

$$\left|\frac{\partial G(t)}{\partial t}\right| \leq \mathrm{SR_{Max}} \tag{3.13}$$

where $\mathrm{T_{RF-90}}$ corresponds to the excitation pulse and $\mathrm{T_{RF-180}}$ corresponds to the refocusing pulse. $\mathrm{T_{EPI}}$ is the time needed by the EPI echo train to reach the center of k-space. In summary, the diffusion-weighting waveform may begin immediately after the excitation pulse, is zero during the refocusing pulse, and needs to finish before the beginning of the EPI echo train.

3.2.6 Proposed Formulation

The proposed ODGD formulation seeks to maximize the achievable b-value for a given TE. The b-value is given by

$$b = \gamma^2 \int_0^{T_{\mathrm{Diff}}} F(t)^2 \partial t \tag{3.14}$$

where

$$F(t) = \int_0^t G(\tau) \partial \tau \tag{3.15}$$

Therefore, the maximization is performed directly over the b-value formulation by optimizing the diffusion-weighting gradient waveform for any direction subject to the constraints in Eqs. (3.1)-(3.13). Hence, the objective function is formulated as follows:

$$G(t) = \arg\max_{G} b(G) \tag{3.16}$$

For the sake of clarity, Table 3.1 summarizes the constraints of the ODGD formulation. Note that G(t) can be a gradient waveform in any of the three axes, since there is no spatial dependence in the CG-nulling approach introduced in this work via Eq. (3.4). Importantly, it is generally of interest to minimize the TE for a given b-value (rather than to maximize the b-value for a given TE). To achieve the minimum TE for a given b-value, ODGD iteratively implements the maximization described in Eq. (3.16) at several TEs following a similar solution strategy as described in Figure 2 of Aliotta et al. (2017).

Table 3.1: Optimized Diffusion-weighted Gradient waveform Design (ODGD) formulation.

	ODGD Formulation
Pulse Sequence Constraints	$G(\mathrm{T_{RF-90}}) = 0 \quad \& \quad G(\mathrm{T_{RF-180}}) = 0 \quad \& \quad G(\mathrm{T_{EPI}}) = 0$
Hardware Constraints	$\lvert G(t)\rvert \leq \mathrm{G_{Max}} \qquad \& \qquad \left\lvert \frac{\partial G(t)}{\partial t} \right\rvert \leq \mathrm{SR_{Max}}$
Moment Constraint	$\mathrm{M_n} = \gamma \int_0^{T_{\mathrm{Diff}}} t^{\mathrm{n}} G(t) \partial t = 0 \quad \text{where} \quad \mathrm{n} = 0, 1, 2...$
Concomitant Gradients Constraint	$^{*}\ \gamma \int_{A_1} G(t)^2 dt - \gamma \int_{A_2} G(t)^2 dt = 0$
Eddy Currents Constraint	$g(t,\tau) = \frac{\partial G(t)}{\partial t} * e(t,\tau)\Big\rvert_{T_{\mathrm{Diff}}} = 0 \quad \text{where} \quad e(t,\tau) = H(t) \sum_n \alpha_n e^{\frac{t}{\tau_n}}$
PNS Constraint	$R(t) = n(t) * \frac{\partial G(t)}{\partial t} < P_{\mathrm{Limit}} \quad \text{where} \quad n(t) = \frac{\alpha c}{r(c+t)^2}$
b-value Formulation	$b = \gamma^2 \int_0^{T_{\mathrm{Diff}}} F(t)^2 dt \quad \text{where} \quad F(t) = \int_0^t G(\tau) d\tau$
Objective Function	$^{\dagger}\ G(t) = \arg\max_G b(G)$

* A_1 and A_2 are the time periods before and after the refocusing Radio Frequency pulse.
† G(t) is the diffusion-weighting gradient waveform.

3.2.7 Optimization Algorithm

In this work, Eq. (3.16) is directly solved using a Sequential Quadratic Programming (SQP) algorithm subject to upper and lower bounds (Eq. (3.12)), linear equality constraints (Eqs. (3.1), (3.6), and (3.9) - (3.11)), linear inequality constraints (Eqs. (3.8) and (3.13)), and a quadratic equality constraint (Eq. (3.4)). This optimization is performed in MATLAB (MathWorks, Natick, MA) using the *fmincon* built-in function. ODGD optimization MATLAB code is available for download from https://github.com/opennog/ODGD.

4

Validation of ODGD for Motion Compensation and Concomitant Gradient Nulling

Contents

4.1 Experimental work

In this Chapter we validate the performance of the Optimized Diffusion-weighting Gradient Waveform Design (ODGD) formulation introduced in previous Chapter 3. We focus on the validation of the proposed ODGD formulation to increase the

quality of the diffusion-weighted images and the corresponding diffusion-related parametric maps by reducing the artefacts introduced by the lengthy Diffusion-Weighted Imaging (DWI) acquisitions, patient motion, and the Concomitant Gradients (CGs).

4.1.1 ODGD Simulations

The performance of the proposed ODGD method and previous waveform designs were compared by assessing the Echo Time (TE) needed to achieve a given b-value for each waveform. Specifically, gradient waveforms were compared for a broad range of b-values (20 b-values in the range of 100 - 2000 s/mm^2 separated in steps of 100 s/mm^2). Additionally, because the achievable TE also depends on the time needed by the Echo Planar Imaging (EPI) echo train to reach the center of k-space (which will itself depend on the desired spatial resolution and degree of partial Fourier acquisition), different EPI readout times to the center of k-space (7 T_{EPI} readout times in the range of 16.4 - 46.4 ms separated in steps of 5 ms) were considered for each b-value. Diffusion-weighting gradient waveforms were designed using the following hardware and time constraints: excitation radiofrequency pulse duration of T_{RF-90} = 5.3 ms; refocusing pulse duration of T_{RF-180} = 4.3 ms; maximum gradient strength of G_{Max} = 49 mT/m; maximum slew rate of SR_{Max} = 100 T/m/s; unless otherwise stated, only one gradient axis was considered active for the computation of the b-values (note that Concomitant Gradient (CG)-effects will depend on the diffusion-weighting direction). All waveform designs were computed with a time resolution of 0.5 ms to optimize the waveforms in moderate computation times.

For each T_{EPI} and b-value, the following gradient waveforms were designed:

1. Monopolar (MONO) (Zhou et al., 1998).
2. BIPOLAR Ozaki et al. (2013).
3. Motion-Compensated (MOCO) diffusion-encoding gradient waveforms (Stoeck et al., 2016).
4. Three Convex Optimized Diffusion Encoding (CODE) (Aliotta et al., 2017) waveforms, one for each of the motion-nulling moments (CODE-M_n, where n = 0, 1, 2).
5. the proposed ODGD formulation for each of the motion-nulling moments (ODGD-M_n, where n = 0, 1, 2) without and with CG-nulling (ODGD-M_n-CG, where n = 0, 1, 2).

Crusher gradients around the refocusing radiofrequency pulse were not included in the design of ODGD or Convex Optimized Diffusion Encoding (CODE) waveforms for non-zero b-values. In this study, the optimization algorithm for ODGD-M_n waveforms was initialized with a constant waveform, and the optimization of ODGD-M_n-CG waveforms was initialized with the corresponding ODGD-M_n waveform. Figure 4.1 shows examples of each of the waveforms designed for the experiments

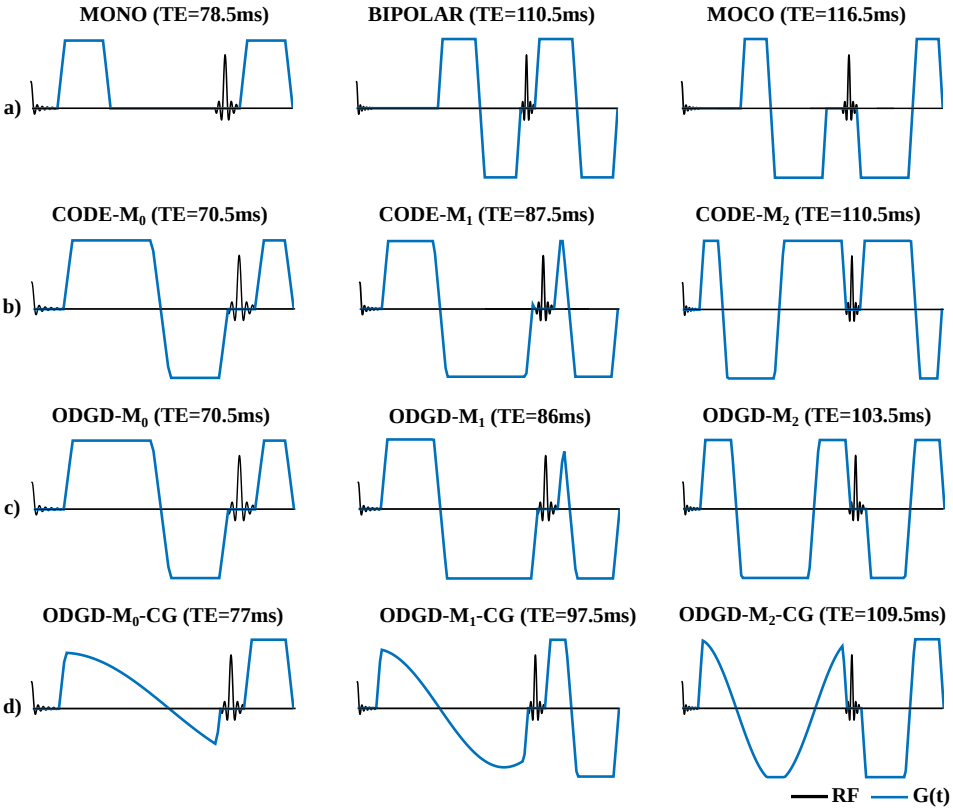

Figure 4.1: Set of diffusion-weighting gradient waveforms. Traditional waveforms (a), Convex Optimized Diffusion Encoding (CODE) gradient waveforms (b), and Optimized Diffusion-weighting Gradient Waveform Designs (ODGD) without (c) and with (d) Concomitant Gradients (CGs) nulling for b = 1000 s/mm^2 and T_{EPI} = 26.4 ms. CODE and ODGD waveforms without and with CG-nulling reduced the TE of the traditional waveforms (MONO, BIPOLAR, and MOCO) in all cases. These traditional waveforms have equivalent or symmetric shapes before and after the refocusing pulse, and therefore lead to dead times between the Radio Frequency (RF) pulses (due to the need for additional time for the EPI readout between the end of the diffusion waveform and the echo time). In contrast, the CODE framework and the ODGD formulation seek to use the available time optimally in order to minimize the TE. Note that the ODGD-based diffusion gradients have the same waveform along the three main gradient axes, although generally with different scaling depending on the diffusion direction. Therefore, only one gradient axis is considered active for the optimization of these waveforms.

grouped as traditional designs, CODE waveforms, and ODGD waveforms without and with CG-nulling.

4.1.2 Evaluation of SNR Increase

4.1.2.1 Acetone phantom experiments

A ten-vial acetone-based diffusion phantom was constructed using mixtures of pure acetone (as a signal source), H_2O (to control the Apparent Diffusion Coefficient (ADC) of acetone without producing Magnetic Resonance (MR) signal), and $MnCl_2$ (to control the T_2 of acetone) (Wang et al., 2017). The total volume of mixture in each vial was of 50 ml. The ten vials were designed to form two T_2 groups of approximately 40 and 90 ms, respectively, with five different ADC values each. Specific vial compositions and expected approximate ADC values included:

1. 19.38 mM of $MnCl_2$ with a 9% v/v of H_2O for ADC = 2.1×10^{-3} mm^2/s.
2. 8.42 mM of $MnCl_2$ with a 9% v/v of H_2O for ADC = 2.1×10^{-3} mm^2/s.
3. 17.50 mM of $MnCl_2$ with a 12% v/v of H_2O for ADC = 1.8×10^{-3} mm^2/s.
4. 7.60 mM of $MnCl_2$ with a 12% v/v of H_2O for ADC = 1.8×10^{-3} mm^2/s.
5. 15.94 mM of $MnCl_2$ with a 15% v/v of H_2O for ADC = 1.5×10^{-3} mm^2/s.
6. 6.92 mM of $MnCl_2$ with a 15% v/v of H_2O for ADC = 1.5×10^{-3} mm^2/s.
7. 13.89 mM of $MnCl_2$ with a 20% v/v of H_2O for ADC = 1.2×10^{-3} mm^2/s.
8. 6.03 mM of $MnCl_2$ with a 20% v/v of H_2O for ADC = 1.2×10^{-3} mm^2/s.
9. 11.02 mM of $MnCl_2$ with a 30% v/v of H_2O for ADC = 0.9×10^{-3} mm^2/s.
10. 4.78 mM of $MnCl_2$ with a 30% v/v of H_2O for ADC = 0.9×10^{-3} mm^2/s.

The number before the $MnCl_2$ concentration represents the vial number.

Diffusion-weighted images of the diffusion phantom were acquired under 0°C ice-water bath with an eight-channel head coil in a 3T scanner (MR 750, GE Healthcare, Waukesha, WI). The specific constraints of the optimization formulation are T_{EPI} = 23 ms, T_{RF-90} = 5.5 ms, T_{RF-180} = 6 ms, G_{Max} = 49 mT/m and SR_{Max} = 100 T/m/s. Twelve different diffusion-weighting gradient waveforms with these constraints were designed with MONO, BIPOLAR, MOCO, CODE-M_n (n = 0, 1, 2), ODGD-M_n (n = 0, 1, 2) and ODGD-M_n-CG (n = 0, 1, 2), respectively. Axial images were acquired using different waveforms with Field-of-View (FOV) = 26 × 26 cm, in-plane resolution = 2.0 × 2.0 mm, slice thickness = 5 mm, Repetition Time (TR) = 6 s, parallel imaging acceleration of 2 and no partial-Fourier acquisitions. Diffusion encoding was performed in all three orthogonal directions with b-values = [100(1), 400(1), 600(2), 800(4), 1000(6)] s/mm^2, where the number in brackets represents the number of averages for each b-value. Note that crusher gradients are not used around the refocusing Radio-Frequency (RF) pulse in any of the implementations of this chapter.

In order to perform T_2 mapping, 2D Spin Echo (SE) images were acquired with FOV = 26 × 15.6 cm, matrix size of 256 x 160, slice thickness of 10 mm, TR = 2 s, parallel imaging acceleration factor of 2, and TE = [6, 20, 60, 120, 240] ms. T_2 measurements were obtained in order to fully describe the acetone phantom used in the experiments, as well as to be able to further characterize the Signal-to-Noise-Ratio (SNR) values of each vial. T_2 maps were estimated with least squares fitting.

In order to compare SNR across different acquisitions, SNR maps were calculated for each acquisition using a Rician non-stationary noise model (Aja-Fernández and Vegas-Sánchez-Ferrero, 2016), with spatially-varying noise standard deviation $\sigma(\boldsymbol{x})$. SNR maps were computed from the averaged composite magnitude images (e.g., complex images from different coils merged into one single magnitude image) using a Rician expectation–maximization estimator (Aja-Fernández et al., 2015; DeVore et al., 2000):

$$\mathrm{SNR}(\boldsymbol{x}) = \frac{\widehat{A(\boldsymbol{x})}}{\widehat{\sigma(\boldsymbol{x})}}, \tag{4.1}$$

where $\widehat{A(\boldsymbol{x})}$ and $\widehat{\sigma(\boldsymbol{x})}$ are the estimates of the signal amplitude and noise standard deviation, respectively, obtained from an iterative process (Aja-Fernández et al., 2015). Local parameters were estimated using 3 × 3 windows and a total of 20 iterations. For the evaluation of SNR, a 0.9 cm^2 Region of Interest (ROI) was drawn in each vial, co-localized across the different acquisitions.

4.1.2.2 In-vivo acquisitions

This study including healthy volunteers was performed with Institutional Review Board (IRB) approval and informed written consent.

Brain DWI: Ten healthy volunteers were recruited for brain DWI. Brain DWI was acquired with the same waveform designs and constraints as the diffusion phantom experiment described in the previous section with the eight-channel head coil, and on the same 3T scanner. The acquisition parameters were FOV = 26 × 26 cm, in-plane resolution = 2.0 × 2.0 mm, slice thickness = 5 mm, TR = 2.5 s, parallel imaging acceleration factor = 2 and full k-space acquisitions. Diffusion encoding was performed in all three directions with b-values(averages) = [100(1), 200(1), 600(2), 800(4), 1000(6)] s/mm^2. SNR maps were calculated with Eq. (4.1). For SNR analysis, four circular ROIs of size 38 - 50 mm^2 were drawn in the left and right cerebral white matter. ROIs in the images from different acquisitions were co-localized and SNR measurements within each subject were averaged prior to statistical comparison between different waveforms (see 'Statistical Analysis', Section 4.1.4 below for details).

Liver DWI: Ten healthy volunteers were scanned with a 30-channel torso coil (GE Healthcare, Waukesha, WI) in the same 3T scanner for liver DWI. Slices covering the superior portion of the liver, including through the right and left lobes were acquired. Full liver coverage was not obtained due to time constraints

for the acquisition. The constraints used for the waveform optimization were T_{EPI} = 18.5 ms, T_{RF-90} = 5.5 ms, T_{RF-180} = 6.5 ms, G_{Max} = 49 mT/m, and SR_{Max} = 100 T/m/s. Different diffusion-weighting gradient waveforms with these parameters were designed with MONO, MOCO, CODE-M_2, ODGD-M_2 and ODGD-M_2-CG. Axial images were acquired with respiratory triggering. Other acquisition parameters are FOV = 36 × 36 cm, in-plane resolution = 2.8 × 2.8 mm, slice thickness = 6 mm, parallel imaging factor of 2 and full k-space acquisitions. Diffusion encoding was performed in the R/L direction with b-values (averages) = [100(4), 500(10)] s/mm^2. SNR maps were calculated with Eq. (4.1) and ADC maps were estimated with least-squares fitting. For SNR analysis, circular ROIs of 50 - 100 mm^2 were drawn on the superior portion of the liver in segments VII and VIII of the right lobe, and segment IV of the left lobe. For each waveform, SNR measurements within each subject were averaged prior to statistical comparison between different waveforms. For motion compensation analysis, one ROI was set on segment II since it is typically severely impacted by cardiac motion and might contain signal voids with traditional diffusion waveforms. Care was taken to avoid large vessels and blurred regions. Further, to measure liver T_2, a multi-TE multi-TR Stimulated Echo Acquisition Mode (STEAM) sequence (Hamilton et al., 2015) with voxel size of 20 × 20 × 20 mm was applied to all volunteers on the right lobe of the liver carefully avoiding large vessels.

4.1.3 Evaluation of CG-nulling

4.1.3.1 Simulations and phantom experiments

Water phantom simulations: Simulations were performed in a synthetic water phantom with full k-space acquisition and same FOV, in-plane resolution, slice thickness, and waveform designs as the acetone phantom experiments. CG-related signal dephasing effects for different diffusion-weighting directions were simulated, including x, y, z, x-y, x-z, y-z and x-y-z to assess the through-plane dephasing effects. Further, the synthetic water phantom approximated the shape, dimensions and ADC value (2×10^{-3} mm^2/s) of the following water phantom, which is described next.

Water phantom: A 7.5 L cylindrical water phantom doped with NaCl and $NiCl_2$ (Imaging, 1997) was imaged at room temperature with the same acquisition setup and the same waveform designs as the acetone phantom experiment to evaluate the CG correction effect. Seven diffusion-weighting directions were acquired, including x, y, z, x-y, x-z, y-z and x-y-z. Coverage in the slice (z) inferior-direction of 12 cm was applied to evaluate the slice dependent CG-effect, especially for slices that are away from the isocenter. ADC maps were estimated for each diffusion-weighting direction and for each diffusion-weighting waveform with a maximum likelihood estimator (Sijbers et al., 1998).

4.1.3.2 In-vivo acquisitions

Brain DWI: Average trace ADC maps were estimated from trace Diffusion-Weighted (DW) images from the previously described brain DW acquisitions with a maximum likelihood estimator (Sijbers et al., 1998). Hereinafter in this Chapter, the average trace ADC map and the trace DW images are denoted as ADC maps and DW images, respectively. ROIs measured within slices between 4.5 and 7 cm from isocenter (among the ROIs drawn on the previously described brain DW acquisitions) were considered to assess the effect of CG-related bias in ADC measurements. For each waveform, ADC measurements within each subject were averaged prior to statistical comparison between different waveforms.

4.1.4 Statistical Analysis

All ROIs of the phantom experiments were first tested for normality using the Kolmogorov-Smirnov test. Homoscedasticity across variances was then tested using the Ansari-Bardley test. If both tests yielded normality and homoscedasticity, pairwise comparisons were made between co-localized ADC acquired with different waveforms using the one-way sample t-test. From these comparisons, p-value < 0.05 (P) was considered significant. Similarly, for each waveform of the in-vivo experiments, all ROI SNR and ADC measurements within each subject were averaged and then tested using the same analysis as in the phantom experiments.

4.2 Results

4.2.1 ODGD Simulations

ODGD waveforms reduce or equalize the minimum TE of the traditional (MONO, BIPOLAR, and MOCO) and recently proposed waveforms (CODE-M_n, where n = 0, 1, 2) for any given b-value, EPI readout time, and moment-nulling order. ODGD with CG-nulling constraints also results in shorter TE compared to the traditional waveforms. The relationship between previously proposed CODE versus the proposed ODGD solution depends on the specific constraints: CODE waveforms are sometimes the same as ODGD, sometimes a different local optimum resulting in a longer TE, and sometimes not even a local optimum (results not shown). The residues achieved by the ODGD optimization in terms of b-value and CG dephasing are null (up to our numerical precision). Computation times of ODGD ranged between a few seconds for low b-value and zeroth-order moment-nulling (ODGD-M_0) to ≈10 minutes for high b-values, second-order moment-nulling, and CG-nulling (ODGD-M_2-CG).

Moment Constraints ODGD-M_n, where n=0,1,2, outperforms the traditional waveforms as well as the recently proposed CODE-M_n gradient waveforms as shown in Figure 4.2. Figure 4.2.a) depicts the optimal TE for a range of b-values and T_{EPI} = 26.4 ms. Figure 4.2.b) shows the TE difference between CODE-M_n and

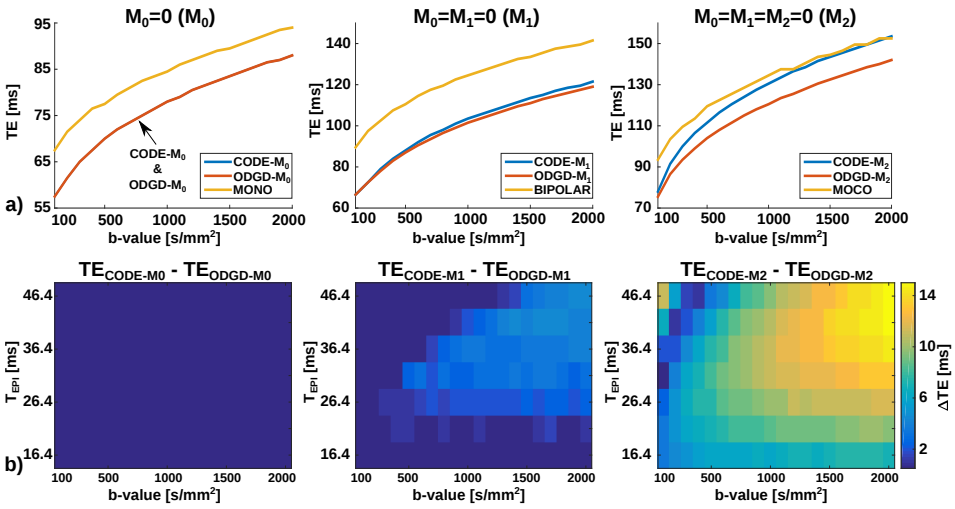

Figure 4.2: Minimum TE achieved for the range of b-values 100 - 2000 s/mm^2 in steps of 100 s/mm^2 and T_{EPI} (EPI readout time to the center of k-space) of 26.4 ms for ODGD-M_n, CODE-M_n, and the traditional waveforms (MONO, BIPOLAR, and MOCO) for different moment constraints, M_0, M_1, and M_2, respectively (a). TE reduction (ΔTE) achieved using ODGD-M_n compared to CODE-M_n for the same range of b-values and T_{EPI} in the range of 16.4 - 46.4 ms in steps of 5 ms (b). There is no TE reduction ($\Delta TE = 0$) for zeroth-order moment-nulling (M_0), but there is TE reduction for first- and second-order moment-nulling (M_1 and M_2, respectively). The TE reduction is greater for higher b-values, longer T_{EPI}, and higher-order moment-nulling. Note that only one gradient axis is considered active for the optimization of these waveforms.

ODGD-M_n waveforms for the range T_{EPI} = 15 - 50 ms. There is no TE reduction of ODGD-M_0 compared to CODE-M_0, but there is a TE reduction between 0 - 3.57% for M_1, and between 0.63 - 10.14% for M_2. Relative to the traditional waveforms, ODGD results in TE reductions between 1.91 - 17.84% compared to MONO, 9.20 - 29.22% compared to BIPOLAR, and 1.88 - 26.97% compared to MOCO.

Concomitant Gradients Constraints ODGD-M_n-CG, where n=0,1,2, reduces the TE of traditional CG-compensated waveforms (MONO, BIPOLAR, and MOCO, which cancel the CG phase accrual due to their symmetry around the RF_{180}), as illustrated in Figure 4.3. Figure 4.3.a) shows the minimum TE achieved for a given range of b-values and T_{EPI} = 26.4 ms of the traditional waveform designs and the proposed ODGD waveforms. Figure 4.3.b) shows the difference between the minimum TE achieved by the traditional and ODGD waveforms for the same range of b-values and T_{EPI} = 15 - 50 ms. Namely, ODGD-M_n-CG, where n = 0, 1, 2, results in TE reductions between 0 - 4.02% compared to MONO, 7.53 - 16.74% compared to BIPOLAR, and 0.77 - 12.54% compared to MOCO.

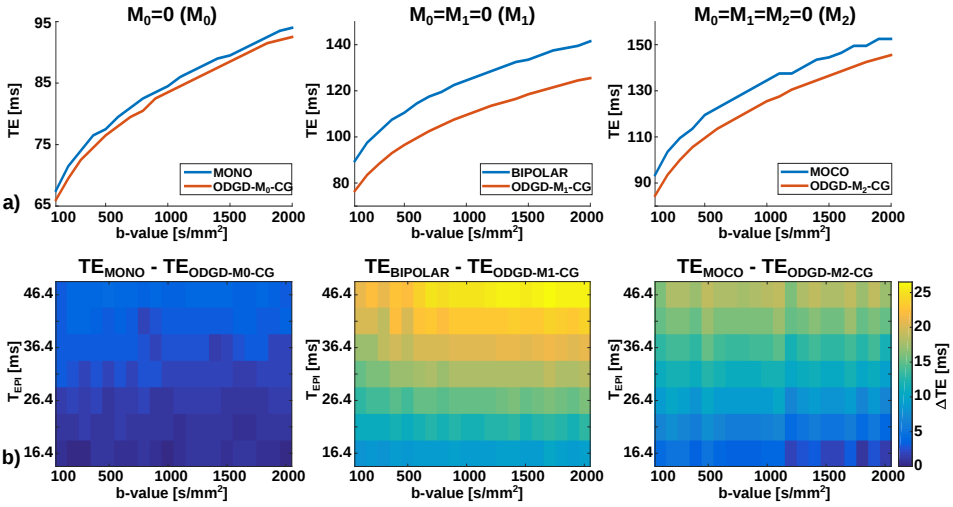

Figure 4.3: Minimum TE achieved for a range of b-values 100 - 2000 s/mm^2 in steps of 100 s/mm^2 and T_{EPI} (EPI readout time to the center of k-space) of 26.4 ms for ODGD-M_n-CG and the traditional waveforms (MONO, BIPOLAR, and MOCO) for different moment constraints, M_0, M_1, and M_2, respectively (a). TE reduction (ΔTE) achieved using ODGD-M_n-CG compared to the traditional waveforms for the same range of b-values and T_{EPI} in the range of 16.4 - 46.4 ms in steps of 5 ms (b). ΔTE is larger for higher b-values and T_{EPI}, and larger for the M_1 constraint than for M_0, or M_2. Note that only one gradient axis is considered active for the optimization of these waveforms.

4.2.2 Evaluation of SNR Increase

4.2.2.1 Acetone phantom experiments

Experimentally measured T_2 are 39.5±0.7 and 83.5±1.5 ms, and measured ADC in a slice at the isocenter with respect to each of the T_2 and vial number are 1) 2.22±0.16 and 2) 2.28±0.02 × 10^{-3} mm^2/s, 3) 1.99±0.09 and 4) 1.94±0.02 × 10^{-3} mm^2/s, 5) 1.69±0.07 and 6) 1.69±0.02 × 10^{-3} mm^2/s, 7) 1.36±0.06 and 8) 1.35±0.01 × 10^{-3} mm^2/s, and 9) 0.84±0.06 and 10) 0.92±0.02 × 10^{-3} mm^2/s. No bias was found in these ADC measurements.

There is a 6% TE reduction in ODGD-M_2 over CODE-M_2 (TE: 118.5 ms and 126.5 ms, respectively), which generally increases the SNR in each of the diffusion phantom vials, as shown in Figure 4.4. Mean SNR for each of the vials is T_2 and ADC dependent, but there is an increase of 4%, -15%, 18%, 44%, 11% for each of the vials with T_2 = 39.5±0.7 ms (vial numbers 1, 3, 5, 7 and 9, respectively), and 29%, -4%, 25%, 17%, 8% for each of the vials with T_2 = 83.5±1.5 ms (vial numbers 2, 4, 6, 8 and 10, respectively) as shown in Figure 4.4.c)-d). Statistical significance ($P < 0.05$) is found in every vial pairwise comparison except for vial 4) $T_2 \approx 83.5$ ms and ADC = 1.94±0.02 × 10^{-3} mm^2/s. ODGD-M_0 and ODGD-M_1 waveforms are the same as the corresponding CODE waveforms under the implemented spatial resolution (T_{EPI} = 23.32 ms), achieving no TE reduction, and therefore no SNR increase.

4.2.2.2 In-vivo acquisitions

Brain DWI: Brain DWI results, including SNR and ADC measurements, are shown in Figure 4.5. ODGD-M_1 and ODGD-M_1-CG reduce the TE by 16.3% and 10.9% as compared with BIPOLAR (BIPOLAR: 119.5 ms, ODGD-M_1-CG: 106.5 ms, ODGD-M_1: 100.0 ms). There is no TE reduction of ODGD-M_1 compared to CODE-M_1. The TE reduction relative to BIPOLAR results in visually apparent increased signal (see Fig. 4.5.a)). ODGD-M_1 leads to higher SNR than BIPOLAR and ODGD-M_1-CG, $P < 1$ x 10^{-6} and $P < 0.05$, respectively. ODGD-M_1-CG also leads to higher SNR than BIPOLAR with $P < 0.005$.

Liver DWI: The results from the liver acquisitions, with mean measured liver T_2 = 24.38±11.4 ms, are shown in Figures 4.6 and 4.7. ODGD-M_2 and CODE-M_2 waveforms result in ADC maps that are visually more homogeneous than MONO, suggesting higher motion robustness (see Fig. 4.6). ADC values on a ROI on segment II of the liver of a representative volunteer are 2.46±0.38 × 10^{-3} mm^2/s for MONO, 1.85±0.2 × 10^{-3} mm^2/s for CODE-M_2, and 1.53±0.21 × 10^{-3} mm^2/s for ODGD-M_2.

ODGD-M_2 increases the TE by 47.7% as compared to MONO (from 65.3 to 96.5 ms). ODGD-M_2 (TE = 96.5 ms) reduces the TE by 8.5% and 6% as compared with MOCO (105.5 ms) and CODE-M_2 (102.5 ms), respectively. ODGD-M_2-CG (TE = 99 ms) reduces the TE by 6% and 3.5% as compared with MOCO and CODE-M_2. This TE reduction results in visually apparent increased diffusion-weighted signal

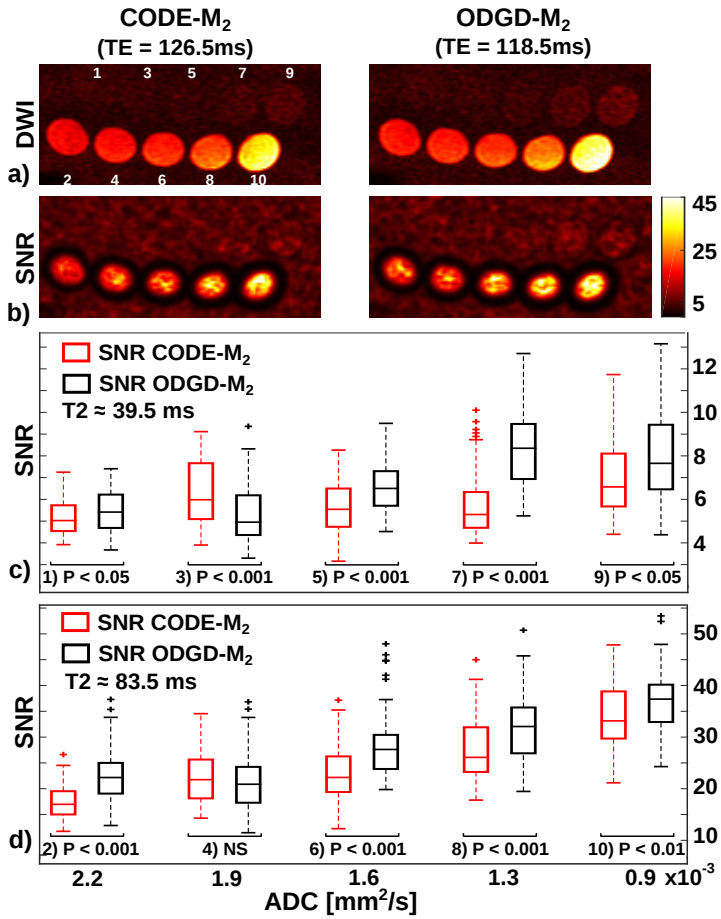

Figure 4.4: Diffusion-weighted images of the acetone phantom experiments acquired with CODE-M_2 and ODGD-M_2 at b-value 1000 s/mm^2 in a slice at the isocenter of the magnet (a). SNR of the same images (b). Top row of the set of 10 vials have short $T_2 \approx 39.5$ ms (vial numbers 1, 3, 5, 7, 9), and bottom row have long $T_2 \approx 83.5$ ms (vial numbers 2, 4, 6, 8, 10). Distribution of the SNR values of each vial grouped by $T_2 \approx 39.5$ ms (c), and $T_2 \approx 83.5$ ms (d). From left to right, distributions are ordered as vials in (a). Red boxes show the distribution of CODE-M_2 and black boxes the distribution of ODGD-M_2. There is a statistically significant ($P < 0.05$) SNR increase for every vial of ODGD-M_2 compared to CODE-M_2 except for vials with ADC = 1.9×10^{-3} mm^2/s.

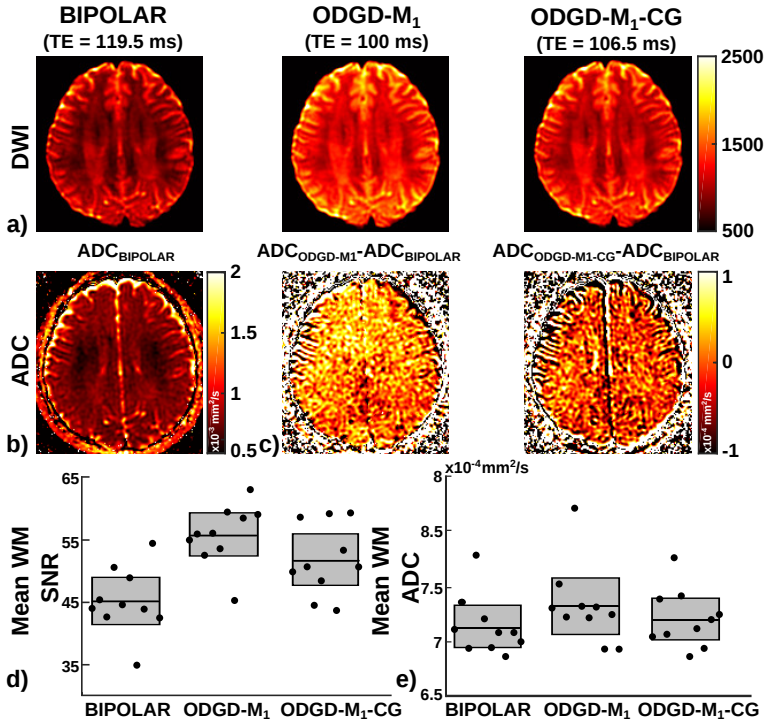

Figure 4.5: Axial trace diffusion-weighted images (DWI) acquired at 4.5 cm from isocenter of a representative brain are shown acquired with BIPOLAR, ODGD-M_1, and ODGD-M_1-CG with a b-value of 100 s/mm^2 (a). Corresponding average trace ADC map of the BIPOLAR acquisition (b). ODGD-M_1 and ODGD-M_1-CG average trace ADC maps pixelwise subtracted with the BIPOLAR average trace ADC map (c). Mean ± 95% CI SNR values of the trace DW images (d), and average trace ADC values (e) across ROIs set on white matter of the 10 volunteers. ODGD-M_1 leads to higher statistically significant SNR than BIPOLAR and ODGD-M_1-CG, $P < 1$ x 10^{-6} and $P < 0.05$, respectively. ODGD-M_1-CG also leads to statistically significant higher SNR than BIPOLAR with $P < 0.005$. ODGD-M_1 average trace ADC map is positively biased ($P < 0.005$) with respect to BIPOLAR. There is no statistically significant difference between the average trace ADC maps of ODGD-M_1-CG and BIPOLAR. Note that for this set of waveforms ODGD-M_1 and CODE-M_1 are the same.

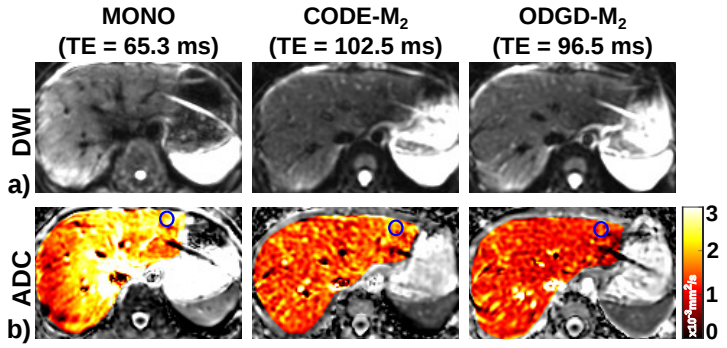

Figure 4.6: Axial diffusion-weighted images of a representative liver are shown acquired with MONO, CODE-M_2, and ODGD-M_2 with a b-value of 500 s/mm^2 (a). Corresponding ADC maps (b). MONO ADC maps have heterogeneous positive bias throughout the liver due to intravoxel signal dephasing at b-value of 500 s/mm^2 produced by bulk motion. ODGD-M_2 and CODE-M_2 waveforms achieve more spatially homogeneous DW images and ADC maps than MONO, showing better motion robustness. ADC values on a ROI on segment II of the liver (blue ROI) of a representative volunteer are 2.46±0.38 × 10^{-3} mm^2/s for MONO, 1.85±0.2 × 10^{-3} mm^2/s for CODE-M_2, and 1.53±0.21 × 10^{-3} mm^2/s for ODGD-M_2.

and SNR (Fig. 4.7). ODGD-M_2 and ODGD-M_2-CG have significantly higher SNR than MOCO and CODE-M_2 (ODGD-M_2 = 12.3±3.6, ODGD-M_2-CG = 12.0±3.5 versus MOCO = 9.7±2.9 and CODE-M_2 = 10.2±3.4, both with $P < 0.05$). There is no statistically significant difference between the SNRs of ODGD-M_2 and ODGD-M_2-CG.

4.2.3 Evaluation of CG-nulling

4.2.3.1 Water phantom simulations and experiments

Figure 4.8 shows the in-plane CG-related dephasing effects for the x-y-z diffusion-weighting gradient direction in the water phantom experiments. ODGD-M_0 suffers from diffusion-weighting direction-dependent k-space shifting at the slice 4.5 cm from isocenter. Further, it also shows that ODGD-M_0 suffers from k-space blurring (i.e., larger full-width-half-maximum along the y direction, FWHMy) at isocenter (0 cm) and at 4.5 cm from isocenter. In contrast, MONO and ODGD-M_0-CG suffer from slight k-space shifting and their FWHMy is similar at both slice positions.

From simulations and phantom experiments, through-plane dephasing effects produced by CGs are demonstrated in Figure 4.9. Figure 4.9.b) and c) show the direction-dependent patterns of ADC bias produced by the CG-effects of ODGD-M_1 waveforms in simulations and in the water phantom experiments. Importantly, BIPOLAR and ODGD-M_1-CG waveforms, both with CG-nulling, show improved homogeneity of ADC maps and tightly distributed histograms around the expected

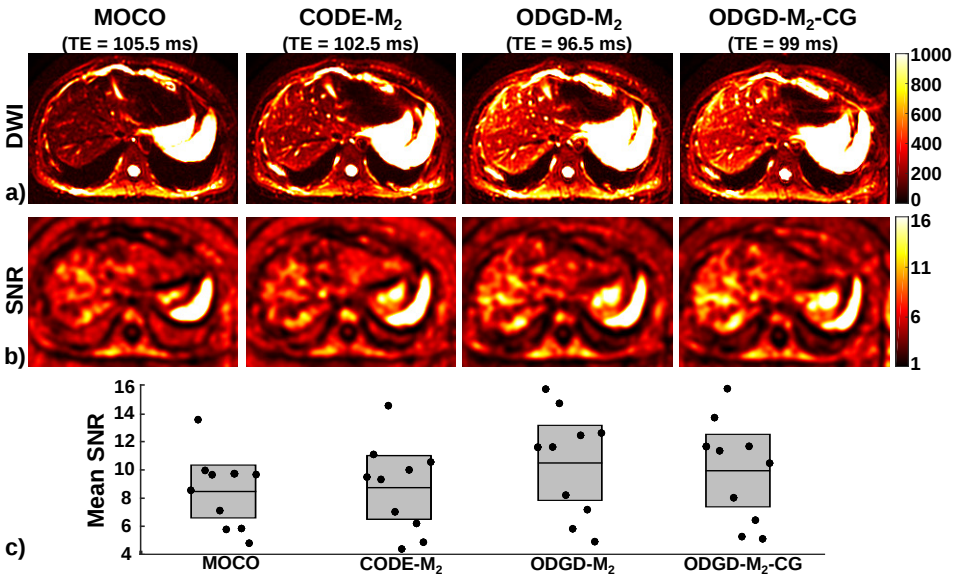

Figure 4.7: Axial diffusion-weighted images of the liver are shown acquired with MOCO, CODE-M_2, ODGD-M_2, and ODGD-M_2-CG with a b-value of 100 s/mm^2 (a). Signal-to-noise ratio (SNR) maps of these acquisitions (smoothed with an average filter for better representation) (b). Liver SNR measurements in the 10 volunteers, for each of the diffusion waveforms (c). ODGD-M_2 and ODGD-M_2-CG lead to statistically significant ($P < 0.05$) higher SNR than MOCO and CODE-M_2. There is no statistically significant difference between ODGD-M_2 and ODGD-M_2-CG.

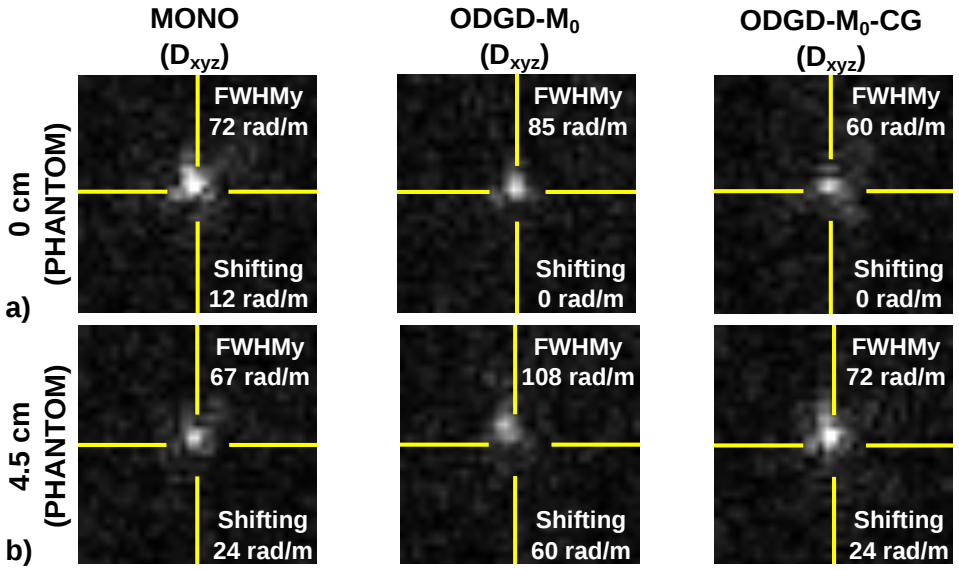

Figure 4.8: Cropped k-space of the water phantom experiments of slices at isocenter (0 cm) and 4.5 cm from isocenter with MONO, ODGD-M_0, and ODGD-M_0-CG, b-value of 1000 s/mm^2, and diffusion-weighting direction D_{xyz}, (a) and (b), respectively. FWHMy indicates the full-width-half-maximum along the phase-encoding direction (y-axes). Shifting indicates the displacement of the k-space from its center. ODGD-M_0 shows broader FWHMy than MONO and ODGD-M_0-CG, and k-space shifting towards the upper left corner at 4.5 cm from isocenter. MONO and ODGD-M_0-CG show little blurring and no k-space shifting. Note that for this set of waveforms ODGD-M_0 and CODE-M_0 are the same.

room-temperature water diffusion coefficient (nearly 2×10^{-3} mm^2/s).

4.2.3.2 In-vivo acquisitions

Brain DWI: ADC results from the brain acquisitions are shown in Figure 4.5. The ADC map of ODGD-M_1 pixelwise subtracted from the BIPOLAR ADC map shows visually positive general bias (see Fig. 4.5.c)). No bias is apparent in the pixelwise subtraction of ODGD-M_1-CG and BIPOLAR ADC maps. ODGD-M_1 leads to statistically significant higher ADC than BIPOLAR ($P < 0.005$) while there is no statistically significant difference between the ADC measured from ODGD-M_1-CG versus BIPOLAR (BIPOLAR ADC = 0.71±0.02 x 10^{-3} mm^2/s, ODGD-M_1 ADC = 0.73±0.03 x 10^{-3} mm^2/s, and ODGD-M_1-CG ADC = 0.71±0.01 x 10^{-3} mm^2/s)

4.3 Discussion

We have presented a novel Optimized Diffusion-weighting Gradient Waveform Design (ODGD) formulation as a quadratic constrained optimization problem. The ODGD formulation allows the design of diffusion-weighting gradient waveforms to diminish bulk motion effects and null Concomitant Gradient (CG) effects while minimizing the TE of diffusion-weighted acquisitions. ODGD equalized or reduced the achievable TE compared to the traditional moment-nulled waveforms and the recently proposed Convex Optimized Diffusion Encoding (CODE) formulation. Generally, TE reductions are greater at higher b-values, k-space resolutions (i.e., longer T_{EPI}), and high-order moment-nulling. This TE reduction may enable increased signal-to-noise ratio in Diffusion-Weighted Magnetic Resonance Imaging (DW-MRI) by avoiding T_2-related signal losses. Additionally, optimized motion-compensated waveforms have been implemented in a different Magnetic Resonance Imaging (MRI) vendor and platform from the previous implementation (Aliotta et al., 2017) demonstrating feasibility and reproducibility of optimized motion-compensated diffusion waveforms on different platforms.

Motion-compensated waveforms have promising applications in organs that experience substantial physiological motion, such as heart or liver, by enabling improved DW image quality and improved accuracy of quantitative diffusion parameter maps (Murphy et al., 2013). Further, CG-nulling waveforms may be important for quantitative diffusion imaging in applications requiring a large anatomical coverage, when implementing partial Fourier acquisitions, and for Diffusion Tensor Imaging (DTI) acquisitions. In addition, improvements on multi-shot DW-EPI (Chen et al., 2013; Holdsworth et al., 2008) might be achieved by using ODGD-M_n waveforms due to the potential for reduced motion-induced phase variations across multiple shots.

It has been shown that ODGD-M_n results in equal or shorter TE than CODE-M_n for a given b-value. This TE reduction is likely due to the direct solution of the nonlinear optimization problem for gradient waveform design in ODGD, compared

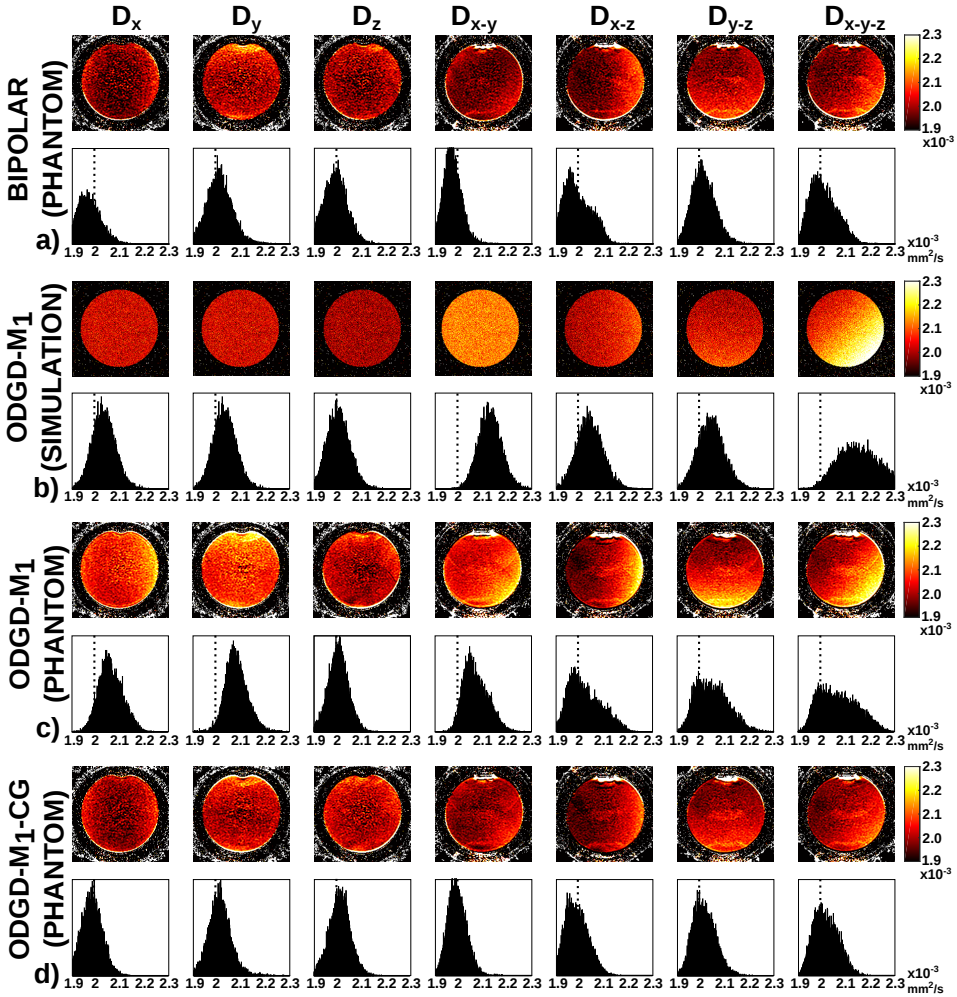

Figure 4.9: Measured ADC maps along each gradient direction combination (D_n) of the water phantom experiment with the BIPOLAR waveform (a). Measured ADC maps of the simulated acquisition of the water phantom experiment for ODGD-M_1 (b). Measured ADC maps of the waveforms ODGD-M_1 (c) and ODGD-M_1-CG (d). The reference ADC value of 1.98×10^{-3} mm^2/s, dotted line, was measured as the average of D_x, D_y and D_z of the BIPOLAR acquisition. Acquisitions with BIPOLAR and ODGD-M_1-CG waveforms considerably reduced the bias of the ADC maps introduced by the concomitant gradients. Note that for this set of waveforms ODGD-M_1 and CODE-M_1 are the same.

to the approximate linear formulation of the objective function used in (Aliotta et al., 2017). CG-nulling waveforms also shortened the achievable TE compared to the traditional symmetric MONO, BIPOLAR, and MOCO waveforms. This was likely achieved due to the elimination of dead times between radiofrequency pulses leading to more efficient use of the diffusion encoding time. Interestingly, the proposed CG-nulling formulation leads to novel smoothed asymmetric waveforms with the same squared area before versus after the refocusing RF pulse.

This work has several limitations. For oblique diffusion-weighting directions, ODGD-CG restricts the waveforms along each axis to be scaled versions of the optimized G(t) waveform. Also, the proposed formulation does not consider the contribution to the b-value of the imaging gradients (Güllmar et al., 2005), although this contribution is often not accounted for in the design of diffusion-weighting gradient waveforms. Further, in this work the computation of ODGD waveforms was performed offline and then loaded on the scanner. Next steps will include accelerated computation to achieve finer time resolution with reasonable computation times, and online implementation of ODGD waveforms for better sequence design flexibility.

Additionally, we have employed full k-space sampling for better illustration of the different formulations. Further studies may use partial k-space sampling, as it is often acquired in many applications. In addition, rapidly moving blood spins (e.g., in liver acquisitions) might also be compensated by the motion-compensated waveforms, especially for low b-values, which results in high ADC values for CODE and ODGD in/near blood vessels. Finally, the overall CG-related ADC bias patterns on Figure 4.9 is generally consistent between simulations and phantom experiments. However, there is some remaining spatially dependent ADC bias in BIPOLAR and ODGD-M_1-CG. We speculate that this remaining bias, as well as differences between the ODGD-M_1 phantom acquisition and the simulation, may be due to gradient non-linearity effects (Bammer et al., 2003; Tan et al., 2013).

4.4 Conclusions

We have proposed a novel method, termed Optimized Diffusion-weighting Gradient Waveform Design (ODGD), to design motion-compensated and CG-nulling diffusion-weighting gradient waveforms that optimize the TE for a given b-value. Theoretical results, simulations, as well as experiments in phantoms and healthy volunteers, demonstrated that ODGD motion-compensated diffusion-weighting gradient waveforms resulted in reduced TEs, increased SNR, increased motion robustness, and reduced ADC bias compared to the state-of-the-art.

5

Validation of ODGD for reduced Eddy Current induced image distortions and Peripheral Nerve Stimulation

Contents

5.1 Experimental work

In this Chapter we continue with the validation of the proposed Optimized Diffusion-weighting Gradient Waveform Design (ODGD) formulation introduced in Chapter 3 and partly validated in Chapter 4. We now focus on the validation of the proposed formulation to increase the quality of the diffusion-weighted images by reducing the artefacts introduced by the Eddy Currents (ECs) and to reduce the effects of Peripheral Nerve Stimulation (PNS) while preserving all properties already validated in the previous Chapter.

5.1.1 ODGD Simulations

The performance of the proposed ODGD-EC and ODGD-PNS method and previous waveform designs were compared by assessing the Echo Time (TE) needed to achieve a given b-value for each waveform. Specifically, gradient waveforms were compared for a broad range of b-values (20 b-values in the range of 100 - 2000 s/mm^2 separated in steps of 100 s/mm^2). Additionally, because the achievable TE also depends on the time needed by the Echo Planar Imaging (EPI) echo train to reach the center of k-space (which will itself depend on the desired spatial resolution and degree of partial Fourier acquisition), different EPI readout times to the center of k-space (7 T_{EPI} readout times in the range of 16.4 - 46.4 ms separated in steps of 5 ms) were considered for each b-value. Diffusion-weighting gradient waveforms were designed using the following hardware and time constraints: excitation radiofrequency pulse duration of T_{RF-90} = 5.5 ms; refocusing pulse duration of T_{RF-180} = 5.5 ms; maximum gradient strength of G_{Max} = 70 mT/m; waveforms without PNS-nulling were computed with maximum slew rate of SR_{Max} = 100 T/m/s (limit usually used to avoid PNS-effects) and with PNS-nulling with SR_{Max} = 150 T/m/s (hardware limit); unless otherwise stated, only one gradient axis was considered active for the computation of the b-values (note that EC-effects will depend on the diffusion-weighting direction). On the one hand, ODGD-EC waveform designs were computed with a time resolution of 0.5 ms to optimize the waveforms in moderate computation times. On the other hand, ODGD-PNS waveform designs were computed with a time resolution of 40 μs to increase resolution during ramp-up and ramp-down times when switching the diffusion-weighting gradients.

For each T_{EPI} and b-value, the following gradient waveforms for the Spin Echo (SE) Diffusion-Weighted Imaging (DWI) sequence were designed:

1. Monopolar (MONO) (Zhou et al., 1998).
2. BIPOLAR Ozaki et al. (2013).
3. Motion-Compensated (MOCO) diffusion-encoding gradient waveforms (Stoeck et al., 2016).
4. The proposed ODGD formulation for each of the motion-nulling moments (ODGD-M_n, where n = 0, 1, 2) without and with EC-nulling (ODGD-M_n-EC, where n = 0, 1, 2) and PNS-nulling (ODGD-M_n-PNS, where n = 0, 1, 2).
5. Diffusion-weighting gradient waveforms for the Twice Refocused Spin Echo (TRSE) DWI (Reese et al., 2003) sequence for the same set of parameters were also computed.

In this study, the optimization algorithm for ODGD-M_n-EC and ODGD-M_n-PNS waveforms were initialized with a constant waveform except when the Concomitant Gradient (CG)-nulling constraint was also considered in the optimization In these cases the corresponding ODGD-M_n-CG waveform was used. Figure 5.1 shows examples of some of the waveforms designed for the experiments grouped as traditional designs, ODGD waveforms without and with CG-nulling, and ODGD waveforms without and with Eddy Current (EC)-nulling and PNS-nulling.

5.1.2 Phantom Experiments

5.1.2.1 3T MRI

A 7.5L cylindrical water phantom doped with NaCl and $NiCl_2$ (Imaging, 1997) was scanned with a forty eight-channel head coil at a 3T scanner (Signa Premier, GE Healthcare, Waukesha, USA). Diffusion-weighting imaging of the diffusion phantom were acquired with a SE EPI sequence. Acquisition parameters were Repetition Time (TR) = 4 s, slice thickness = 5 mm, Field-of-View (FOV) = 24 x 24 cm, in-plane resolution = 1.88 x 1.88 mm, full k-space, six diffusion-weighting directions (±A/P, ±R/L, ±S/I), and *b*-values(averages) = [0(1), 100(2), 1000(4)] s/mm^2. The specific constraints of the optimization formulation are T_{EPI} = 11.2 ms, T_{RF-90} = 5.5 ms, T_{RF-180} = 5.5 ms, G_{Max} = 70 mT/m and SR_{Max} = 100 T/m/s. The PNS-nulling waveforms were designed with a hardware limit of the SR_{Max} = 150 T/m/s. Eight different diffusion-weighting gradient waveforms with these constraints were designed with MONO, BIPOLAR, CODE-M_n (n = 0, 1), ODGD-M_n-EC (n = 0, 1) and ODGD-M_n-PNS (n = 0, 1), respectively. Note that crusher gradients are not used around the refocusing Radio-Frequency (RF) pulse in the implementations of this phantom experiment. In order to compare Signal-to-Noise-Ratio (SNR) across different acquisitions, SNR maps were computed following (Aja-Fernández et al., 2015) through Eq. (4.1). For evaluation of SNR, the threshold mask of Figure 5.4.b) was used.

5.1.2.2 1.5T MRI

A 2L cylindrical water phantom doped with NaCl and $NiSO_4$ was scanned with a twenty-channel head coil at a 1.5T scanner (Aera 1.5T, Siemens, Erlangen, Germany). Diffusion-weighting imaging of the diffusion phantom were acquired with a spin-echo EPI sequence. Acquisition parameters were TR = 5 s, slice thickness = 2.5 mm, FOV = 24 x 24 cm, in-plane resolution = 3.75 x 3.75 mm, full k-space, six diffusion-weighting directions (±A/P, ±R/L, ±S/I), and *b*-values(averages) = [0(1), 500(1)] s/mm^2. The specific constraints of the optimization formulation are T_{EPI} = 28.5 ms, T_{RF-90} = 2.6 ms, T_{RF-180} = 11.2 ms, G_{Max} = 32 mT/m and SR_{Max} = 150 T/m/s. Further, a TRSE sequence (Reese et al., 2003) was also implemented using the same parameters but with the second radiofrequency refocusing pulse with T_{RF-180} = 17.16 ms, to better satisfy the Carr-Purcell-Meiboom-Gill (CPMG) conditions (Carr and Purcell, 1954), and G_{Max} = 28 mT/m, due to safety reasons with the duty cycle of the Magnetic Resonance (MR) scanner. Three different diffusion-weighting gradient waveforms for previous sequences and constraints were designed with MONO, TRSE DWI sequence, and ODGD-M_0-EC, respectively. In order to compare SNR across different acquisitions, SNR maps were computed as aforementioned. For evaluation of SNR, the threshold mask of Figure 5.6.b) was used.

5.2 Results

5.2.1 ODGD Simulations

5.2.1.1 Eddy Current Constraint

ODGD-M_n-EC waveforms (where n = 0, 1, 2) reduce the minimum TE of the corresponding traditional waveforms with same nth moment-order nulling and EC-nulling properties such as BIPOLAR or the TRSE DWI sequence for any given b-value and EPI readout time. ODGD with CG-nulling and EC-nulling waveforms generally also reduce the TE of the corresponding traditional BIPOLAR waveforms. Compared to ODGD-M_n and ODGD-M_n-CG, the TE of the ODGD-M_n-EC is increased. The residues achieved by the ODGD optimization in terms of b-value, CG- and EC-nulling are null (up to our numerical precision). Computation times of ODGD-EC waveforms ranged between seconds for low b-value and zeroth-order moment-nulling (ODGD-M_0-EC) to ≈30 minutes for high b-values, second-order moment-nulling, and CG-nulling (ODGD-M_2-CG-EC).

ODGD-M_n-EC waveforms (where n = 0, 1) outperform the traditional BIPOLAR waveforms and the TRSE DWI sequence as shown in Figure 5.2. Figure 5.2.a) depicts the optimal TE for a range of b-values and T_{EPI} = 26.4 ms. Figure 5.2.b) shows the TE difference between ODGD-M_1-CG-EC and ODGD-M_1-CG, and ODGD-M_1-EC without and with CG-nulling compared to BIPOLAR for the range T_{EPI} = 15 - 50 ms. Figure 5.2.c) shows the TE difference between ODGD-M_0-CG-EC and ODGD-M_0-CG, and ODGD-M_0-EC without and with CG-nulling compared to the TRSE sequence for the same range of T_{EPI}. ODGD-M_0-CG results in TE reductions between 3.1 - 18.7% compared to ODGD-M_0-CG-EC. ODGD-M_1-CG results in TE reductions between 3.8 - 14.7% compared to ODGD-M_1-CG-EC. Relative to BIPOLAR, ODGD-M_1-EC and ODGD-M_1-CG-EC result in TE reductions between 1.9 - 27.9%, and -7.0 - 11.2%, respectively. Relative to the TRSE DWI sequence, ODGD-M_0-EC and ODGD-M_0-CG-EC result in TE reductions between -6.9 - 31.3%, and -12.1 - 20.6%, respectively

5.2.1.2 Peripheral Nerve Stimulation Constraint

ODGD-M_n-PNS waveforms (where n = 0, 1, 2) reduce the minimum TE of the traditional (MONO, BIPOLAR, and MOCO) and previously proposed waveforms (ODGD-M_n) for any given b-value, EPI readout time, and nth moment-nulling order. Computation times of ODGD-PNS waveforms ranged between minutes for low b-value and zeroth-order moment-nulling (ODGD-M_0-EC) to ≈50 minutes for high b-values, and second-order moment-nulling (ODGD-M_2-PNS).

ODGD-M_n-PNS waveforms (where n = 0, 1, 2) outperform the ODGD-M_n waveforms as shown in Figure 5.3. Figure 5.3 shows the TE difference between ODGD-M_n and ODGD-M_n-PNS for the range T_{EPI} = 15 - 50 ms. Ramp-up and ramp-down times of ODGD-M_n-PNS are different to those from ODGD-M_n resulting in TE

reductions between 0 - 0.94%, 0 - 0.74%, and 0 - 0.75% for M_0, M_1, and M_2 respectively.

5.2.2 Phantom Validation

5.2.2.1 3T MRI

There is a TE decrease of 8.4% and 9.e5% of the ODGD-M_1 waveform compared to BIPOLAR and ODGD-M_1-EC (TEs of 76.5, 83.5, and 84.5, respectively), which increases the SNR of the ODGD-M_1 compared to the other two waveform designs. Mean SNR(± std) of each of the acquisitions is 225.63 (±69.21), 185.04 (±58.34), 181.61 (±57.60), and 178.58 (±57.79) for the MONO, ODGD-M_1, BIPOLAR, and the ODGD-M_1-EC waveforms.

Figure 5.4.a) shows the difference between Diffusion-Weighted (DW) images of opposite diffusion-weighting polarity (±A/P), at b-value = 1000 s/mm^2, and T_{EPI} = 11 ms for the same waveforms than before. The MONO acquisition is visually severely affected by eddy currents induced distortions showing strong mismatch between DW images of opposite polarity. On the contrary, ODGD-M_1, BIPOLAR and ODGD-M_1-EC show more homogeneous difference between DW images of opposite polarity despite their longer TE. Figure 5.4.c) shows the distribution of the difference between diffusion-weighted images acquired at three opposite DW directions (±A/P, ±R/L, ±S/I) separating between the border and phantom masks shown in Figure 5.4.b). ODGD-M_1, BIPOLAR and ODGD-M_1-EC show tighter confidence intervals and lower height at both masks proving better EC performance than MONO. Nevertheless, ODGD-M_1-EC shows similar variability to the ODGD-M_1 and BIPOLAR between opposite DW images (width of the phantom mask) and no bias despite its longer TE.

Further, there is neither visual difference nor SNR difference between ODGD-M_0 and ODGD-M_0-PNS, nor between ODGD-M_1 and ODGD-M_1-PNS as shown in Figure 5.5.

5.2.2.2 1.5T MRI

There is a TE increase of 2.1% and 14.3% of the MONO waveform compared to ODGD-M_0-EC and the TRSE DWI sequence (TEs of 93.0, 95.0, and 106.3 ms, respectively). The TE reduction of the ODGD-M_0-EC compared to the TRSE DWI sequence is of 11.9%. These TE differences provide the following SNR variations for each of the acquisitions: 43.95 (±8.86), 43.07 (±8.68), and 29.39 (±5.82) for the MONO, and ODGD-M_0-EC waveforms and the TRSE DWI sequence.

Figure 5.6.a) shows the difference between DW images of opposite diffusion-weighting polarity (±A/P), at b-value = 500 s/mm^2, and T_{EPI} = 28.5 ms for the three previous acquisitions. The MONO acquisition is visually severely affected by eddy currents induced distortions showing strong mismatch between DW images

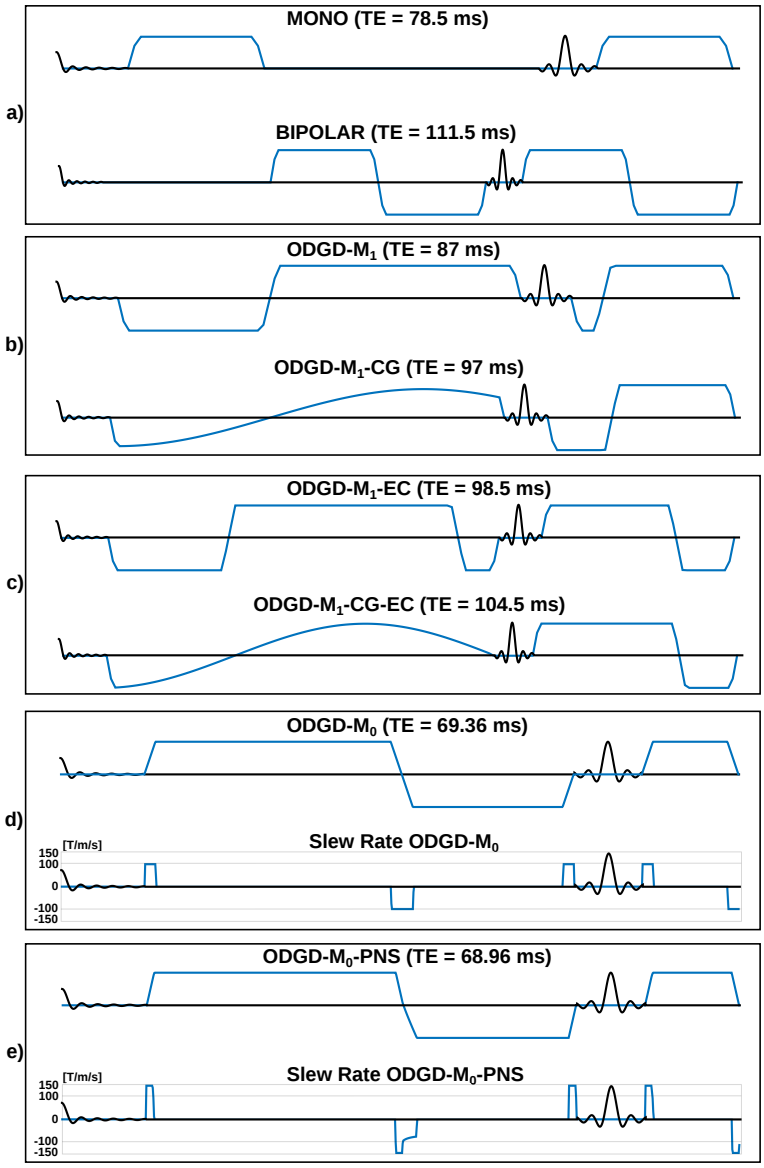

Figure 5.1: Set of diffusion-weighting gradient waveforms. Traditional waveforms (a), first-order moment-nulled (M_1) Optimized Diffusion-weighted Gradient waveform Designs (ODGD-M_1) without and with CG-nulling (Peña-Nogales et al., 2019b) (b), ODGD-M_1 waveforms with EC-nulling for a time constant of $\tau = 10$ ms without and with CG-nulling (c), ODGD-M_0 waveforms and their slew rate without and with PNS-nulling (d) and (e), respectively. (a-c) waveform designs were computed with a time resolution of 0.5 ms and (d-e) with 0.04 ms. All waveforms were designed for b-value = 1000 s/mm^2 and T_{EPI} of 24.6 ms. ODGD-M_0 and ODGD-M_0-PNS were computed with SR_{Max} of 100 T/m/s (limit used to avoid PNS-effects) and 150 T/m/s (hardware limit), respectively. Note the different slew rate of ODGD-M_0-PNS compared to ODGD-M_0.

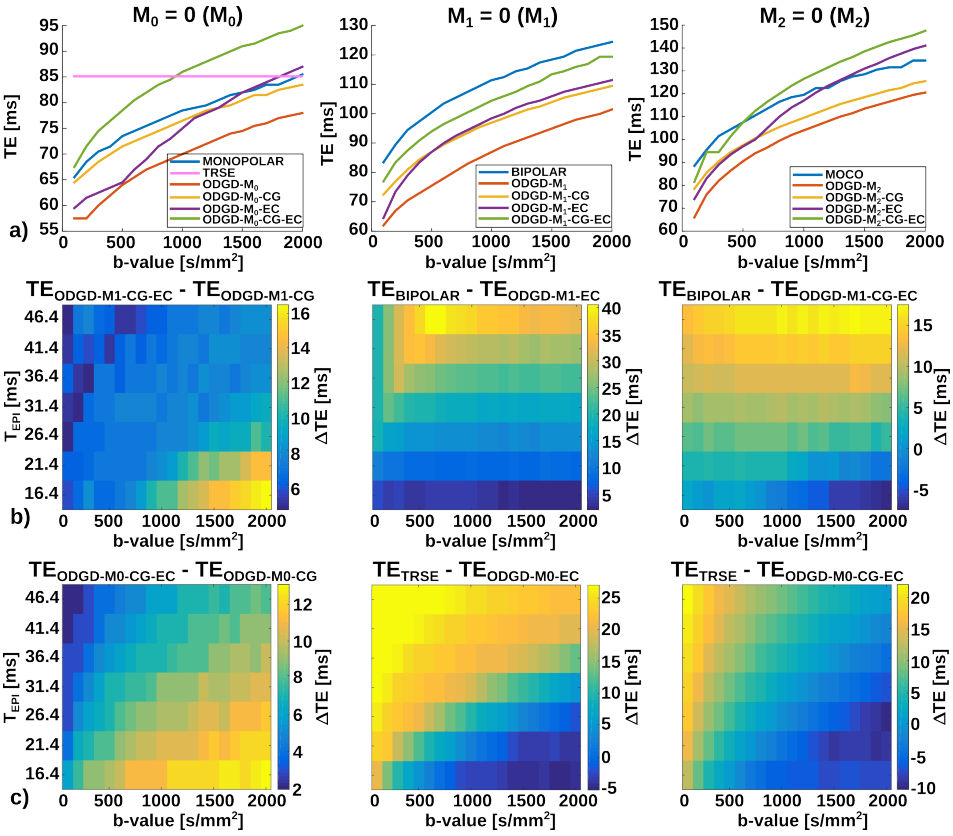

Figure 5.2: Minimum TE achieved for a range of b-values 100 - 200 s/mm^2 and T_{EPI} = 26.4 ms for ODGD-M_n, ODGD-M_n-CG, ODGD-M_n-EC, ODGD-M_n-CG-EC, the traditional waveforms (MONO, BIPOLAR, and MOCO) for M_0, M_1, and M_2 moment constraint, respectively, and the TRSE DWI sequence (a). TE reductions (ΔTE) achieved using ODGD-M_1-CG compared to ODGD-M_1-CG-EC, and ODGD-M_1-EC and ODGD-M_1-CG-EC compared to BIPOLAR for the same range of b-values and T_{EPI} in the range of 16.4 - 46.4 ms (b). TE reductions (ΔTE) achieved using ODGD-M_0-CG compared to ODGD-M_0-CG-EC, and ODGD-M_0-EC and ODGD-M_0-CG-EC compared to the TRSE DWI sequence for the same range of b-values and T_{EPI} (c). EC-nulling waveforms were designed to null time constants of τ = 10ms. ODGD waveforms with EC-nulling achieve higher minimum TE than the corresponding ODGD waveform without EC-nulling. In these cases, ΔTE is larger for higher b-values and lower T_{EPI}. Compared to BIPOLAR and the TRSE DWI sequence, ΔTE of ODGD waveforms with EC-nulling is larger for higher T_{EPI}.

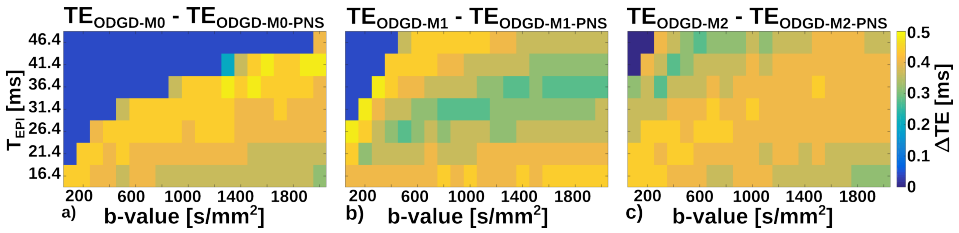

Figure 5.3: TE reductions (ΔTE) achieved using ODGD-M_n-PNS compared to ODGD-M_n for b-values 100 - 2000s/mm^2 and T_{EPI} in the range of 16.4 - 46.4 ms for M_0 (a), M_1 (b) and M_2 (c) moment constraints, respectively. There is a TE reduction between 0 - 0.94%, 0 - 0.74% and 0 - 0.75% for M_0, M_1 and M_2, respectively. TE reductions are comparable throughout b-value, T_{EPI} ranges, and nth-order moment-nulling. ODGD-M_n and ODGD-M_n-PNS were computed with SRMax of 100 T/m/s (limit found on the literature to avoid PNS-effects) and 150 T/m/s (hardware limit), respectively.

of opposite polarity. On the contrary, ODGD-M_0-EC and the TRSE DWI sequence show more homogeneous difference between DW images of opposite polarity despite their longer TE and lower SNR. Figure 5.6.c) shows the distribution of the difference between diffusion-weighted images acquired at three opposite DW directions ($\pm$A/P, $\pm$R/L, $\pm$S/I) separating between the border and phantom masks shown in Figure 5.6.b). ODGD-M_0-EC and the TRSE DWI sequence show tighter confidence intervals and lower height at both masks proving better EC performance than MONO. It is to be noted that the performance of the ODGD-M_0-EC and the TRSE DWI sequence to diminish EC image distortions is comparable albeit having the TRSE DWI sequence a 12% reduction of the maximum diffusion-weighting gradient strength (33 mT/m vs. 28 mT/m).

5.3 Discussion

We have presented the novel Optimized Diffusion-weighting Gradient Waveform Design (ODGD) formulation. The ODGD formulation allows the design of diffusion-weighting gradient waveforms to diminish Eddy Current (EC) induced image distortions and to reduce Peripheral Nerve Stimulation (PNS) while minimizing the TE of diffusion-weighted acquisition, reducing bulk motion effects and nulling Concomitant Gradient (CG) effects. The ODGD-M_n-EC, with n = 0, 1, 2, generally reduced the TE of state-of-the-art diffusion-weighting gradient waveforms and sequences with similar EC-nulling properties (i.e,. BIPOLAR waveforms and TRSE DWI sequence). This TE reduction tends to be higher for higher k-space resolutions (i.e., longer T_{EPI}) and enables an increase of the SNR in Diffusion-Weighted Magnetic Resonance Imaging (DW-MRI) by avoiding T_2-related signal losses. Nevertheless, TE increases and SNR decreases when compared to the traditional MONO non EC-nulling waveform. On the other hand, the ODGD-M_n-PNS waveforms achieve similar TE reduction for any b-value - T_{EPI} combinations, with no SNR increase.

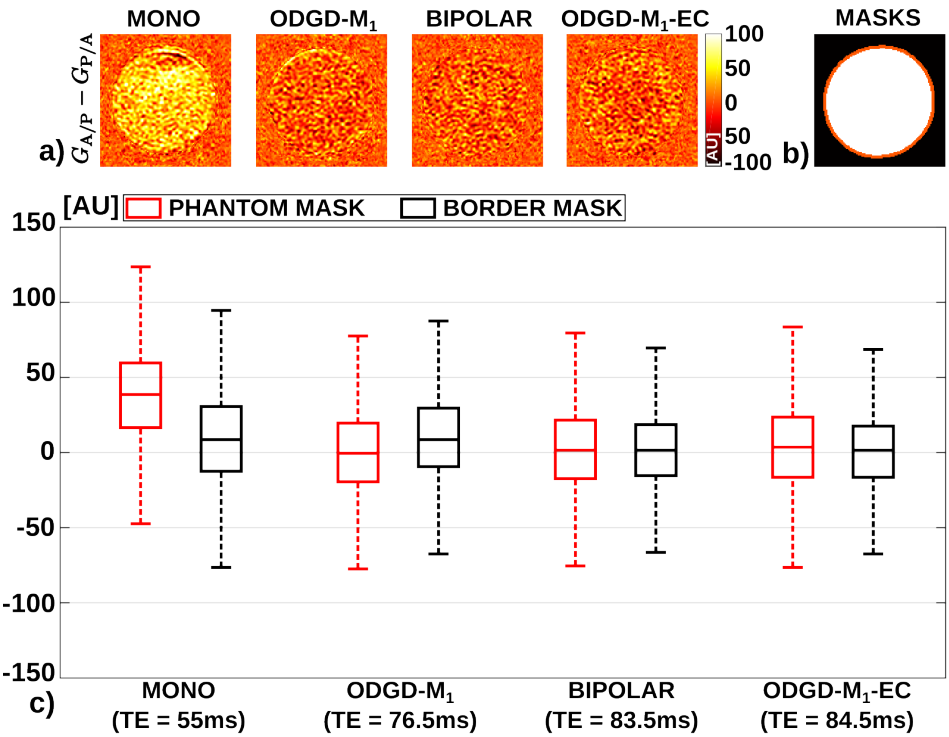

Figure 5.4: Difference between diffusion-weighted images acquired with opposite diffusion-weighting polarity (±A/P), b-value = 1000 s/mm^2, and T_{EPI} = 11 ms with waveforms MONO, ODGD-M_1, BIPOLAR, and ODGD-M_1-EC of the phantom experiment at 3T (a). Masks for ROI analysis (b). Distribution of the difference between diffusion-weighted images acquired with the three opposite diffusion-weighting directions (c). Red and black boxes show the distribution of the phantom and border masks, respectively. MONO is severely affected by eddy currents induced distortions showing strong mismatch between opposite DW images (higher height and wide confidence interval). At the phantom's border, ODGD-M_1 is slightly affected by EC induced distortions. ODGD-M_1, BIPOLAR, and ODGD-M_1-EC show more homogeneous difference between opposite DW images than MONO. Compared to ODGD-M_1, BIPOLAR and ODGD-M_1-EC show similar variability between opposite DW images despite their longer TE.

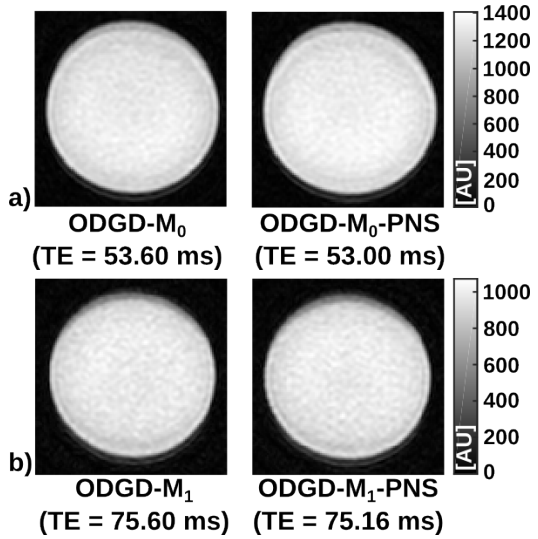

Figure 5.5: Diffusion-weighted images acquired with ODGD-M_n, where n = 0, 1, without and with PNS-nulling. Zeroth-order motion-compensated waveforms (a). First-order motion-compensated waveforms (b). There is no visual difference between ODGD waveforms without and with PNS-nulling.

Diffusion-weighting gradient waveforms with EC-nulling have promising applications in DWI by improving DW image quality and improved quantification of the parametric maps. Further, PNS-nulling waveforms may have important applications in Magnetic Resonance Imaging (MRI) of the fetus where reduced nerve stimulation is essential. The potential of both EC- and PNS-nulling waveforms is of added importance in brand-new high gradient MRI scanners (i.e., Connectome MRI scanners) which are able to drive ultra- high-gradient strengths and one-of-a-kind high-slew rates (Jones et al., 2018).

This work has several limitations. The ODGD waveforms with EC-nulling were designed for a medium EC time constant on two different scanners without previously measuring the most significant EC time constants of the scanner. Thus, tuning of the time EC constant on the ODGD formulation might lead to further image distortion reduction reducing the border artefacts of Figures 5.4 and 5.6. The ODGD waveforms with PNS-nulling were feasibly implemented in the scanner. However, nerve stimulation effects only appear in in-vivo acquisitions, thus their PNS-nulling properties could not be tested. As a result, the proposed ODGD formulation needs to be further validated in brain, liver, and heart in-vivo studies in volunteers and in patients. Additionally, an extension of the formulation to optimize the imaging gradients in addition to the diffusion gradients (Schulte and Noeske, 2015), and application to other DWI sequences is also desirable.

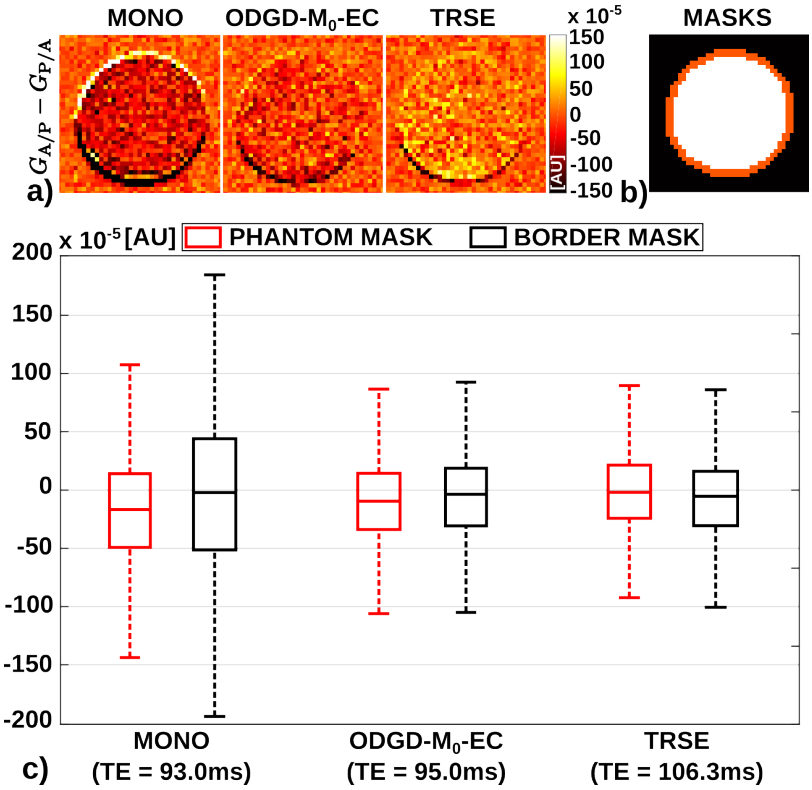

Figure 5.6: Difference between diffusion-weighted images acquired with opposite diffusion-weighting polarity (±A/P), b-value = 500 s/mm^2, and T_{EPI} = 28.5 ms with waveforms MONO, ODGD-M_0-EC, and the TRSE DWI sequence of the phantom experiment at 1.5T(a). Masks for ROI analysis (b). Distribution of the difference between diffusion-weighted images acquired with the three opposite diffusion-weighting directions (c). Red and black boxes show the distribution of the phantom and border masks, respectively. MONO is severely affected by eddy currents induced distortions showing strong mismatch between opposite DW images in both masks (higher height and wide confidence interval). ODGD-M_0-EC and the TRSE DWI sequence show comparable performance to reduce the EC induced distortions showing more homogeneous difference between opposite DW images and tighter confidence intervals at both the border and the phantom mask.

5.4 Conclusion

We have proposed the novel Optimized Diffusion-weighting Gradient Waveform Design (ODGD) method to design motion-compensated, CG-, EC- and/or PNS-nulled diffusion-weighting gradient waveforms that optimize the TE for a given b-value. Theoretical results and phantom experiments on scanners from two different vendors demonstrated that the ODGD formulation has the potential to improve image quality compared to standard DW-MRI methods.

Part III

Contribution II:

Diffusion-Weighting b-value Optimization

6

b-Value Optimization: Motivation and Theory

Contents

6.1 Introduction

The standard procedure to measure diffusion-related parametric maps is by applying a monoexponential model to the diffusion-weighted signal decay as previously indicated in Subsection 2.2.3. Such model provides a quantitative diffusion value, known as Apparent Diffusion Coefficient (ADC), which can be used to characterize the tissue (Koh and Thoeny, 2010; Padhani et al., 2009a; Taouli et al., 2016). However, this value jointly describes the diffusion originating from multiple compartments, which hinders its interpretation and determines its lack of physical significance (Le Bihan et al., 1991). This is of particular interest in abdominal organs such as the liver due to their comprehensive vascular network (Dijkstra et al., 2012; Yamada et al., 1999). To overcome this limitation, the Intravoxel Incoherent Motion (IVIM) biexponential diffusion-weighted signal model was developed by Le Bihan et al. (1988). This signal model, also introduced in Subsection 2.2.3, separates the contribution of the Diffusion-Weighted (DW) signal into two terms. The first one corresponds to the signal of the diffusing spins, and the second one corresponds to the signal of the spins undergoing translational displacements due to

the microcirculation or pseudodiffusion of the blood flow in the capillary network. The latter effect translates into a fast decrease of the diffusion-weighted signal at low b-values. This implies that for high b-values the signal from the capillary network diminishes and only the signal from diffusing spins remains.

In the past decades, it has been proven how the estimation of the ADC and of the IVIM parametric maps such as the pseudodiffusion and the diffusion maps can aid tissue characterization. For example, multiple authors have showed how the ADC decreases in liver metastasis reflecting the cellularity of the tumour (Koh and Thoeny, 2010; Padhani et al., 2009a), Luciani et al. (2008) showed that pseudodiffusion is lower in cirrhotic livers than in healthy livers, and Chow et al. (2012) indicated that IVIM analysis may be a valuable tool in liver fibrosis detection and characterization. However, the estimation of the ADC and of the IVIM parametric maps is affected by several confounding factors (i.e., bias, lack of repeatability, and/or lack of reproducibility) that hinder their establishment as quantitative imaging biomarkers. The influence of all these factors, together with the lack of standardization of acquisition parameters, may contribute to the variability of the diffusion values found in the literature (Taouli and Koh, 2009). Moreover, these confounding factors are particularly severe in liver Diffusion-Weighted Imaging (DWI), due to several additional imaging challenges including respiratory and cardiac motion (Taouli and Koh, 2009). For example, several studies (Bruegel et al., 2008b; Gourtsoyianni et al., 2008; Kim et al., 1999; Namimoto et al., 1997; Taouli et al., 2003) show that the ADC varies between 0.69 - 1.83 $\times$ 10^{-3} mm^2/s in normal liver, between 0.97 - 1.38 $\times$ 10^{-3} mm^2/s in hepatocellular carcinomas, and between 2.55 - 3.63 $\times$ 10^{-3} mm^2/s in cysts (see Table 2.2 for more details). Quantitative diffusion Magnetic Resonance Imaging (MRI) in the liver has important potential applications in research and in the clinic (Colagrande et al., 2010; Koh and Thoeny, 2010). However, in order to enable the widespread dissemination of quantitative diffusion MRI for the measurement of quantitative imaging diffusion biomarkers, there is an unmet need to improve and characterize its accuracy (lack of bias), precision (low variance), reproducibility (low variability across sites and platforms), and robustness (insensitivity to platform scan parameters and estimation algorithm) as previously indicated in Section 1.1.

Diffusion-related parametric map estimation is also affected by aspects such as DW image quality, Signal-to-Noise-Ratio (SNR), and the weighting of the DWI sequence. Multiple approaches have been proposed to increase DW image quality (Le Bihan et al., 2006; Norris, 2001; Peña-Nogales et al., 2019b), and even though low SNR can bias the estimations (Koay et al., 2009), this bias can be reduced if using the appropriate estimator as shown by Sijbers et al. (1998). On the other hand, one of the best approaches to increase the precision of the diffusion-related parametric maps is through the application of the appropriate diffusion weighting, which is generally defined as the set of b-values that is acquired. The b-value definition was initially established by Stejskal and Tanner back in 1965 (Stejskal and Tanner, 1965). Withal, the optimal set of b-values for both the monoexponential and the IVIM signal models remains unclear (Guiu and Cercueil, 2011; Koh and Collins, 2007), in spite of the fact that it has substantial effects on the estimated diffusion-related parametric maps as shown in Figure 6.1 for the ADC. The optimization of

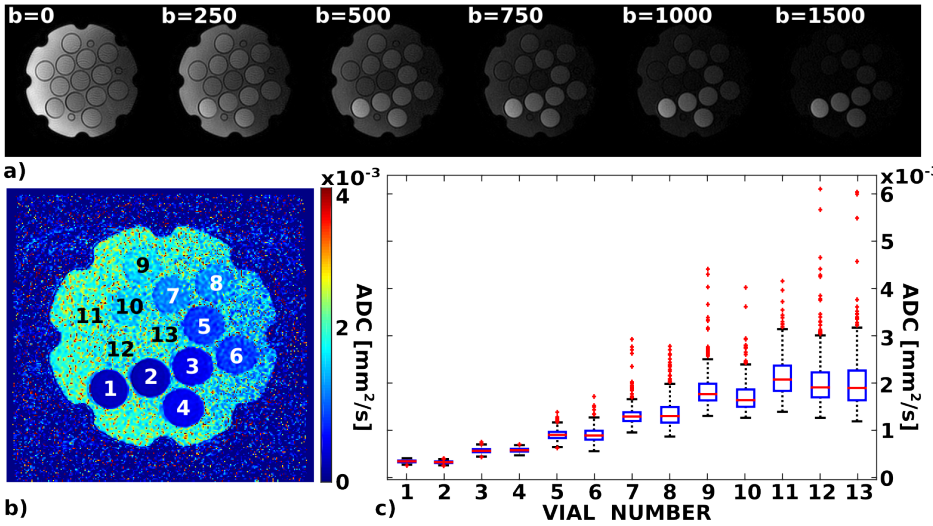

Figure 6.1: Estimated Apparent Diffusion Coefficient (ADC) map and its variance of the quantitative diffusion phantom (Imaging, 1997). (a) Diffusion-weighted images of the 13 vials quantitative diffusion phantom acquired at b-values of 0, 250, 500, 750, 1000, and 1500 s/mm^2. (b) Corresponding ADC map. Distribution of the ADC values of a Region of Interest (ROI) set on each vial (c). For this specific set of b-values, vials with low ADC (vials 1 to 4) have higher noise performance (i.e., ADC maps have low variance) than vials with higher ADC (vials 9 to 13).

the set of b-values has been an important question since the early stages of DWI, when Xing et al. (1997) proposed a propagation of error formulation to optimize the set of b-values for ADC mapping. Subsequently, other authors have also tackled this optimization problem, such as (Jones et al., 1999; Kingsley and Monahan, 2004), and (Zhang et al., 2012) for IVIM DWI. Yet, all of these previous works considered the signal to be affected by Gaussian distributed noise by assuming a high SNR. This way, classical estimation tools could directly be applied to the problem formulation. However, in MRI, other statistical distributions are usually considered for noise, specially in low SNR scenarios, as in body DWI. As indicated in Section 2.5.1 the most accepted model is to consider that MRI images are corrupted by Rician distributed noise, which is a valid assumption for single-coil acquisitions and some multi-coil parallel imaging methods such as Sensitivity Encoding (SENSE) (Aja-Fernández and Vegas-Sánchez-Ferrero, 2016). Saritas et al. (2011) applied precisely Rician noise statistics to the diffusion estimates to optimize the b-values for a two sample measurement. Albeit using a more accurate noise formulation, their proposal lacked of generalization since they assumed that the ADC is estimated from only a two-point measurement scheme of nth-averaged DW images, which is not necessarily the case in the clinical routine. Further, their optimized set of b-values was not empirically validated.

Monte-Carlo simulations have also been employed to obtain the optimized set of b-values in body DWI, as proposed by Jambor et al. (2014); Lemke et al. (2011);

Merisaari and Jambor (2015); Senegas et al. (2012). However, this technique is markedly computationally expensive, which limits its utility. Finally, an alternative approach to optimize the set of b-values is through the Cramér-Rao Lower Bound (CRLB), which is described in detail next in Section 6.2. The CRLB provides a theoretical framework to obtain the lower bound on the variance of any unbiased estimator. Therefore, by minimizing the CRLB, which depends on the chosen set of b-values, we can obtain the set that optimizes the noise performance of the estimated maps (i.e., maximize the precision and minimize the variance). The CRLB approach has been previously used for the monoexponential model in the brain (Brihuega-Moreno et al., 2003), and for the IVIM model in the liver (Alberich-Bayarri et al., 2014; Jalnefjord et al., 2019; Leporq et al., 2015). Nevertheless, in these approaches the authors again considered DW images to be affected by Gaussian distributed noise. In addition, in (Alexander, 2008; Poot et al., 2010) the authors used the CRLB to optimize the gradient settings for diffusion kurtosis imaging and for microstructure imaging in the brain under Rician distributed noise. However, due to the high dimensionality of their optimization problems, optimizations were performed through a stochastic method, which is only guaranteed to find an approximate optimal combination of gradient settings. Further, their optimizations were not validated through empirical experiments.

Therefore, in this part of the Thesis dissertation we derive the Cramér-Rao Lower Bound (CRLB) of both the monoexponential and the IVIM isotropic diffusion signal models used in liver DWI under the assumption that magnitude images are affected by Rician distributed noise. In addition, we propose a formulation to obtain, for a given scenario (target diffusion values, SNR and total number of b-values to be employed), optimized sets of b-values that maximize the noise performance of the estimated diffusion-related parametric maps (i.e., maximize the precision and minimize the variance). The theoretical foundation of the CRLB is described in this chapter, and is completed in the following Chapters 7 and 8 to derive the CRLB of the monoexponential and the IVIM signal models, respectively. In Chapter 7 the proposed formulation for the monoexponential signal model is experimentally validated using synthetic data, phantoms, and in-vivo liver DWI acquisitions. Further, the CRLB-based optimized set of b-values for both signal models for in-vivo liver DWI are compared with other sets of b-values proposed in the literature in their corresponding chapters.

6.2 Cramér-Rao Lower Bound Theory

Suppose that we have a noise free quantity, S, which depends on the parameters $\boldsymbol{\theta}$. If we have a set of noisy observations, $\tilde{S} = \{\tilde{S}_1, \ldots, \tilde{S}_K\}$ with a probability density function, $p(\tilde{S}|\boldsymbol{\theta})$, and a log-likelihood, $\log p(\tilde{S}|\boldsymbol{\theta})$. Then, the Fisher Information Matrix (FIM), $\boldsymbol{I}$, of these set of measurements is given by Van den Bos (2007) as:

$$\boldsymbol{I}(\boldsymbol{\theta}_0) = \mathbb{E}\left\{ \left(\frac{\partial \log p(\tilde{S}|\theta)}{\partial \boldsymbol{\theta}} \right)^T \left(\frac{\partial \log p(\tilde{S}|\theta)}{\partial \boldsymbol{\theta}} \right) \Bigg|_{\boldsymbol{\theta}=\boldsymbol{\theta}_0} \right\}, \tag{6.1}$$

where $\boldsymbol{\theta}_0$ is the true value of $\boldsymbol{\theta}$. Then, the minimum variance, i.e., highest precision, with which a certain parameter can be estimated using an unbiased estimator is given by the CRLB inequality:

$$\mathrm{cov}(\hat{\boldsymbol{\theta}}) \geq \boldsymbol{I}^{-1}(\boldsymbol{\theta}_0) \tag{6.2}$$

where $\mathrm{cov}(\hat{\boldsymbol{\theta}})$ is the covariance matrix of the estimator $\hat{\boldsymbol{\theta}}$. Therefore, considering a Diffusion-Weighted Magnetic Resonance Imaging (DW-MRI) sequence with a set of K b-values, and assuming the simpler case where the noise is equally distributed along every diffusion-weighted image ($\sigma = \sigma_k$), an element of the FIM is given by

$$\begin{aligned}\boldsymbol{I}(\boldsymbol{\theta}) &= \mathbb{E}\left\{\left(\sum_{k=1}^{K}\frac{\partial \log p(\tilde{S}|\theta)}{\partial S_k}\frac{\partial S_k}{\partial \boldsymbol{\theta}}\right)^T\left(\sum_{k=1}^{K}\frac{\partial \log p(\tilde{S}|\theta)}{\partial S_k}\frac{\partial S_k}{\partial \boldsymbol{\theta}}\right)\right\} \\ &= \sum_{k=1}^{K}\left(\frac{\partial S_k}{\partial \boldsymbol{\theta}}\right)^T\left(\frac{\partial S_k}{\partial \boldsymbol{\theta}}\right)\mathcal{I}_n(S_k,\sigma),\end{aligned} \tag{6.3}$$

where S_k is the diffusion-weighted signal model, $\mathcal{I}_n(S_k,\sigma)$ is the Fisher Information of a statistical variable, and n depends on the noise distribution.

Particularly, $\mathcal{I}_n(S_k,\sigma)$ for the Gaussian noise distribution is

$$\mathcal{I}_{\mathrm{Gauss}}(S_k,\sigma) = \sigma^{-2} \tag{6.4}$$

and for the Rician noise distribution is, according to Karlsen et al. (1999):

$$\mathcal{I}_{\mathrm{Rice}}(S_k,\sigma) = \int_{\hat{S}=0}^{\infty}\left(\frac{\hat{S}I_1\left(\frac{S_k\hat{S}}{\sigma^2}\right)}{\sigma^2 I_0\left(\frac{S_k\hat{S}}{\sigma^2}\right)} - \frac{S_k}{\sigma^2}\right)^2 \times \frac{\hat{S}e^{\left(-\frac{S_k^2+\hat{S}^2}{2\sigma^2}\right)}I_0\left(\frac{S_k\hat{S}}{\sigma^2}\right)}{\sigma^2}d\hat{S} \tag{6.5}$$

where I_1 and I_0 are the modified Bessel functions of the first kind of order 1 and 0 respectively.

7

Determination of optimized set of b-values for Apparent Diffusion Coefficient mapping in liver Diffusion-Weighted MRI

Contents

7.1 Theory

In the monoexponential Diffusion-Weighted Imaging (DWI) isotropic model, as shown in Eq. (2.27) of Section 2.2.3, the measured signal is described (Stejskal and Tanner, 1965) as:

$$S(b) = S_0 e^{-b\ \mathrm{ADC}}, \tag{7.1}$$

where b is the b-value, S_0 is the signal intensity when no diffusion-weighting gradient is applied, and ADC is the Apparent Diffusion Coefficient. Generally, the estimation of the Apparent Diffusion Coefficient (ADC) is performed by voxelwise fitting the previous model to a set of weighted measurements, $S(b_\mathrm{k})$ where $k \in [1,\ldots,K]$. Therefore, we seek to maximize the precision and noise performance of ADC estimations through the selection of the optimized set of b-values via the Cramér-Rao Lower Bound (CRLB) theory introduced in Chapter 6 under a Rician noise assumption (see Section 2.5.1 for details). This formulation is presented below followed by the methods used to optimize the set of b-values.

7.1.1 Cramér-Rao Lower Bound of the monoexponential DWI signal model

The Cramér-Rao Lower Bound (CRLB) provides a lower bound on the variance of any unbiased estimator as indicated in Section 6.2. Particularly, the Maximum Likelihood (ML) estimator is asymptotically unbiased and efficient under Rician distributed noise (Sijbers et al., 1998). Therefore, the variance of its estimates will reach the CRLB asymptotically (i.e., for a large number of samples).

In Diffusion-Weighted Magnetic Resonance Imaging (DW-MRI), given the noise free model in Eq. (7.1) with the set of parameters $\boldsymbol{\theta} = \{S_0, \mathrm{ADC}\}$ and any noise distribution, the Fisher Information Matrix (FIM) (Van den Bos, 2007) is:

$$\boldsymbol{I}(\boldsymbol{\theta}) = \begin{bmatrix} \sum_{k=1}^{K} e^{-2\cdot b_k \cdot \mathrm{ADC}}\ \mathcal{I}_n(S(b_k),\sigma) & -\sum_{k=1}^{K} S_0 b_k e^{-2\cdot b_k \cdot \mathrm{ADC}}\ \mathcal{I}_n(S(b_k),\sigma) \\ -\sum_{k=1}^{K} S_0 b_k e^{-2\cdot b_k \cdot \mathrm{ADC}}\ \mathcal{I}_n(S(b_k),\sigma) & \sum_{k=1}^{K} S_0^2 b_k^2 e^{-2\cdot b_k \cdot \mathrm{ADC}}\ \mathcal{I}_n(S(b_k),\sigma) \end{bmatrix}, \tag{7.2}$$

where K is the number of b-values in the set, σ the covariance, and $\mathcal{I}_n()$ depends on the noise distribution (i.e., Gaussian (Karlsen et al., 1999) or Rician (Karlsen et al., 1999; Poot et al., 2010)).

Therefore, the CRLB of the DW-MRI monoexponential model is given by inverting Eq. (7.2) as shown in the CRLB inequality (Section 6.2), (Karlsen et al.,

1999):

$$\mathrm{cov}(\hat{\boldsymbol{\theta}}) \geq \boldsymbol{I}^{-1}(\boldsymbol{\theta}), \tag{7.3}$$

where $\mathrm{cov}(\hat{\boldsymbol{\theta}})$ is the covariance matrix of the estimator $\hat{\boldsymbol{\theta}}$. As shown in the previous equations, the CRLB will depend on the set of b-values, the total number of b-values (K) of the set, the actual ADC, S_0, σ and the noise distribution as shown in Chapter 6.

7.2 Experimental work

7.2.1 Determination of the optimized set of b-values

The computation of the optimized set of b-values for a given set of parameters, $\boldsymbol{\theta} = \{S_0, \mathrm{ADC}\}$, is achieved by minimizing the elements of the right hand side of the CRLB inequality (Eq. (7.3)).

In the inverse of the FIM (Eq. (7.2)), the elements of the diagonal correspond to the lower bound of any unbiased estimator for a set of b-values and a unique set of parameters $\boldsymbol{\theta}$. Top left element ($\boldsymbol{I}^{-1}(\boldsymbol{b},\boldsymbol{\theta})_{11}$) corresponds to the CRLB of the S_0 ($\mathrm{CRLB}_{\mathrm{S_0}}$), and the bottom right element ($\boldsymbol{I}^{-1}(\boldsymbol{b},\boldsymbol{\theta})_{22}$) corresponds to the CRLB of the ADC ($\mathrm{CRLB}_{\mathrm{ADC}}$). On the other hand, the off-diagonal elements correspond to the covariance between both parameters (Karlsen et al., 1999). In order to obtain the optimized set of b-values that maximize the noise performance of the ADC maps (i.e., maximize the precision and minimize the variance), in this work, we only consider $\mathrm{CRLB}_{\mathrm{ADC}}$ in the minimization process. Thus, the optimized set of b-values is obtained through the minimization of the following objective function:

$$\hat{\boldsymbol{b}} = \arg\min_{\boldsymbol{b}} \boldsymbol{I}^{-1}(\boldsymbol{b},\boldsymbol{\theta})_{22} = \arg\min_{\boldsymbol{b}} \mathrm{CRLB}_{\mathrm{ADC}}(\boldsymbol{b}) \tag{7.4}$$

In general, and depending on the total number of desired b-values (K), this minimization process can be computationally expensive, or even infeasible in practice. In order to overcome this challenge, we propose two alternative methods to perform the minimization by selecting the optimal b-values from a large pool of N candidates:

Greedy algorithm: Starting from an initial set of b-values composed only of one b-value (b = 0 s/mm^2), the algorithm iteratively adds to the set the b-value that achieves minimum $\mathrm{CRLB}_{\mathrm{ADC}}$ among the pool of N candidates. The algorithm iterates until a set of K b-values is completed. This approach was previously implemented by Lemke et al. (2011).

Two b-value search: In this case, the optimized set is restricted to be composed of only two b-values. The first of them is fixed to be b= 0 s/mm^2 to have measurements with maximum Signal-to-Noise-Ratio (SNR) (it is to be noted that for some liver DWI applications the lowest b-value might be b= 100 s/mm^2 to avoid too much contamination from Intravoxel Incoherent Motion (IVIM) (Taouli

et al., 2016)), whereas the second one is chosen among the pool of N-1 candidates (notice that the previously chosen b-value is removed from the pool of candidates). Then an exhaustive search is performed to find the optimized set of K b-values, where k_1 b-values will be equal to 0 s/mm^2 and k_2 will be different, but always the same b-value ($k_1 + k_2 = K$). The [k_1, k_2] combination of the pair of b-values that achieve minimum $\mathrm{CRLB}_{\mathrm{ADC}}$ is considered optimal. Hereinafter, the sets of b-values obtained using these two CRLB-based analysis are called CRLB-based b-value sets.

Table 7.1, Table 7.2, and Table 7.3 show the ADC, SNR of the S_0 image, and b-value pool of candidates used to obtain the CRLB-based b-value sets under both methodologies assuming Rician and Gaussian distributed noise. For the greedy algorithm, the CRLB-based b-value sets obtained from Table 7.1 were composed of $K = 13$ b-values, and the sets of Table 7.2 and Table 7.3 were composed of $K = 16$ b-values. For the two b-value search algorithm, the CRLB-based b-value sets were obtained for all K in the range of 2 to 16. For the sake of clarity, these experiments to obtain optimized CRLB-based b-value sets are described in Table 7.4.

In addition, to study the convergence properties of the two b-value search algorithm to provide fast computation of the CRLB-based b-value sets, it was applied to ADC values of 2.1, 1.2, and 0.9 mm^2/s, and SNR values of 100, 50, 20, and 10 assuming both Gaussian and Rician noise distributions. Two b-value pool of candidates were composed of N = 701 and 2001 b-values uniformly distributed between 0 and 700, and 0 and 2000 s/mm^2, respectively. All optimized sets were computed for K in the range of 2 to 60.

7.2.2 Experimental data

In order to validate the proposed methods (i.e., greedy algorithm and two b-value search), we need to study whether these two methods are able to obtain sets of b-values that effectively yield the lowest possible variance on the estimated ADC maps. To that end, we compare the CRLB-based optimized b-value sets obtained with the previous two methods to those obtained experimentally from synthetic data, phantoms, and in-vivo liver DWI experiments (these b-value sets obtained experimentally are later described in Section 7.2.3). Therefore, two phantom acquisitions and an in-vivo liver acquisition were carried out as described in the following subsections. Further, in order to have realistic synthetic data, and to facilitate the assessment of the CRLB-based analysis, synthetic DWI images were generated from the estimated features of Regions of Interest (ROIs) drawn on both phantom acquisitions as subsequently described in the Experimental validation Subsection 7.2.3.

7.2.2.1 Quantitative diffusion phantom

A High Precision Devices' (HPD) Quantitative Diffusion Phantom (Bolder, CO, USA) with 13 vials of aqueous solutions doped with various concentrations of

Table 7.1: Characterization of each of the 13 vials of the quantitative diffusion phantom. Mean ground truth ADC (± standard deviation), mean T_2 (± standard deviation), and mean SNR (± standard deviation) of the S_0 image. Pool of b-values is composed of N = 41 b-values uniformly distributed between 0 and 2000 s/mm^2. Ground truth ADC was computed from all DW images and b-values in the range 0 – 1000 s/mm^2.

	VIALS													Max. b-value
	1	2	3	4	5	6	7	8	9	10	11	12	13	pool of candidates
ADC	0.32	0.30	0.54	0.54	0.87	0.88	1.22	1.26	1.69	1.62	2.10	2.08	2.09	-
[$\times 10^{-3}$ mm^2/s]	± 0.02	± 0.02	± 0.04	± 0.02	± 0.05	± 0.04	± 0.04	± 0.04	± 0.03	± 0.02	± 0.02	± 0.04	± 0.06	
T_2 [ms]	307.3	303.2	400.9	395.5	428.0	433.7	468.1	467.4	555.9	582.5	913.3	909.1	855.5	-
	± 4.3	± 6.0	± 14.1	± 8.5	± 18.7	± 21.7	± 21.9	± 32.7	± 27.5	± 23.7	± 58.3	± 52.2	± 75.8	
SNR	52.6	42.3	34.4	48.	29.0	22.8	39.5	25.23	53.19	50.6	57.8	46.5	39.7	2000 s/mm^2
	± 12.8	± 9.7	± 8.3	± 13.1	± 7.1	± 6.6	± 8.6	± 6.7	± 12.1	± 11.9	± 12.2	± 10.4	± 9.6	(TE = 111 ms)

Table 7.2: Characterization of each of the 10 vials of the acetone phantom. Mean ground truth ADC (± standard deviation), mean T_2 (± standard deviation), and five mean SNR (± standard deviation) of the S_0 image. Pool of b-values for each SNR row is composed of N = 15, 21, 27, 31, and 41 b-values uniformly distributed between 0 and 700 s/mm^2, 0 and 1000 s/mm^2, 0 and 1300 s/mm^2, 0 and 1500 s/mm^2, and 0 and 2000 s/mm^2, respectively. Ground truth ADC was computed from all DW images and b-values of the DWI acquisition with TE = 75.9 ms and maximum b-value of 1000 s/mm^2.

	VIALS										Max. b-value
	1	2	3	4	5	6	7	8	9	10	pool of candidates
ADC [$\times 10^{-3}$ mm^2/s]	1.05 ± 0.04	1.43 ± 0.02	1.74 ± 0.03	1.94 ± 0.02	2.34 ± 0.04	2.39 ± 0.07	2.03 ± 0.02	1.70 ± 0.02	1.36 ± 0.01	0.97 ± 0.05	-
T_2 [ms]	86.2 ± 1.2	87.5 ± 1.0	88.2 ± 1.3	85.9 ± 0.9	82.6 ± 0.9	36.0 ± 0.7	37.2 ± 0.4	37.5 ± 0.5	37.7 ± 0.5	36.4 ± 0.3	-
SNR	118.1 ± 27.0	110.9 ± 17.2	124.0 ± 26.6	118.0 ± 23.8	133.9 ± 27.3	66.5 ± 14.0	52.9 ± 11.0	45.8 ± 9.7	46.3 ± 9.0	48.0 ± 10.0	700 s/mm^2 (TE = 70 ms)
SNR	121.6 ± 29.6	109.4 ± 26.4	116.6 ± 22.1	122.0 ± 23.0	134.3 ± 30.2	52.3 ± 9.4	45.3 ± 9.5	39.9 ± 8.5	39.6 ± 7.1	41.7 ± 9.4	1000 s/mm^2 (TE = 75.9 ms)
SNR	109.4 ± 27.2	102.4 ± 20.0	107.7 ± 24.4	115.6 ± 28.0	129.2 ± 30.2	47.2 ± 10.4	40.1 ± 8.3	34.8 ± 7.7	34.8 ± 6.4	34.5 ± 7.6	1300 s/mm^2 (TE = 80.8 ms)
SNR	109.4 ± 30.0	101.4 ± 20.0	102.8 ± 19.1	108.8 ± 20.2	127.6 ± 30.2	44.2 ± 9.3	38.6 ± 8.3	34.5 ± 7.3	34.5 ± 6.9	31.8 ± 6.9	1500 s/mm^2 (TE = 83.6 ms)
SNR	99.9 ± 26.7	92.4 ± 20.4	93.1 ± 15.6	109.2 ± 24.9	114.1 ± 26.4	34.2 ± 8.4	30.8 ± 6.2	27.0 ± 6.2	37.3 ± 5.1	27.0 ± 4.7	2000 s/mm^2 (TE = 89.7 ms)

Table 7.3: Characterization of all Regions of Interest (ROIs) of the liver DWI experiment. Mean ground truth ADC (± standard deviation), and mean SNR (± standard deviation) of the S_0 image. Pool of b-values is composed of 11 b-values uniformly distributed between 0 and 1000 s/mm^2. Ground truth ADC was computed from all DW images and b-values of the liver DWI acquisition.

					30 mm^2 ROIs						Max. b-value
	1	2	3	4	5	6	7	8	9	10	pool of candidates
ADC [$\times 10^{-3}$ mm^2/s]	0.99 ± 0.05	1.60 ± 1.51	1.15 ± 0.19	1.09 ± 0.09	1.32 ± 0.30	1.19 ± 0.18	1.21 ± 0.35	1.26 ± 0.19	1.21 ± 0.32	1.17 ± 0.24	-
SNR	9.4 ± 1.1	11.8 ± 2.2	10.7 ± 2.2	10.0 ± 2.0	6.9 ± 0.8	9.4 ± 1.6	9.4 ± 1.9	10.7 ± 2.5	6.5 ± 1.9	10.9 ± 1.2	1000 s/mm^2 (TE = 65.66 ms)
	30 mm^2 ROIs										Max. b-value
	11	12	13	14	15	16	17	18	19	20	pool of candidates
ADC [$\times 10^{-3}$ mm^2/s]	1.08 ± 0.12	1.14 ± 0.11	1.21 ± 0.19	1.22 ± 0.11	1.59 ± 0.78	1.20 ± 0.18	1.38 ± 0.70	1.73 ± 0.73	1.03 ± 0.07	1.03 ± 0.03	-
SNR	9.6 ± 1.4	5.2 ± 1.0	9.2 ± 1.4	5.9 ± 1.1	7.5 ± 0.5	9.6 ± 1.7	6.2 ± 0.9	4.8 ± 1.0	9.6 ± 1.3	8.9 ± 0.8	1000 s/mm^2 (TE = 65.66 ms)
	30 mm^2 ROIs										Max. b-value
	21	22	23	24	25	26	27	28	29	30	pool of candidates
ADC [$\times 10^{-3}$ mm^2/s]	1.08 ± 0.12	1.22 ± 0.24	1.17 ± 0.21	1.19 ± 0.05	1.39 ± 0.37	1.43 ± 0.38	1.24 ± 0.25	1.07 ± 0.05	1.04 ± 0.06	1.18 ± 0.24	-
SNR	7.8 ± 0.9	8.8 ± 1.8	6.3 ± 0.7	7.4 ± 1.0	7.1 ± 1.2	8.4 ± 2.1	7.4 ± 1.1	8.3 ± 1.5	7.0 ± 0.9	7.5 ± 1.9	1000 s/mm^2 (TE = 65.66 ms)
	Full liver coverage ROI										Max. b-value
ADC [$\times 10^{-3}$ mm^2/s]	1.86 ± 1.2										pool of candidates
SNR	7.2 ± 2.5										1000 s/mm^2 (TE = 65.66 ms)

polyvinylpyrrolidone (Imaging, 1997) was imaged under a 0°C ice-water bath with an 8-channel head coil in a 1.5T scanner (GE Healthcare, Waukesha, WI). Axial diffusion-weighted images were acquired with a Field-of-View (FOV) of 24 × 24 cm, matrix size of 144 × 144, slice thickness of 5 mm, Repetition Time (TR) = 2 s, Echo Time (TE) = 111 ms, and parallel imaging acceleration factor of 2. Acquisitions were performed with N = 41 b-values uniformly distributed between 0 and 2000 s/mm^2. Further, this acquisition was repeated 16 consecutive times to enable voxel-wise determination of ADC and SNR statistics. The first three repetitions were discarded to avoid steady-state effects.

In order to perform T_2 mapping, 2D spin-echo images were acquired with FOV = 24 × 24 cm, matrix size of 128 × 96, slice thickness of 6 mm, TR = 1 s, and TE = [6, 50, 200] ms.

SNR of the S_0 images was computed voxel-wise by calculating the ratio between the mean signal intensity and the standard deviation across the 13 repetitions considered. Ground truth ADC was obtained with a maximum likelihood estimator (initialized with a least squares estimation) using all the diffusion-weighted images and b-values in the range 0 - 1000 s/mm^2. T_2 maps were estimated with a least square fitting. For the evaluation of SNR, ADC, and T_2, a 3.15 cm^2 Region of Interest (ROI) was drawn in each vial, co-localized across the different acquisitions. All parametric maps were obtained to fully describe the quantitative diffusion phantom used in the experiments. Mean SNR, mean ground truth ADC, mean T_2 values of each vial, and pool of N b-values used on the acquisitions are shown in Table 7.1. It is worth noticing that this phantom contains vials for a large range of ADC values although they have unrealistic and long T_2 values (300 to 900 ms).

7.2.2.2 Acetone phantom

Axial diffusion-weighted images of the same ten-vial acetone-based diffusion phantom constructed in Chapter 4 (Peña-Nogales et al., 2019b; Wang et al., 2017) were acquired under a 0°C ice-water bath with an 8-channel head coil on the same 1.5T scanner as before. The acquisition parameters were: FOV of 20 × 10 cm, matrix size of 64 × 64, slice thickness of 10 mm, TR = 1 s, and parallel imaging acceleration factor of 2. Diffusion-weighting was performed with N = 15, 21, 27, 31 and 41 b-values uniformly distributed between 0 and 700 (TE = 70 ms), 0 and 1000 (TE = 75.9 ms), 0 and 1300 (TE = 80.8 ms), 0 and 1500 (TE = 83.6 ms), and 0 and 2000 s/mm^2 (TE = 89.7 ms), respectively. All acquisitions were repeated 16 consecutive times to enable voxel-wise determination of ADC and SNR statistics. No repetition was discarded due to steady-state effects.

In order to perform T_2 mapping, 2D Spin Echo (SE) images were also acquired with FOV = 26 × 15.6, matrix size of 256 × 160, slice thickness of 10 mm, TR = 1 s, and TE = [9, 14, 65, 139, 300] ms.

The same procedures as with the previous quantitative diffusion phantom were carried out to compute the SNR, ground truth ADC (in this case, only using the

Table 7.4: Experiments carried out on each dataset to obtain optimized CRLB-based b-value sets.

Dataset	CRLB-based b-value sets	Number of b-values of the set (K)	Number of b-values of the pool of candidates (N)
Table 7.1	Greedy algorithm	13	41
Table 7.2	Greedy algorithm	16	15, 21, 27, 31, 41
	Two b-value search	2 - 16	
Table 7.3	Greedy algorithm	16	11
	Two b-value search	2 - 16	

acquisition with TE = 75.9 ms and maximum b-value of 1000 s/mm^2) and T_2. For this phantom, a 2.5 cm^2 ROI was drawn in each vial, co-localized across the different acquisitions. All parametric maps were obtained to fully describe the acetone phantom used in the experiments. Mean SNR, mean ground truth ADC, mean T_2 values of each vial, and the pool of N b-values used on the acquisitions are shown in Table 7.2. This phantom contains vials for a limited range of ADC values but they have realistic and short T_2 values (around 37 and 86 ms).

7.2.2.3 In-vivo liver DWI

One healthy volunteer (female, 23 years old) was scanned with institutional review board approval and informed written consent. The acquisition was done with a 16-channel torso coil in a 3T scanner (Philips Healthcare, Best, The Netherlands). Axial diffusion-weighted images were acquired including liver segments III to VIII with respiratory triggering. Other acquisition parameters were: FOV = 22 × 20 cm, matrix size of 100 × 92, slice thickness of 7 mm, space between slices of 7 mm, TR = 911 ms, TE = 65.66 ms, and parallel imaging factor of 2. N = 11 b-values were employed, uniformly distributed between 0 and 1000 s/mm^2. The whole acquisition was repeated 16 consecutive times to enable voxel-wise determination of ADC and SNR statistics. A T_2 weighted sequence was not applied due to time constraints.

SNR maps and ground truth ADC were calculated as in the quantitative diffusion phantom experiment. Three 30 mm^2 ROIs were drawn on each slice. In addition, another larger ROI was drawn with full liver coverage. In both cases, ROIs were co-localized across the different acquisitions. Care was taken to avoid large vessels. All parametric maps were obtained to fully describe the liver acquisition used in the experiments. Mean SNR, mean ground truth ADC values of each ROI, and the pool of b-values used on the acquisitions are shown in Table 7.3.

7.2.3 Experimental validation

Based on the previous acquisitions, four different experiments were performed for the validation of the proposed methods. The first three constitute a procedure

to experimentally obtain an optimized set of K b-values selected from a pool of N candidates, so that it can be compared to the proposed CRLB-based b-value sets. The last experiment is designed to prove the superiority of the proposed CRLB-based b-value sets compared to sets of b-values proposed on the literature for liver DWI.

- Experiment 1: For each DWI acquisition considered, several ROIs were delineated. Then, for each ROI of each acquisition we iteratively obtained the optimized set of K b-values by adding, at each iteration, the b-value that achieved the minimum experimental mean $\mathrm{CRLB}_{\mathrm{ADC}}$ among the available b-value pool of candidates. The procedure is analogous to the one employed in the proposed greedy algorithm, but now the $\mathrm{CRLB}_{\mathrm{ADC}}$ is computed voxel-wise, from voxel-wise ADC and SNR estimates within the ROI. This experiment constitutes a procedure to experimentally obtain optimized sets of K b-values with minimum $\mathrm{CRLB}_{\mathrm{ADC}}$ for ROIs drawn on DW-MRI images, so that they can be compared with the corresponding proposed CRLB-based b-value sets.

- Experiment 2: Based on the mean SNR and mean ground truth ADC that were estimated for each ROI of each acquisition, and their pool of b-values (see Tables 7.1, 7.2, and 7.3), repeated synthetic Diffusion-Weighted (DW) images were generated. Then, we iteratively obtained the optimized set of K b-values by adding, at each iteration, the b-value that achieved minimum experimental variance of the ADC estimation (σ^2_{ADC}) on the synthetic DW images among the available b-value pool of candidates. The procedure is analogous to the one employed in the greedy algorithm, although now the estimated experimental variance (σ^2_{ADC}) is minimized instead of the $\mathrm{CRLB}_{\mathrm{ADC}}$. This experiment constitutes a procedure to experimentally obtain optimized sets of K b-values with minimum σ^2_{ADC} for synthetic DW-MRI images, so that they can be compared with the corresponding proposed CRLB-based b-value sets.

  For both the quantitative diffusion and the acetone phantom acquisitions, synthetic diffusion-weighted images of 10000 pixels per vial and SNR level were created corresponding to the values given in Table 7.1 and 7.2. For the former acquisition, diffusion-weighting was performed with N = 41 b-values uniformly distributed between 0 and 2000 s/mm^2. For the latter acquisition, diffusion-weighting was performed with N = 15, 21, 27, 31, and 41 b-values uniformly distributed between 0 and 700, 0 and 1000, 0 and 1300, 0 and 1500, and 0 and 2000 s/mm^2, respectively. All DW images were corrupted with noise following a Rician distribution. These synthetic images were created 16 consecutive times.

- Experiment 3: For each DWI acquisition considered, several ROIs were delineated. Then, for each ROI of each acquisition we iteratively obtained the optimized set of K b-values by adding, at each iteration, the b-value that achieved the minimum experimental variance of the ADC estimation (σ^2_{ADC}) among the available b-value pool of candidates for a particular ROI. The procedure is analogous to the one employed in the validation through the experiment 2 although with co-localized ROIs drawn on repeated phantom or

Table 7.5: Validation experiments carried out on each DWI acquisition to validate the optimized CRLB-based b-value sets.

DWI acquisitions	Optimized b-value sets	Validation Experiments
Quantitative diffusion phantom experiments	CRLB-based b-value sets: - Greedy algorithm	Experiment 1 Experiment 2 Experiment 3
Acetone phantom experiments	CRLB-based b-value sets: - Greedy algorithm - Two b-value search	Experiment 1 Experiment 2 Experiment 3
In-vivo liver experiments	CRLB-based b-value sets: - Greedy algorithm - Two b-value search	Experiment 1 Experiment 3

in-vivo DWI data. This experiment constitutes a procedure to experimentally obtain optimized sets of K b-values with minimum σ^2_{ADC} for ROIs drawn on DW-MRI images, so that they can be compared with the corresponding proposed CRLB-based b-value sets.

In all previous three methods, ADC maps were obtained with a ML estimator initialized with a least squares estimation. Further, when a b-value was repeated on the selected set, equivalent number of DW images of the consecutive repetitions were selected for ADC estimation. It is worth noticing that the quantitative diffusion phantom acquisition, the acetone phantom acquisition, and the in-vivo liver DWI acquisition were repeated 13, 16, and 16 consecutive times, respectively. For the sake of clarity, these approaches are described in Figure 7.1, and Table 7.5 summarizes which experimental validation methods were employed to validate the proposed b-value determination methods for each of the three types of experimental data.

- Experiment 4: Given a set of b-values, DW images of a DWI acquisition were selected for ADC estimation. However, if a b-value was repeated on the selected set, an equivalent number of DW images of the consecutive repetitions were selected (it is to be noted that as described in Section 7.2.2.3, the whole DWI acquisition, with its 11 uniformly distributed b-values, was repeatedly acquired 16 consecutive times). Hence, this method was repeated 16 times, one for each acquisition, obtaining a total set of 16 different ADC maps. Then, we obtained the voxelwise standard deviation statistics (σ_{ADC}) and the mean ADC map across all the estimated maps. ADC was estimated as described in the previous three experiments. This experiment constitutes a procedure to experimentally compare the achieved noise performance (i.e., σ_{ADC}) of various b-value sets.

7.2.4 Statistical analysis

Provided a set of maps obtained through experiment 4 (i.e., σ_{ADC} maps or mean ADC maps) for various sets of b-values, we computed the statistics described next.

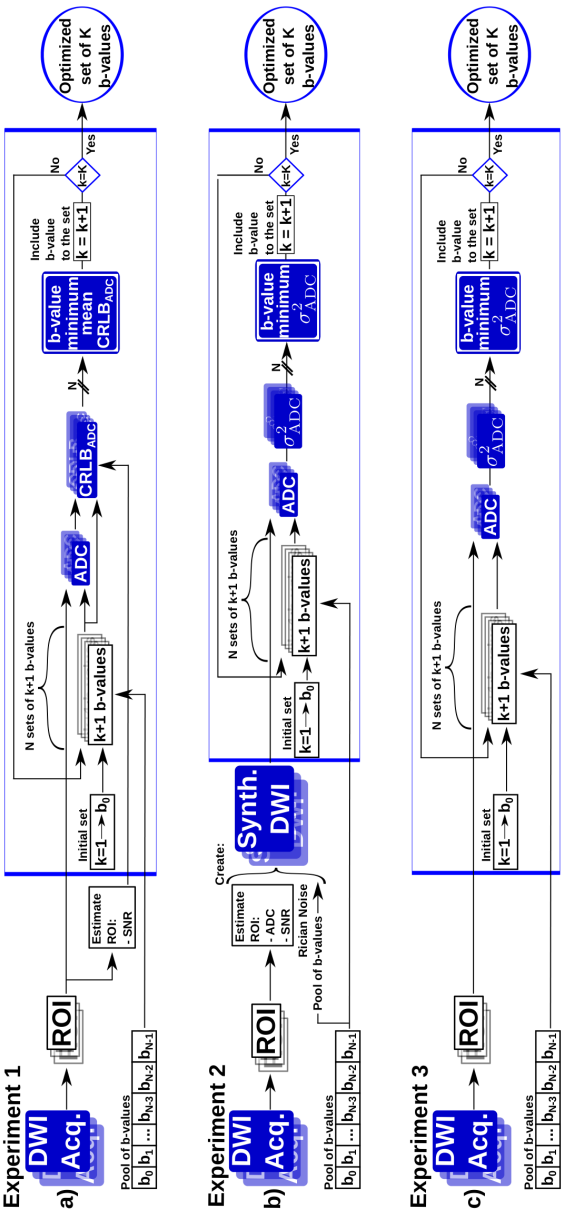

Figure 7.1: Flow diagrams illustrating the optimization processes used to validate the optimized CRLB-based b-value sets obtained through the greedy algorithm. The experimental validation is performed by means of three different experiments, all of which start from a set of b-values composed of b-value = 0 s/mm^2 (b_0), and iterate until a set of K b-values is complete. (a) Experiment 1 - from co-localized ROIs drawn on repeated DWI acquisitions, we iteratively add to the set the b-value that achieves minimum experimental mean $\mathrm{CRLB}_{\mathrm{ADC}}$ among the b-value pool of candidates. (b) Experiment 2 - from synthetic and repeated DW images, we iteratively add to the set the b-value that achieves minimum σ^2_{ADC} among the b-value pool of candidates. (c) Experiment 3 - from co-localized ROIs drawn on repeated DWI acquisitions, we iteratively add to the set the b-value that achieves minimum σ^2_{ADC} among the b-value pool of candidates. It is to be noted that a DWI acquisition has the same number of weighted images as b-values in the pool of candidates (N), k is the number of optimized b-values in the set at each iteration. Further, the ADC blue box estimates the ADC maps with a voxelwise maximum likelihood estimator using only the DW images of the b-values of the selected set. When a b-value is repeated on the set, the equivalent number of DW images of the consecutive repetitions are selected. The $\mathrm{CRLB}_{\mathrm{ADC}}$ blue box computes the $\mathrm{CRLB}_{\mathrm{ADC}}$ maps for a set of b-values, ADC map, and SNR of ROI of the DW S_0 images.

Separately, slices of the ROI with full liver coverage were tested for normality using the Kolmogorov-Smirnov test. Next, the non-parametric Kruskal-Wallis test was applied to reject the null hypothesis that all sets of maps come from the same distribution. Then, we pairwise compared the control maps (the ones obtained through the proposed optimized CRLB-based b-value sets under the Rician noise assumption) with the other sets of maps to test if the distributions were different using a paired, two-sided Wilcoxon signed rank test. Finally, the Bonferroni multiple-comparison post-hoc correction was used when comparing multiple times the same control map. Therefore, for a single comparison the p-value < 0.05 (P) was considered significant, while for multiple comparisons it was p-value $< 0.05/8 = 0.006$. In addition, to quantify the difference between maps we computed the standardized absolute effect size corresponding to the Wilcoxon signed rank test.

7.3 Results

7.3.1 Quantitative diffusion phantom experiments

Figure 7.2 shows a color-coded comparison of the optimized CRLB-based $K = 13$ b-value sets of the 13-vial quantitative diffusion phantom, and the optimized validation sets of $K = 13$ b-values obtained through experiments 1, 2, and 3. Each column shows the optimized set of b-values found for a vial, where the color code indicates how many times a certain b-value was included in the set. Optimized sets of b-values of vials with lowest ADC (i.e., vials 1 - 4) are constrained by the maximum b-value of the pool of candidates. On the other hand, optimized sets of vials 5 to 13 are within the range of the b-value pool of candidates. Higher ADC values achieved a lower optimized set of b-values. Overall, there is good agreement between the optimized CRLB-based b-value sets and the optimized validation sets from all three experiments.

7.3.2 Acetone phantom experiments

Similarly to the previous phantom, Figure 7.3 shows a color-coded comparison of the optimized CRLB-based $K = 16$ b-value sets for each of the five acquisitions with different maximum b-value of the 10-vials acetone phantom (Figure 7.3.a)), and the optimized validation sets of $K = 16$ b-values obtained through experiments 1, 2, and 3 (Figure 7.3.b)-d)). Each column of each sub-figure shows the optimized set found for a vial. Optimized CRLB-based b-value sets and the optimized validation b-value sets from experiments 1 and 2 of vials 1 to 3 and 8 to 10 on the acquisition with maximum b-value of 700 s/mm^2 (TE = 70 ms), and vials 1 and 10 on the acquisition with maximum b-value of 1000 s/mm^2 (TE = 75.9 ms) are constrained by the maximum b-value of the pool of candidates. Further, experiment 1 shows that vials 6 and 7 have lower SNR and marginally higher ADC values than vials 5 and 4 (see Table 7.2), respectively. However, the b-values of their optimized

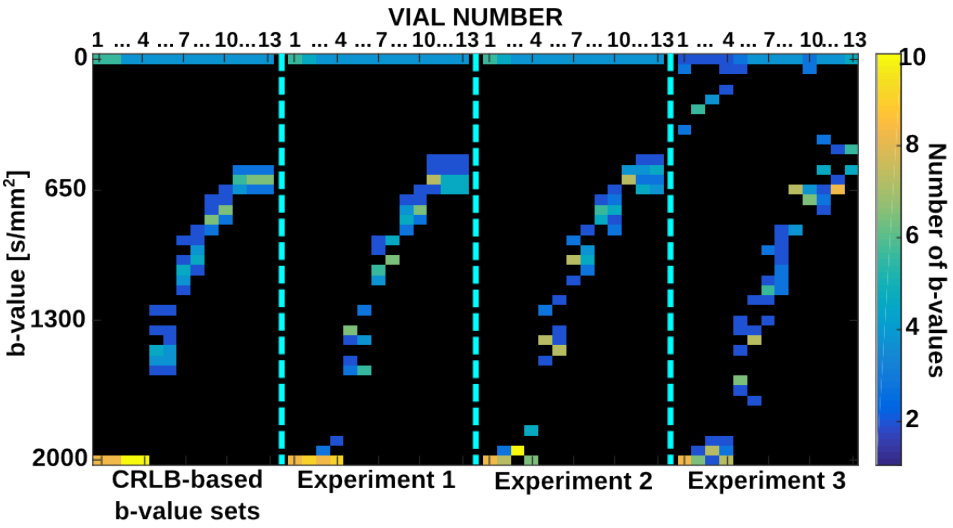

Figure 7.2: Optimized b-value sets. Optimized CRLB-based K=13 b-value sets of the 13-vials quantitative diffusion phantom, and optimized validation sets of K=13 b-values obtained from experiment 1, 2, and 3. Each column shows the optimized set of b-values found for each vial, where the color code indicates how many times a certain b-value was included in the optimized set. Black background color represents zero number of b-values. Optimizations were performed via the greedy algorithm. Vials characteristics to obtain the CRLB-based b-value sets and to perform experiment 2 are given in Table 7.1. There is good agreement between the optimized CRLB-based b-value sets and the optimized validation sets of all three experiments.

sets are lower. Similarly, vials 8, 9, and 10 have lower SNR and marginally lower ADC values than vials 3, 2, and 1, respectively. However, the b-values of their optimized sets are similar. Overall, there is good agreement between the optimized set of b-values obtained with the proposed CRLB-based analysis and the optimized validation sets from all three experiments.

Figure 7.4 illustrates the evolution of the $\mathrm{CRLB}_{\mathrm{ADC}}$ and the evolution of the variance of the ADC (σ^2_{ADC}) for each b-value of the pool of candidates and the 15 first iterations of the greedy algorithm. Figure 7.4.a) depicts both, the $\mathrm{CRLB}_{\mathrm{ADC}}$ evolution to obtain the optimized CRLB-based $K = 16$ b-value set, and the same evolution of experiment 1 when applied to vial 4 of the acquisition with maximum b-value = 2000 s/mm^2 (TE = 89.7 ms). Further, it also shows the σ^2_{ADC} evolutions of experiments 2 and 3 for the same vial. The number of b-values (k) corresponds to the number of b-values of the set at each iteration of the greedy algorithm. Figure 7.4.a) also depicts the $\mathrm{CRLB}_{\mathrm{ADC}}$ of the two b-value search algorithm for K b-values and same vial. The CRLB-based analysis through the greedy algorithm and experiment 1 achieves a similar $\mathrm{CRLB}_{\mathrm{ADC}}$ evolution. At each iteration, their local optimum coincides with the optimal $\mathrm{CRLB}_{\mathrm{ADC}}$ of the CRLB-based analysis through the two b-value search algorithm for the same number of b-values. The σ^2_{ADC} evolution of experiment 3 shows strong agreement with the σ^2_{ADC} of experiment 2,

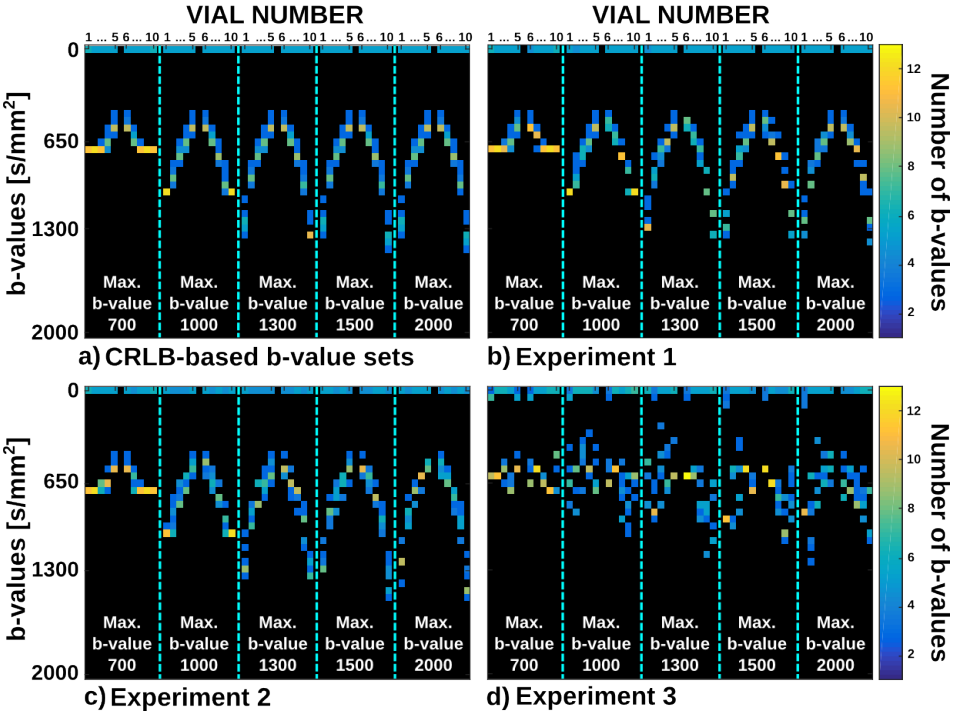

Figure 7.3: Optimized b-value sets. (a) Optimized CRLB-based K=16 b-value sets for each of the five acquisitions with different maximum bvalue of the 10-vials acetone phantom, and (b) optimized validation sets of K=16 b-values obtained from experiment 1, (c) experiment 2, and (d) experiment 3. Each column of each subfigure shows the optimized set of b-values found for each vial, where the color code indicates how many times a certain b-value was included in the optimized set. Black background color represents zero number of b-values. Optimizations were performed via the greedy algorithm. Vials characteristics to obtain the CRLB-based b-value sets and to perform experiment 2 are given in Table 7.2. There is good agreement between the optimized CRLB-based b-value sets and the optimized validation sets of all three experiments.

and the CRLB_{ADC} evolution of the CRLB-based analysis and experiment 1.

7.3.3 In-vivo liver DWI experiments

Figure 7.5 shows a color-coded comparison of the optimized CRLB-based $K = 16$ b-value sets for all ROIs of the liver DWI acquisition obtained under both the Gaussian and Rician noise assumptions Figure 7.5.a) and b), respectively, and the optimized validation sets of $K = 16$ b-values obtained through experiment 1 and 3 (Figure 7.5.c) and d), respectively). ROIs with similar SNR level and different ADC (i.e., ROIs 15 - 30, and 1 - 7, see Table 7.3) have different optimized sets of b-values, obtaining lower b-values for higher ADC values. ROIs with same ADC and different SNR (i.e., ROIs 7 - 9, 10 - 23, and 22 - 14) have different optimized

sets of b-values, obtaining lower b-values for lower SNR levels. In general, there is good agreement between the proposed optimized CRLB-based b-value sets under both noise assumptions and the optimized validation sets from experiments 1 and 3. However, the optimized b-values obtained under the Gaussian noise assumption are higher than those obtained with a Rician assumption, and more differences can be found with respect to the values obtained in experiment 3 (i.e., ROIs 22-27)

Figure 7.4.b) illustrates both the CRLB_{ADC} evolution of the greedy algorithm to obtain the CRLB-based $K = 16$ b-value set and the same evolution for experiment 1 for ROI 8. Further, it also presents the σ^2_{ADC} evolution of experiment 3. Figure 7.4.b) also depicts the CRLB_{ADC} of the two b-value search algorithm for K b-values and same ROI. The CRLB_{ADC} evolution to obtain the CRLB-based analysis through the greedy algorithm is lower than the CRLB_{ADC} of experiment 1, and at each iteration, it achieves a similar local optimal than the two b-value search algorithm. Further, on iterations with $k \geq 5$, the σ^2_{ADC} evolution of experiment 3 is similar but higher than the CRLB_{ADC} of experiment 1. Contrary, on iterations with $k < 5$ the σ^2_{ADC} evolution is similar, and sometimes lower, than the CRLB_{ADC} evolution of both, the CRLB-based analysis and experiment 1.

Figure 7.6 shows the performance comparison in terms of the voxelwise standard deviation reductions (i.e., $\frac{\sigma_{\text{ADC}} - \sigma_{\text{ADC-Rician}}}{\sigma_{\text{ADC}}}$) between the proposed optimized CRLB-based b-value set obtained under the Rician noise assumption and the b-value sets proposed in the literature for in-vivo liver DWI. The sets of b-values found in the literature are described in Table 7.6 entrances 2 to 9). The σ_{ADC} and the mean ADC for each set of b-values were computed as described in experiment 4. The proposed set achieves lower voxelwise standard deviation ($\sigma_{\text{ADC-Rician}}$) than any other set of the literature as shown in Figure 7.6.b)-i). Figure 7.6.j and k) further confirm that the standard deviation of the estimated ADC, and therefore the variance, of the proposed set of b-values is lower than in the other eight literature cases. Particularly, the boxplot of the σ_{ADC} has the lowest median with the narrowest Interquartile Range (IQR) as shown in Table 7.7 and Figure 7.6.j). Namely, the σ_{ADC} reduction of the proposed set of b-values compared to the other literature sets is of 6.25%, 21.05%, 31.82%, 54.55%, 42.31%, 50.00%, 44.44%, and 48.28%, respectively, for each of the entries of Table 7.7. Similarly, in Figure 7.6.k) the boxplot of the mean ADC has the narrowest IQR (see Table 7.7). The IQR reduction of the proposed set of b-values compared to the other literature sets is of 24.74%, 17.05%, 38.14%, 68.40%, 68.80%, 70.33%, 17.98%, and 48.59%, respectively. The values of both boxplots were taken from the corresponding slice of the full liver coverage ROI. Further, statistically significant differences ($P < 0.006$) were found between the σ_{ADC} maps computed with the proposed b-value set (Rician) and all the other literature cases. On the other hand, with the mean ADC maps statistically significant differences were found between the proposed set and all the other literature cases except for Koc and Erbay (2014) ($P = 0.79$), Kaya and Koc (2014) ($P = 0.42$), and Taouli and Koh (2009) ($P = 0.10$). However, it is to be noted that the reduction of the Rician mean ADC IQR compared to those three cases is around 70% (see Table 7.7). Moreover, as described by the standardized effect size shown in Table 7.8, the differences between the σ_{ADC} comparisons can be described between medium and small. Further, standardized effect sizes of the

Table 7.6: Sets of b-values recommended on the literature for healthy in-vivo liver DWI. The sets proposed by Xing et al. (1997) and Brihuega-Moreno et al. (2003) are equivalent to those obtained under the Gaussian noise assumption for the two b-value search algorithm.

	Manuscript	b-values (NEX*)
1)	Proposed optimized CRLB-based b-value set	0(4) 600(12)
2)	Xing et al. (1997) and Brihuega-Moreno et al. (2003)	0(3) 700(13)
3)	Saritas et al. (2011)	0(4) 500(12)
4)	Goshima et al. (2008)	0(8) 400(8)
5)	Koc and Erbay (2014)	0(2) 100(2) 200(2) 400(2) 600(2) 800(3) 1000(3)
6)	Kaya and Koc (2014)	0(3) 100(3†) 600(3) 800(3) 1000(4)
7)	Taouli and Koh (2009)	0(3) 100(4†) 500(3) 700(3) 1000(3)
8)	Padhani et al. (2009b)	100(4) 200(4) 500(4) 700(4)
9)	Koh and Collins (2007)	0(2) 100(5†) 300(3†) 500(3) 800(3†)

* b-Value sets are composed of $K = 16$ b-values. Therefore, the b-values recommended in the literature were repeated until a set of $K = 16$ was achieved. If K was not a multiple of the number of b-values proposed in the set, priority was given to the higher b-values as recommended by Padhani et al. (2009b).
† Some or all of these repeated b-values where rounded to allow ADC estimation with the b-values available in the current in-vivo liver DWI experiment.

mean ADC comparisons are also between medium and small for all cases except for the comparisons with Koc and Erbay (2014), Kaya and Koc (2014), and Taouli and Koh (2009) which are very small according to Cohen (2013).

7.3.4 b-Value optimization

The two b-value search algorithm and the greedy algorithm achieve similar optimal CRLB_{ADC} as shown in Figure 7.4 for the acetone phantom experiment and the in-vivo liver experiment. The optimized CRLB-based b-value sets obtained with the two b-value search algorithm are composed of k_1 equal b-values to 0 s/mm^2, and k_2 equal b-values different to 0 s/mm^2 (hereinafter so called optimized b-value), where $k_1 + k_2 = K$, as shown in Table 7.9. Various relationships between the optimized b-value, K, k_1, target ADC, SNR level, noise distribution, and b-value pool of candidates are shown in Figure 7.6. Figure 7.6.a) depicts the product between the optimized b-value and the target ADC for SNR levels of 100, 50, 20, and 10, target ADC values of 2.1, 1.2, and 0.9 mm^2/s, pool of candidates with N = 2001 b-values uniformly distributed between 0 and 2000 s/mm^2, and assuming a Rician noise distribution. The product between the optimized b-value and target ADC is the same independently of the target ADC, however, it decreases for low SNR levels under a Rician noise distribution assumption. For SNR levels of 100 and 10, the ratio converges to 1.274 and 1.203, respectively. Figure 7.6.b) shows the ratio between K and k_1 for the same parameters than Figure 7.6.a). K/k_1 ratio is the same independently of the target ADC, however, it decreases for low SNR levels under a Rician noise distribution assumption. For SNR levels of 100 and 10, the ratio converges to 4.545 and 4.347, respectively. Further, convergence product and ratio values change when the lowest b-value of the pool of candidates increases (results not shown).

Figure 7.7.c) and 7.7.d) show the same ratio K/k_1 for the same SNR levels, pool of candidates with N = 701 b-values uniformly distributed between 0 and

Table 7.7: Median (Interquartile Range (IQR)) of the σ_{ADC}, and the mean ADC of each of the set of b-values of Table 7.6 on a representative slice of the liver. σ_{ADC}, and the mean ADC were computed as described in experiment 4. The values considered for the computation of the medians and the IQRs were taken from the corresponding slice of the full liver coverage ROI. It is to be noted that the σ_{ADC} obtained by the proposed optimized CRLB-based b-value set under the Rician noise assumption achieves the lowest median, and the mean ADC achieves the lowest dispersion (i.e., lowest IQR).

	Manuscript	σ_{ADC}	Mean ADC
		Median (IQR)	[$\times 10^{-3}$ mm^2/s]
1)	Proposed optimized CRLB-based b-value set	0.15 (0.15)	1.78 (0.73)
2)	Xing et al. (1997) and Brihuega-Moreno et al. (2003)	0.16 (0.19)	1.75 (0.97)
3)	Saritas et al. (2011)	0.19 (0.17)	2.04 (0.88)
4)	Goshima et al. (2008)	0.22 (0.23)	2.23 (1.18)
5)	Koc and Erbay (2014)	0.33 (3.21)	1.44 (2.31)
6)	Kaya and Koc (2014)	0.26 (2.74)	1.53 (2.34)
7)	Taouli and Koh (2009)	0.30 (3.37)	1.62 (2.46)
8)	Padhani et al. (2009b)	0.27 (0.40)	1.37 (0.89)
9)	Koh and Collins (2007)	0.29 (1.38)	1.35 (1.42)

700 s/mm^2, assuming a Rician noise distribution, and target ADC values of 1.2 and 0.9 mm^2/s, respectively. In these two cases, the optimized b-value corresponds to the highest b-value of the pool of candidates (i.e., 700 s/mm^2) for any K. However, K/k_1 ratio depends on the target ADC as shown in Figure 7.7.c)-d). Further, for all SNR levels the ratio converge to 3.333 and 2.857 for both ADC values, respectively. In addition, for target ADC of 2.1 mm^2/s, and b-value pool of candidates between 0 and 700 s/mm^2, the product ratio are as shown in Figure 7.7.a)-b), respectively.

Finally, neither the product between the optimized b-value and the target ADC nor the K/k_1 ratio depend on the SNR level under a Gaussian noise assumption. In this case, all products and ratios are the same as for a high SNR under the Rician noise distribution as shown for various optimized b-value sets given in Table 7.9.

7.4 Discussion

In this chapter, we derived the Cramér-Rao Lower Bound (CRLB) of the monoexponential diffusion isotropic model under a realistic noise assumption. This formulation provides an optimized set of b-values that maximize the noise performance (i.e., maximize the precision and minimize the variance) of Apparent Diffusion Coefficient (ADC) mapping in liver DWI. Optimized CRLB-based b-value sets tend to be composed of two groups of b-values as shown by both the greedy and the two b-value search algorithms. In our in-vivo liver DWI experiment with one healthy subject, these two approaches attain similar CRLB, and the two b-value search algorithm generally obtains a better performance. However, this in-vivo experiment is not conclusive to distinguish between both optimization algorithms. Particularly, the two b-value set algorithm can be used to quickly compute an optimized set of b-values given the number of b-values of the set (K),

Table 7.8: Effect size (P-value) of the σ_{ADC}, and the mean ADC resulting from the Wilcoxon signed rank test comparison between the proposed optimized CRLB-based b-value set (element 1) of Table 7.6 and the sets of b-values proposed in the literature (elements 2) to 9) of Table 7.6 on a representative slice of the liver. σ_{ADC}, and the mean ADC were computed as described in experiment 4. The standardized absolute effects size is $|Z|/\sqrt{N}$, where Z is the Z-statistic of the test, and N the total number of samples. Effect sizes of the σ_{ADC} comparisons can be described between medium and small, while effects sizes of the mean ADC comparisons are also between medium and small for all cases except for the comparisons with Koc and Erbay (2014), Saritas et al. (2011), and Taouli and Koh (2009) which are very small.

	Rician vs. Manuscript	Effect Size (P-value)	
		σ_{ADC}	Mean ADC
2)	Xing et al. (1997) and Brihuega-Moreno et al. (2003)	0.12 (<0.006)	0.10 (<0.006)
3)	Saritas et al. (2011)	0.28 (<0.006)	0.37 (<0.006)
4)	Goshima et al. (2008)	0.24 (<0.006)	0.40 (<0.006)
5)	Koc and Erbay (2014)	0.49 (<0.006)	0.01 (=0.79)
6)	Kaya and Koc (2014)	0.36 (<0.006)	0.01 (=0.42)
7)	Taouli and Koh (2009)	0.41 (<0.006)	0.03 (=0.10)
8)	Padhani et al. (2009b)	0.36 (<0.006)	0.30 (<0.006)
9)	Koh and Collins (2007)	0.41 (<0.006)	0.24 (<0.006)

target ADC, SNR and noise distribution. This is due to the convergence of the product between the optimized b-value (higher b-value of the set) and the target ADC, and the convergence of the ratio between the number of b-values = 0 s/mm^2 on the set (k_1) and the total number of b-values (K).

Even though formally establishing the clinical relevance of these results for a specific application is out of the scope of this chapter, since it would need a number of acquisitions to be carried out in patients with that specific application in mind, the potential clinical implications of our contribution can be discussed. First, our approach for obtaining of optimized sets of b-values may have an important role in body DWI (particularly in liver DWI), where there is a lack of consensus in the literature (Guiu and Cercueil, 2011) about the optimal set to be employed. Increased quality in ADC estimation does not only facilitate visual discrimination between healthy and diseased tissue, but may also be a key component for quantitative imaging applications focused on characterizing pathological tissues, such as Radiomics (Jeong et al., 2019). Further, this contribution is also a step towards standardization of liver DWI acquisitions, in order to facilitate comparison between studies, and improve noise performance of ADC mapping. In order to pave the way of this standardization process, in Table 7.10 we provide the optimized CRLB-based b-value sets of various healthy and pathological body tissues at various SNR levels under the Rician noise assumption. In addition, the proposed b-value sets may shorten the DWI scan time through the trade off between lower CRLB and number of b-values of the optimized set, and help with the development of tissue-specific DWI sequences.

It has been shown how the optimized CRLB-based K b-value sets are composed of two b-values repeated k_1 and k_2 times respectively, where $k_1 + k_2 = K$, as

Table 7.9: Optimized CRLB-based b-values for different target ADCs, SNR, and number of K b-values of the optimized set. The optimization was performed with the two b-value search algorithm under both Rician and Gaussian noise distribution assumptions with a pool of b-values including 2001 b-values uniformly distributed between 0 and 2000 s/mm^2. The optimized sets obtained under the Gaussian noise assumption are equivalent to those proposed by Xing et al. (1997) and Brihuega-Moreno et al. (2003). It is worth noticing that the optimized CRLB-based b-values under the Gaussian noise distribution assumption are SNR-independent and the same than the ones optimized under the Rician noise distribution assumption for high SNR scenarios.

Noise →		Rician				Gauss
Target ADC		SNR*				SNR*
([mm^2/s])		100	50	20	10	-
K=8 b-values (k_2†)	2.1×10^{-3}	594(6)	593(6)	587(6)	565(6)	594(6)
	1.2×10^{-3}	1039(6)	1038(6)	1027(6)	988(6)	1040(6)
	0.9×10^{-3}	1385(6)	1383(6)	1369(6)	1318(6)	1386(6)
K=15 b-values (k_2†)	2.1×10^{-3}	618(12)	617(12)	610(12)	586(12)	618(12)
	1.2×10^{-3}	1081(12)	1080(12)	1068(12)	1025(12)	1082(12)
	0.9×10^{-3}	1442(12)	1439(12)	1424(12)	1367(12)	1442(12)
K=30 b-values (k_2†)	2.1×10^{-3}	601(23)	600(23)	594(23)	571(23)	601(23)
	1.2×10^{-3}	1052(23)	1050(23)	1040(23)	1000(23)	1052(23)
	0.9×10^{-3}	1402(23)	1400(23)	1386(23)	1333(23)	1403(23)

* SNR corresponds to the SNR of the S_0 images.
† The lower optimized b-value of the sets is always 0 s/mm^2, and $k_1 = K - k_2$.

previously shown through the error propagation formulation by (Fleysher et al., 2008; Kingsley and Monahan, 2004; Saritas et al., 2011; Xing et al., 1997) and with the CRLB formulation by (Brihuega-Moreno et al., 2003). However, most of previous studies only considered DW images to be affected by Gaussian distributed noise. Under that condition, the product between the optimized b-value and the target ADC and the ratio K/k_1 have been shown to be around 1.3 and around 4.6, respectively, by (Brihuega-Moreno et al., 2003; Xing et al., 1997). These previous results are in agreement with our convergence rates for high SNR under the Rician noise distribution assumption. However, at lower SNR both convergence rates decrease, which implies that there is a decrease on the optimized b-value, as well as an increase on the number of times the b-value 0 s/mm^2 (k_1) is repeated in the optimized set to increase data SNR and assist parameter estimation. In general, the proposed optimized CRLB-based set of b-values achieves lower ADC voxelwise

Table 7.10: Optimized CRLB-based b-values for different target tissues, SNR, and number of K b-values of the optimized set. The optimization was performed with the two b-value search algorithm under the Rician noise distribution assumption. Common ADC values of the different tissue types have been extracted from (Koh and Collins, 2007; Lee et al., 2008; Taouli and Koh, 2009), and from our in-vivo liver DWI acquisition. If the MRI scanner does not support some integer values, b-values should be rounded to the closest multiple of 50 or 100. It is to be noted that the lower the SNR the lower are the optimized b-values.

	Target Tissue (ADC [mm^2/s])	K = 8 b-values (k_2*)			K = 15 b-values (k_2*)			K = 30 b-values (k_2*)		
		SNR†			SNR†			SNR†		
		50	20	10	50	20	10	50	20	10
Liver	Healthy (1.86×10^{-3})	667(6)	660(6)	635(6)	694(12)	686(12)	659(12)	675(23)	668(23)	642(23)
	HCCs‡ (1.16×10^{-3})	1000(6)	1000(6)	1000(6)	1000(11)	1000(11)	1000(11)	1000(23)	1000(23)	1000(23)
	Hemangiomas (1.98×10^{-3})	627(6)	620(6)	597(6)	652(12)	645(12)	619(12)	364(23)	628(23)	604(23)
	Cysts (2.85×10^{-3})	437(6)	432(6)	416(6)	455(12)	450(12)	432(12)	442(23)	438(23)	421(23)
Prostate	Peripheral Zone (1.78×10^{-3})	699(6)	692(6)	666(6)	727(12)	719(12)	690(12)	707(23)	700(23)	673(23)
	Central Gland (1.49×10^{-3})	832(6)	824(6)	792(6)	866(12)	856(12)	822(12)	842(23)	833(23)	801(23)
	Cancer (1.29×10^{-3})	960(6)	950(6)	914(6)	999(12)	988(12)	948(12)	972(23)	962(23)	925(23)
Pancreas	Healthy (1.62×10^{-3})	769(6)	761(6)	732(6)	800(12)	791(12)	759(12)	778(23)	770(23)	740(23)
	Adenocarcinoma (1.24×10^{-3})	999(6)	989(6)	952(6)	1000(12)	1000(12)	987(12)	1000(23)	1000(23)	963(23)
	Cyst (2.50×10^{-3})	498(6)	493(6)	474(6)	518(12)	513(12)	492(12)	504(23)	499(23)	480(23)
Kidneys	Cortex (1.83×10^{-3})	680(6)	674(6)	648(6)	708(12)	700(12)	672(12)	689(23)	682(23)	655(23)
	Medulla (1.87×10^{-3})	666(6)	659(6)	634(6)	693(12)	685(12)	658(12)	674(23)	667(23)	641(23)

* The lower optimized b-value of the sets is always 0 s/mm^2, and $k_1 = K$ - k_2.
† SNR corresponds to the SNR of the S_0 images.
‡ HCCs stands for Hepatocellular carcinomas.

standard deviation and also has lower dispersion around the mean ADC than various sets of b-values proposed in the literature for in-vivo liver DWI (Koh and Collins, 2007; Padhani et al., 2009b; Taouli and Koh, 2009) (i.e., mean ADC absolute differences are of 0.16, 0.40, and 0.43 $\times$ 10^{-3} mm^2/s, respectively) as shown in Figure 7.6. The reductions of the σ_{ADC} of the proposed set of b-values are of 50.00%, 44.44%, and 48.28%, respectively, while the dispersion reduction around (i.e., IQR) of the mean ADC is of 70.33%, 17.98%, and 48.59%, respectively.

This work has several limitations. To obtain a CRLB-based b-value set there needs to be a rough prior knowledge of the target ADC and scan SNR. Nevertheless, the former one is tissue-specific, and the latter one can be estimated from an initial pre-scan as done by Saritas et al. (2011); Xing et al. (1997). Although there may be some spatial variations of noise levels in parallel acquisitions (Aja-Fernández and Vegas-Sánchez-Ferrero, 2016), we assume the SNR is constant throughout the DW images. In addition, in regions where the actual ADC is very different from the target ADC (such as blood vessels inside the liver), the performance of the proposed b-value sets can be worse than that of alternative methods (see for instance the greenish regions in Figure 7.6.c-i). In order to tackle within-tissue heterogeneity, which could be important in the case of focal lesions, for instance, the formulation could be extended through a minimax approach or by averaging the $\mathrm{CRLB}_{\mathrm{ADC}}$ prior minimization of the objective function similarly to (Alexander, 2008; Poot et al., 2010).

Additionally, all b-values from a pool of candidates were acquired including b-values higher than the optimized ones unnecessary reducing the SNR of the DWI images due to T_2 effects. However, even though the T_2 exponential decay is not directly included in the formulation, in practice, it is equivalent to decrease the SNR of the S_0 images needed for the computation of the CRLB.

Further, bias, precision, and reproducibility of ADC mapping should be considered together to achieve quantitative diffusion Magnetic Resonance Imaging (MRI). In this work, however, we focus on precision, while we indirectly address bias through the choice of a suitable estimator. Particularly, in this work ADC mapping was performed through a maximum likelihood estimator, which will reach the CRLB limit asymptotically for a large number of samples. Nevertheless, for a small number of samples poor initializations and low SNR might hinder the estimation by stopping at local minima producing bias and low estimated ADC variances.

Finally, due to the lack of patients in this study we were not able to prove the clinical relevance of the proposed approach. However, future work includes further validation in liver DWI, in both healthy volunteers and patients of several pathologies.

7.5 Conclusion

We have derived the Cramér-Rao Lower Bound (CRLB) of the monoexponential diffusion-weighted signal model under a Rician distribution noise assumption, and

proposed a formulation to obtain the optimized set of b-values that maximize the noise performance of the estimated ADC maps (i.e., maximize the precision and minimize the variance). The good agreement between the optimized CRLB-based b-value sets and the optimized validation b-value sets of experiments 1, 2, and 3 may help to optimize and standardize liver DW-MRI acquisitions.

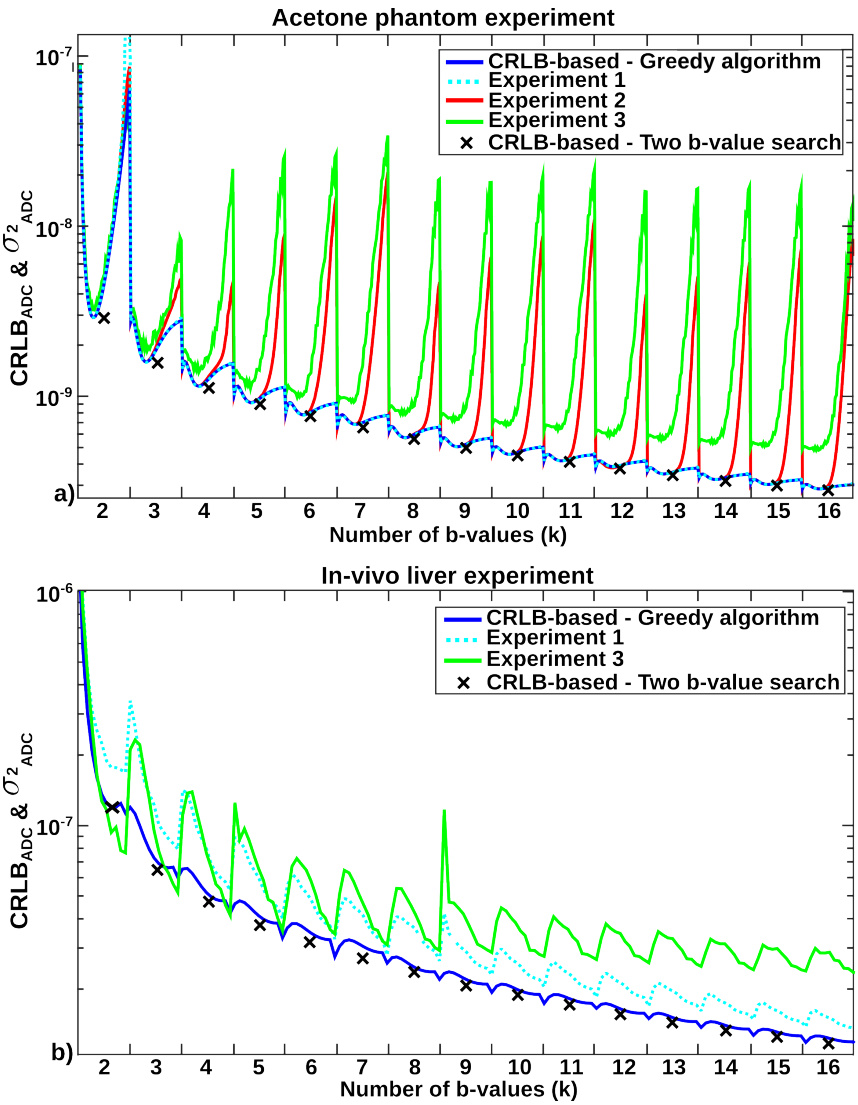

Figure 7.4: Minimization process to obtain the optimized set of b-values. Evolution of the Cramér-Rao Lower Bound of the ADC ($\mathrm{CRLB_{ADC}}$) obtained from the CRLB-based analysis through the greedy algorithm to obtain an optimized K=16 b-value set (blue line), and from experiment 1 (dashed cyan line). Evolution of the variance of the ADC (σ^2_{ADC}) obtained from experiment 2 (red line), and experiment 3 (green line). The $\mathrm{CRLB_{ADC}}$ and the σ^2_{ADC} are shown for each b-value of the pool of candidates and the 15 first iterations of the optimization algorithm. Further, $\mathrm{CRLB_{ADC}}$ of the optimized set of b-values obtained with the two b-value search algorithm for each set of K b-values (black crosses). Crosses are placed on the middle of each k iteration for convenience. (a) $\mathrm{CRLB_{ADC}}$ and σ^2_{ADC} computed for vial 4 of the acetone phantom experiment for the acquisition with TE=89.7 ms and maximum b-value of 2000 s/mm^2. (b) $\mathrm{CRLB_{ADC}}$ and σ^2_{ADC} computed for ROI 8 of the liver DWI acquisition.

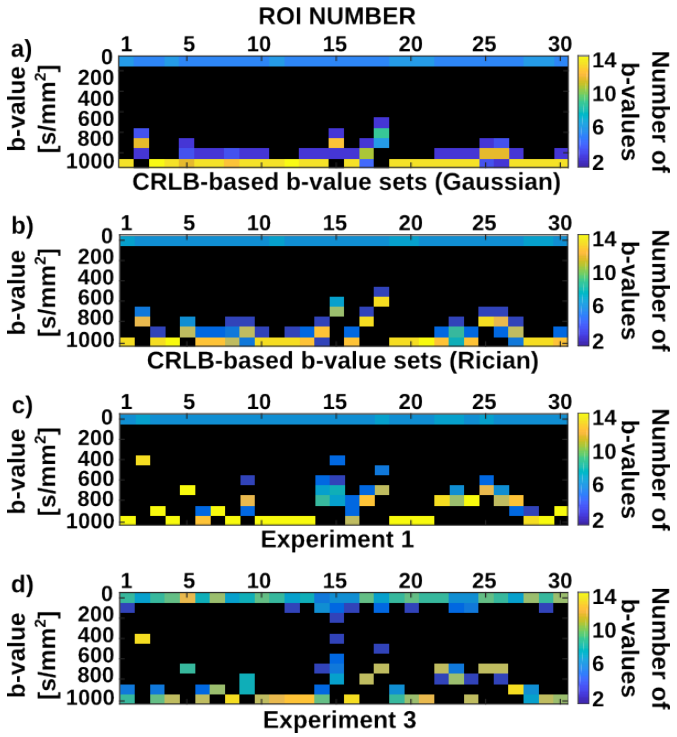

Figure 7.5: Optimized b-value sets. (a and b) Optimized CRLB-based K=16 b-value sets of the 30 ROIs drawn on the in-vivo liver DWI acquisition. (a) Optimized under a Gaussian noise assumption. (b) Optimized under a Rician noise assumption. (c) Optimized validation sets of K=16 b-values obtained from experiment 1, and (d) experiment 3. Each column shows the optimized set of b-values found for each ROI, where the color code indicates how many times a certain b-value was included in the optimized set. Black background color represents zero number of b-values. Optimizations were performed via the greedy algorithm. Vials characteristics to obtain the CRLB-based b-value sets are given in Table 7.3. There is good agreement between the optimized CRLB-based b-value sets obtained under both noise assumptions and the optimized validation sets of experiments 1 and 3. However, the optimized b-values obtained under the Gaussian noise assumption are higher than those obtained with a Rician assumption, and more differences can be found with respect to the values obtained in experiment 3 (i.e., ROIs 22-27).

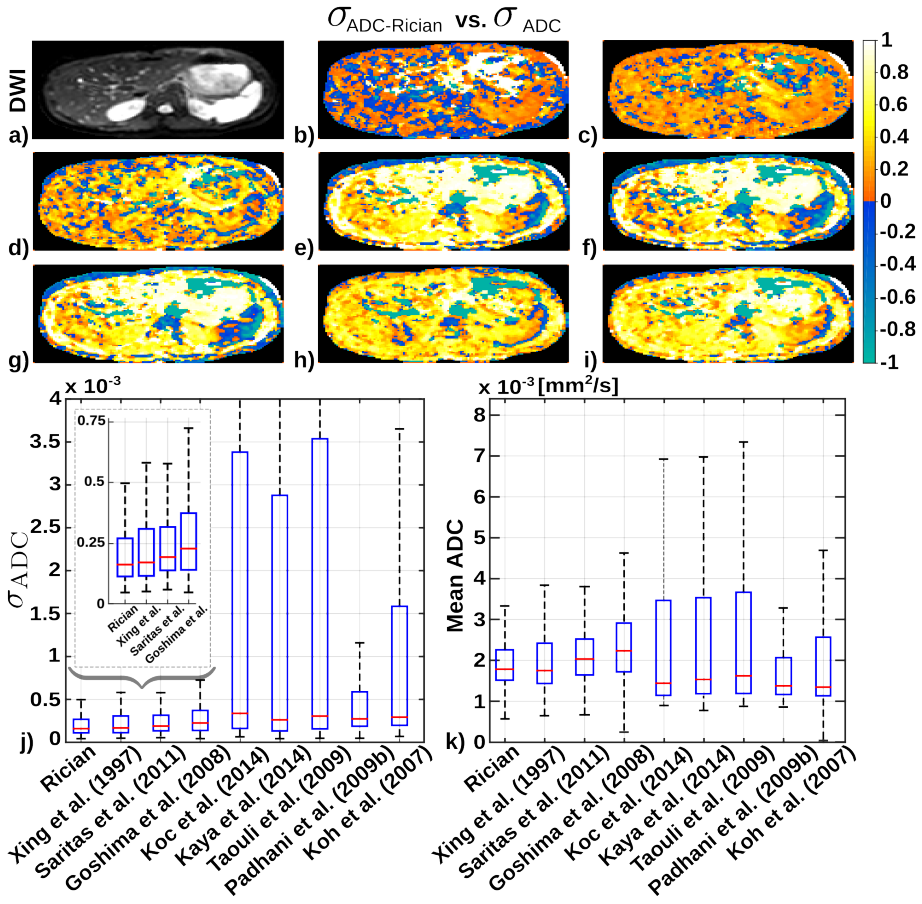

Figure 7.6: Performance comparison between the proposed CRLB-based b-value set obtained under the Rician noise assumption and eight sets of b-values found in the literature (sets 2 to 9) of Table 7.6). a) Diffusion-weighted image at b-value = 0 s/mm^2. b-i) Voxelwise standard deviation reductions, (*i.e.*, $\frac{\sigma_{ADC}-\sigma_{ADC\text{-}Rician}}{\sigma_{ADC}}$), where $\sigma_{\text{ADC-Rician}}$ and σ_{ADC} corresponds to the voxelwise standard deviation of each of the set of b-values of Table 7.6 computed as described in experiment 4. j-k) Corresponding boxplots of the σ_{ADC}, and the mean ADC values of each set of b-values on the corresponding slice of the liver, respectively. Notice that in (j) it is also included a zoomed version of the boxplots of the proposed b-value set, Xing et al. (1997), Saritas et al. (2011), and Goshima et al. (2008), in order to facilitate visual inspection of the results. The proposed set achieves lower voxelwise standard deviation $\sigma_{\text{ADC-Rician}}$ and narrower estimated mean ADC than any other set of the literature (see medians and Interquartile Ranges (IQRs) reported in Table 7.7). The values of both boxplots were taken from the corresponding slice of the full liver coverage ROI. Further, statistical significant differences ($P < 0.006$) were found between the σ_{ADC} maps computed with the proposed b-value set (Rician) and all the other literature cases. On the other hand, with the mean ADC maps statistical significant differences were found between the proposed set and all the other literature cases except for Koc and Erbay (2014) ($P = 0.79$), Kaya and Koc (2014) ($P = 0.42$), and Taouli and Koh (2009) ($P = 0.10$). However, it is to be noted that the reduction of the Rician mean ADC IQR compared to those three cases is around 70% (see Table 7.7 and Table 7.8 for details).

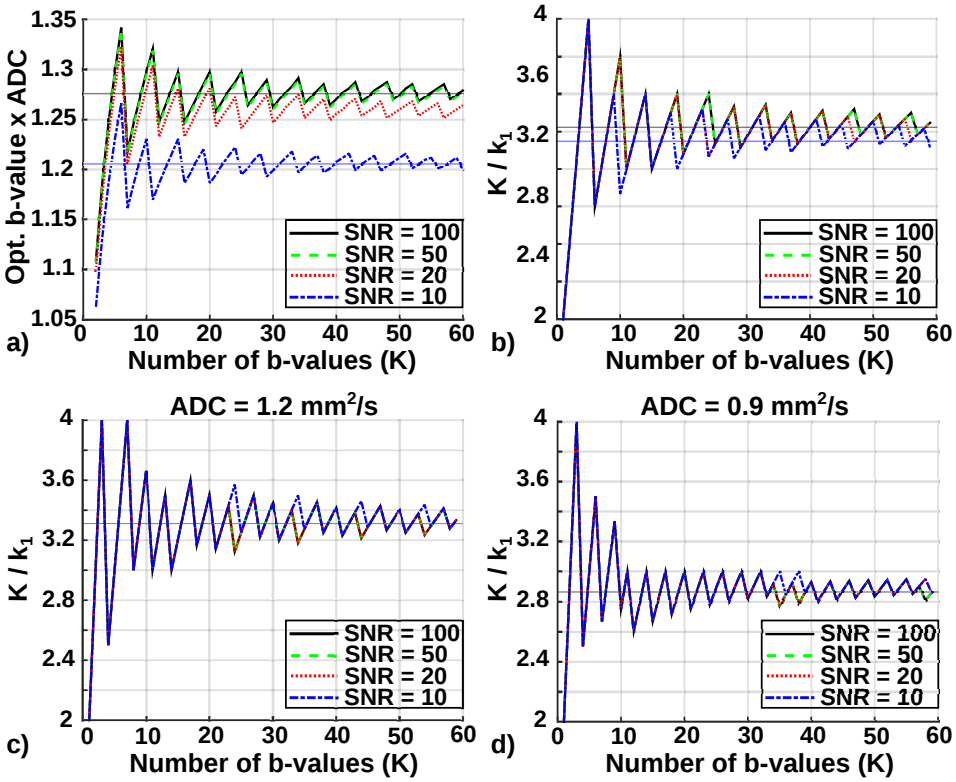

Figure 7.7: b-Value convergence ratios. (a) Product between the optimized b-value (i.e., the k_2 equal b-values different to 0 s/mm^2) and target ADC of the two b-value search algorithm for SNR levels of 100, 50, 20, and 10, target ADC values of 2.1, 1.2, and 0.9 mm^2/s, pool of candidates with N = 2001 b-values uniformly distributed between 0 and 2000 s/mm^2, and assuming a Rician noise distribution. (b) Under the same parameters, ratio between the number of b-values of the optimized set (K), and the number of b-values equal to 0 s/mm^2 (k_1). Ratio between K and k_1 for SNR levels of 100, 50, 20, and 10, pool of candidates with N = 701 b-values uniformly distributed between 0 and 700 s/mm^2, assuming a Rician noise distribution, and target ADC values of 1.2 and 0.9 mm^2/s, (c) and (d), respectively.

8

Determination of the optimal set of b-values for Intravoxel Incoherent Motion (IVIM) parameter mapping in liver Diffusion-Weighted MRI

Contents

8.1 Theory

In the Intravoxel Incoherent Motion (IVIM) biexponential diffusion-weighted signal model introduced in Eq.(2.28) of Section 2.2.3, the measured signal is described

as:

$$S(b) \;=\; S_0\left[fe^{-b\cdot D^*} \;+\; (1-f)e^{-b\cdot ADC}\right], \tag{8.1}$$

where b is the b-value, S_0 is the signal intensity when no diffusion-weighting gradient is applied, D^* is the pseudodiffusion coefficient, D is the diffusion coefficient, and f is the perfusion fraction. Generally, the estimation of the IVIM parameters is performed by voxelwise fitting the previous model to a set of weighted measurements, $S(b_{\mathrm{k}})$ where $k \in [1,\ldots,K]$. Therefore, we seek to maximize the precision and noise performance of D^*, D, and f estimations through the selection of the optimized set of b-values via the Cramér-Rao Lower Bound (CRLB) theory introduced in Chapter 6 under a Rician noise assumption (see Section 2.5.1 for details). This formulation is presented below followed by the methods used to optimize the set of b-values.

8.1.1 Cramér-Rao Lower Bound of the IVIM signal model

Given the noise free model in Eq. (8.1) with the set of parameters $\boldsymbol{\theta} = \{S_0, D^*, D, f\}$ and any noise distribution, the Fisher Information Matrix (FIM) (Van den Bos, 2007) is:

$$\boldsymbol{I}(\boldsymbol{\theta}) = \begin{bmatrix} \sum_{k=1}^{K}[fe^{-b_k\cdot D^*}+(1-f)e^{-b_k\cdot D}]^2\mathcal{I}_n(S(b_k),\sigma) & -\sum_{k=1}^{K}S(b_k)(1-f)b_ke^{-b_kD}\mathcal{I}_n(S(b_k),\sigma) \\ -\sum_{k=1}^{K}S(b_k)(1-f)b_ke^{-b_k\cdot D}\mathcal{I}_n(S(b_k),\sigma) & \sum_{k=1}^{K}S_0^2(1-f)^2b_k^2e^{-2\cdot b_k\cdot D}\mathcal{I}_n(S(b_k),\sigma) \\ \sum_{k=1}^{K}S(b_k)[e^{-b_k\cdot D^*}-e^{-b_k\cdot D}]\mathcal{I}_n(S(b_k),\sigma) & -\sum_{k=1}^{K}S_0^2(1-f)b_k[e^{-b_k\cdot D^*}-e^{-b_k\cdot D}]e^{-b_k\cdot D}\mathcal{I}_n(S(b_k),\sigma) \\ -\sum_{k=1}^{K}S(b_k)fb_ke^{-b_k\cdot D^*}\mathcal{I}_n(S(b_k),\sigma) & \sum_{k=1}^{K}S_0^2(f-f^2)b_k^2e^{-b_k\cdot(D+D^*)}\mathcal{I}_n(S(b_k),\sigma) \end{bmatrix}$$

$$\begin{bmatrix} \sum_{k=1}^{K}S(b_k)[e^{-b_k\cdot D^*}-e^{-b_k\cdot D}]\mathcal{I}_n(S(b_k),\sigma) & -\sum_{k=1}^{K}S(b_k)fb_ke^{-b_k\cdot D^*}\mathcal{I}_n(S(b_k),\sigma) \\ -\sum_{k=1}^{K}S_0^2(1-f)b_k[e^{-b_k\cdot D^*}-e^{-b_k\cdot D}]e^{-b_k\cdot D}\mathcal{I}_n(S(b_k),\sigma) & \sum_{k=1}^{K}S_0^2(f-f^2)b_k^2e^{-b_k\cdot(D+D^*)}\mathcal{I}_n(S(b_k),\sigma) \\ \sum_{k=1}^{K}S_0^2[e^{-b_k\cdot D^*}-e^{-b_k\cdot D}]^2\mathcal{I}_n(S(b_k),\sigma) & -\sum_{k=1}^{K}S_0^2fb_k[e^{-b_k\cdot D^*}-e^{-b_k\cdot D}]e^{-b_k\cdot D^*}\mathcal{I}_n(S(b_k),\sigma) \\ -\sum_{k=1}^{K}S_0^2fb_k[e^{-b_k\cdot D^*}-e^{-b_k\cdot D}]e^{-b_k\cdot D^*}\mathcal{I}_n(S(b_k),\sigma) & \sum_{k=1}^{K}S_0^2f^2b_k^2e^{-2\cdot b_k\cdot D^*}\mathcal{I}_n(S(b_k),\sigma) \end{bmatrix} \tag{8.2}$$

where K is the number of b-values in the set, σ the covariance, and $\mathcal{I}_n(\bullet)$ depends on the noise distribution (i.e., Gaussian (Karlsen et al., 1999) or Rician (Karlsen et al., 1999; Poot et al., 2010)) as shown in Chapter 6.

Therefore, the CRLB (Section 6.2) of the IVIM biexponential Diffusion-Weighted Imaging (DWI) signal model is given by inverting Eq. (8.2) as shown in the CRLB inequality (6.2). The CRLB will depend on the set of b-values, the total number of b-values (K) of the set, the actual D^*, D, f, S_0, σ and the noise distribution.

8.2 Experimental work

8.2.1 Determination of the optimized set of b-values

The computation of the optimized set of b-values for a given set of parameters, $\boldsymbol{\theta} = \{S_0, D^*, D, f\}$, is achieved by minimizing the elements of the right hand side of the CRLB inequality (6.2).

The $\boldsymbol{I}^{-1}(\boldsymbol{b}, \boldsymbol{\theta})_{11}$ element of the inverse of the FIM of Eq. (8.2) corresponds to the CRLB of the S_0 ($\mathrm{CRLB}_{\mathrm{S_0}}$), the $\boldsymbol{I}^{-1}(\boldsymbol{b}, \boldsymbol{\theta})_{22}$ corresponds to the CRLB of the D ($\mathrm{CRLB}_{\mathrm{D}}$), the $\boldsymbol{I}^{-1}(\boldsymbol{b}, \boldsymbol{\theta})_{33}$ corresponds to the CRLB of the f ($\mathrm{CRLB}_{\mathrm{f}}$), and the $\boldsymbol{I}^{-1}(\boldsymbol{b}, \boldsymbol{\theta})_{44}$ corresponds to the CRLB of the D^* ($\mathrm{CRLB}_{\mathrm{D^*}}$). The off-diagonal elements of the inverse of the FIM correspond to the covariance between the different parameters (Karlsen et al., 1999). In order to obtain the optimized set of b-values that maximize the noise performance of the estimated IVIM parametric maps, we minimize the $\mathrm{CRLB}_{\mathrm{D}}$, $\mathrm{CRLB}_{\mathrm{f}}$ and the $\mathrm{CRLB}_{\mathrm{D^*}}$ separately, and jointly with the CRLB of the following figure of merit (CRLB_{Γ}):

$$\Gamma = \frac{\sqrt{\mathrm{CRLB}_{\mathrm{D}}}}{D} + \frac{\sqrt{\mathrm{CRLB}_{\mathrm{f}}}}{f} + \frac{\sqrt{\mathrm{CRLB}_{\mathrm{D^*}}}}{D^*}, \tag{8.3}$$

Thus, the optimized set of b-values is obtained through the minimization of the following four objective functions:

$$\hat{\boldsymbol{b}}_{\mathrm{D}} = \arg\min_{\boldsymbol{b}} \boldsymbol{I}^{-1}(\boldsymbol{b}, \boldsymbol{\theta})_{22} = \arg\min_{\boldsymbol{b}} \mathrm{CRLB}_{\mathrm{D}}(\boldsymbol{b}) \tag{8.4}$$

$$\hat{\boldsymbol{b}}_{\mathrm{f}} = \arg\min_{\boldsymbol{b}} \boldsymbol{I}^{-1}(\boldsymbol{b}, \boldsymbol{\theta})_{33} = \arg\min_{\boldsymbol{b}} \mathrm{CRLB}_{\mathrm{f}}(\boldsymbol{b}) \tag{8.5}$$

$$\hat{\boldsymbol{b}}_{\mathrm{D^*}} = \arg\min_{\boldsymbol{b}} \boldsymbol{I}^{-1}(\boldsymbol{b}, \boldsymbol{\theta})_{44} = \arg\min_{\boldsymbol{b}} \mathrm{CRLB}_{\mathrm{D^*}}(\boldsymbol{b}) \tag{8.6}$$

$$\hat{\boldsymbol{b}}_{\Gamma} = \arg\min_{\boldsymbol{b}} \mathrm{CRLB}_{\Gamma}(\boldsymbol{b}) \tag{8.7}$$

Previous minimization processes can be computationally expensive and even infeasible. Hence, based on the number of parameters of IVIM signal model of Eq. (8.1), we propose an iterative minimization method for the optimization of the optimal set of b-values from a large pool of N candidates:

Four b-value search: The optimized set of b-values is restricted to be composed of only four different b-values repeated k_0, k_1, k_2, and k_3 times, respectively. The first of them is fixed to be b = 0 s/mm^2 to have measurements with maximum Signal-to-Noise-Ratio (SNR), whereas the other three (low, middle, and high) are chosen among the pool of N-1 candidates (note that the previously chosen b-value is removed from the pool of candidates). Then, an exhaustive search is performed to find the optimized set of K b-values (k_0+k_1+k_2+k_3=K). Finally, the [zero(k_0), low(k_1), middle(k_2), high(k_3)] combination of the b-value set that achieves minimum $\mathrm{CRLB}_{\mathrm{D}}$, $\mathrm{CRLB}_{\mathrm{f}}$, $\mathrm{CRLB}_{\mathrm{D^*}}$, or CRLB_{Γ} is considered optimal.

Table 8.1: Parameters of interest used to obtain their CRLB-based b-value sets through all their combinations with the proposed four b-value search algorithm under the Rician noise assumption.

	Parameters for the computation of the CRLB-based b-value sets
D	[0.50, 0.70, 1.00, 2.00, 3.00, 4.00, 5.00, 6.00, 7.00] $\times 10^{-3}$ mm^2/s
f	[0.20, 0.30 0.40 0.50]
D^*	[20.00 30.00 40.00 50.00 60.00] $\times 10^{-3}$ mm^2/s
SNR	[200, 50, 10]

Hereinafter, the sets of b-values obtained using this CRLB-based analysis are called CRLB-based b-value sets. Table 8.1 shows the D, f, D^*, and SNR of the S_0 image used to obtain the CRLB-based b-value sets under the Rician noise assumption. Optimized sets were obtained for all K in the range of 4 to 34 and b-value pool of candidates was composed of N = 101 b-values uniformly distributed between o and 1000 s/mm^2.

8.2.2 Experimental data

In order to validate the proposed four b-value search method, we need to study whether this method is able to obtain the sets of b-values that effectively yield the lowest possible variance on the estimated IVIM parametric D, D^* and f maps. To that end, we compared the variance of the estimated maps with the CRLB-based optimized b-value sets and other sets proposed in the literature.

8.2.2.1 In-vivo liver IVIM

One healthy volunteer (female, 24 years old) was scanned with institutional review board approval and informed written consent. The acquisition was done with a 20-channel torso coil in a 3T scanner (Philips Healthcare, Best, The Netherlands). Axial diffusion-weighted images were acquired with respiratory triggering. Other acquisition parameters were: Field-of-View (FOV) = 22 × 20 cm, matrix size of 100 × 92, slice thickness of 7 mm, space between slices of 7 mm, Repetition Time (TR) = 2000 ms, Echo Time (TE) = 65.66 ms, and parallel imaging factor of 2. The N = 17 employed b-values were: [0, 25, 50, 75, 100, 125, 150, 175, 200, 250, 300, 400, 500, 600, 700, 850, 1000] s/mm^2. The whole acquisition was repeated 16 consecutive times to enable voxel-wise determination of the D, D^*, f and SNR statistics. No repetition was discarded due to steady-state effects.

SNR of the S_0 images was computed voxel-wise by calculating the ratio between the mean signal intensity and the standard deviation across the 16 repetitions considered. Ground truth D, D^* and f were obtained with a maximum likelihood estimator using all the diffusion-weighted images and b-values of the acquisition. For evaluation of SNR, D, D^*, and f, a 30 mm^2 Region of Interest (ROI) was drawn on each slice. In addition, another large ROI was drawn with full liver coverage. In both cases, ROIs, were co-localized across different acquisitions. Care

Table 8.2: Characterization of the liver IVIM DWI acquisition. Mean ground truth parametric map (± standard deviation), and mean SNR (± standard deviation) of the S_0 image. Ground truth parametric maps were computed from all DW images and b-values of the liver IVIM DWI acquisition.

	In-vivo liver IVIM DWI acquisition
D	$1.04 \pm 0.23 \times 10^{-3}$ mm^2/s
f	0.21 ± 0.05
D^*	$70.97 \pm 19.20 \times 10^{-3}$ mm^2/s
SNR	9.68 ± 8.60

was taken to avoid large vessels. All parametric maps were obtained to fully describe the liver acquisition used in the experiment. Mean SNR, mean ground truth D, D^*, and f values of the acquisition are shown in Table 8.2.

8.2.3 Experimental validation

Based on the previous acquisition, the following experiment is performed to prove the superiority (i.e., lower estimation variance) of the proposed CRLB-based b-value sets compared to sets of b-values proposed on the literature for liver IVIM DWI.

- Given a set of b-values, Diffusion-Weighted (DW) images of a DWI acquisition were selected for IVIM parametric maps estimation (D, D^* and f) with a Maximum Likelihood (ML) estimator. However, if a b-value was repeated on the selected set, an equivalent number of DW images of the consecutive repetitions were selected (it is to be noted that as described in Section 8.2.2.1, the whole DWI acquisition, with its 17 distinct b-values, was repeatedly acquired 16 consecutive times). Hence, this method was repeated 16 times, one for each acquisition, obtaining a total set of 16 different IVIM parametric maps. Then, we obtained the voxelwise standard deviation statistics of each parametric map (σ_{D}, σ_{D^*}, σ_{f}) across all the estimated maps. This experiment constitutes a procedure to experimentally compare the achieved noise performance (i.e., σ_{D}, σ_{D^*}, σ_{f}) of various b-value sets.

8.3 Results

8.3.1 b-Value optimization

The four b-value search algorithm obtained an optimized set of four b-values composed of k_0 b-values equal to 0 s/mm^2, and other three low, middle, and high b-values repeated k_1, k_2, and k_3 times, respectively, as shown in Figure 8.1. Figure 8.1 shows the distribution of the optimized CRLB-based $K = 13$ b-value sets of all parameter combinations of Table 8.1 grouped by zero (black), low

(green), middle (blue) and high (red) b-values. These were optimized by minimizing the four objective functions described in Eqs. (8.4) (minimizing $CRLB_D$), (8.5) (minimizing $CRLB_f$), (8.6) (minimizing $CRLB_{D^*}$), and (8.7) (minimizing $CRLB_\Gamma$) for an SNR level of 10. These distributions stablish that the low b-values should be approximately in the range of 10 - 60 s/mm^2, the middle b-values should be approximately in the range of 60 - 200 s/mm^2, and the high b-values should be approximately greater than $>$ 200 s/mm^2. For higher SNR under the Rician noise distribution assumption and for the Gaussian noise distribution assumption, the lower limit for the high b-values slightly increases (i.e., $>$ 250 s/mm^2 at SNR of 200) while the other ranges stay approximately similar.

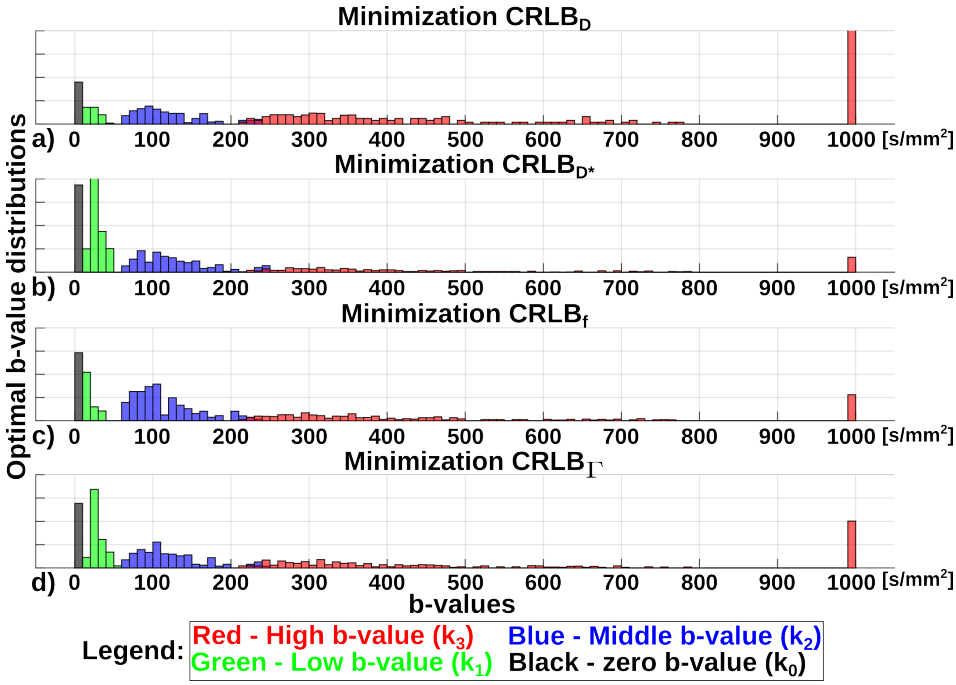

Figure 8.1: Distribution of the b-values of the optimal sets (K=13) obtained from parameters of Table 8.1 at SNR = 10 when minimizing $CRLB_D$ (a), $CRLB_{D^*}$ (b), $CRLB_f$ (c), and $CRLB_\Gamma$ (d). The color-code groups the b-values by zero, low, middle, and high b-values indicating that to minimize the estimation variance (i.e., maximize the noise performance) of the IVIM parameter maps, the low b-value should be in the range of 10-60s/mm^2, the middle b-value in the range of 60 - 200 s/mm^2, and the high b-value should be greater than $>$ 200 s/mm^2.

Figure 8.2 shows the ratio between the number of times each b-value is repeated (k_i, where i = 0, 1, 2, 3) in the optimized set and total number of b-values (K), when minimizing each of the four objective functions for the set of parameters D = 7 $\times$ 10^{-3}mm^2/s, f = 0.3, D^* = 20 $\times$ 10^{-3} mm^2/s, SNR values of 200, 50, and 10, and K from 4 to 34. The convergence limit of each ratio of each optimization is different, and they also vary for a different set of parameters. However, in most cases, at lower SNR there is a decrease of the times the high b-values are repeated

and an increase of the times the other three b-values are repeated on the optimized set, being the lower b-values always repeated less times than the higher b-values (i.e., $k_0 < k_1 < k_2 < k_3$).

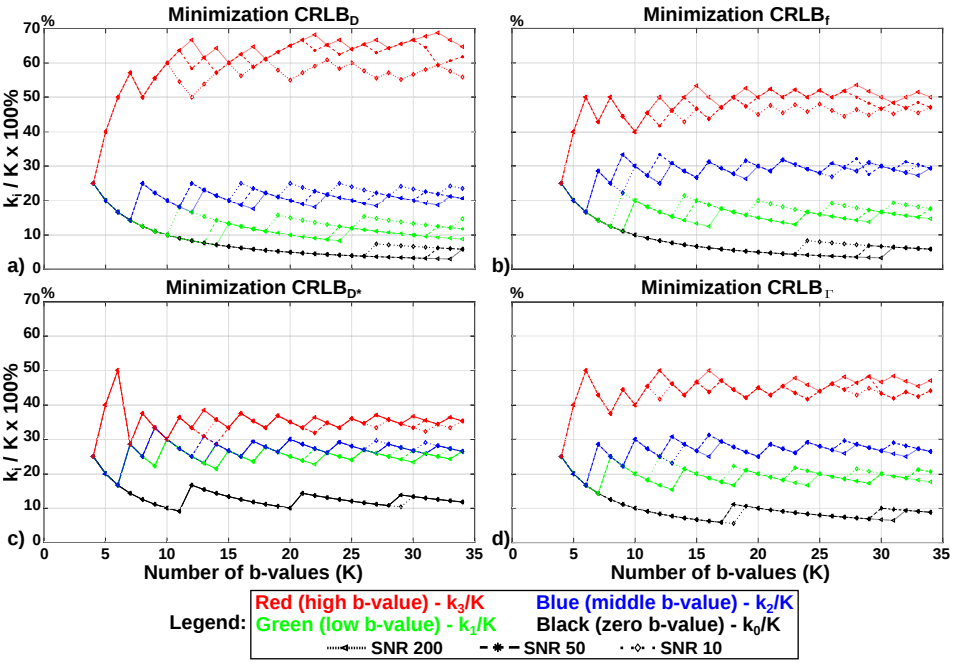

Figure 8.2: Ratio between the number of times each b-value is repeated (ki) on the optimal set and total number of b-values of the set (K), when minimizing CRLB_D (a), CRLB_f (b), CRLB_{D^*} (c), and CRLB_Γ (d) for SNR = [200, 50, 40]. Optimal b-value sets obtained for $D = 7$ x 10^{-3} mm^2/s, $f = 0.3$, $D^* = 20$ x 10^{-3} mm^2/s, SNR=[200, 50, 10], and K from 4 to 34. b-Value sets depend on the SNR, and the minimization (i.e., CRLB_D, CRLB_f, CRLB_{D^*}, and CRLB_Γ). Generally, at low SNR there is a decrease of the times the high b-value of the set is repeated and an increase of the times the other three b-values are repeated.

8.3.2 In-vivo liver IVIM experiments

Figure 8.3 shows the performance comparison in terms of the voxelwise standard deviation reduction (i.e., $\frac{\sigma_\text{D}-\sigma_\text{D-Rician}}{\sigma_\text{D}}$, $\frac{\sigma_{\text{D}^*}-\sigma_{\text{D}^*-\text{Rician}}}{\sigma_{\text{D}^*}}$, $\frac{\sigma_\text{f}-\sigma_\text{f-Rician}}{\sigma_\text{f}}$) between the proposed optimized CRLB-based b-value set obtained under the Rician noise assumption when minimizing the CRLB_Γ and the b-value sets proposed in the literature for in-vivo liver IVIM DWI. The proposed set of b-values and the sets found in the literature are described in Table 8.3. The σ_D, σ_{D^*}, and the σ_f were computed as described in the experimental validation Subsection 8.2.3. The proposed optimized CRLB-based b-value set achieves lower voxelwise standard deviation $\sigma_\text{D-Rician}$, $\sigma_{\text{D}^*-\text{Rician}}$, and $\sigma_\text{f-Rician}$ than any other set of the literature as shown in Figure 8.3.b)-d). Figure 8.3.e-g) further confirms that the standard

Table 8.3: Sets of b-values recommended on the literature for healthy in-vivo IVIM liver DWI.

	Manuscript	b-values (NEX*)
1)	Proposed optimized IVIM CRLB-based b-value set†	0(2) 25(4) 100(5) 1000(2)
2)	Lemke et al. (2011)‡	0(3) 50(1) 100(2) 175(1) 200(1) 250(1) 400(1) 600(1) 700(1) 1000(1)
3)	Koh et al. (2011)	0(1) 25(1) 50(1) 75(2) 100(2) 250(2) 500(2) 850(2‡)
4)	Luciani et al. (2008)	0(2) 25(2‡) 50(1) 75(1‡) 100(1) 200(2) 400(2) 850(2‡)

* b-Value sets are composed of $K = 13$ b-values. Therefore, the b-values recommended in the literature were repeated and shorted until a set of $K = 13$ was achieved. If K was not a multiple of the number of b-values proposed in the set, priority was given to the higher b-values as recommended by Padhani et al. (2009b).
† The proposed optimized IVIM CRLB-based b-value set was obtained by minimizing the CRLB_Γ.
‡ Some or all of these repeated b-values where rounded to allow IVIM parametric maps estimation with the b-values available in the current in-vivo liver DWI experiment.

deviation of the estimated IVIM parametric maps, and therefore the variance, of the proposed set of b-values is lower than in the other three literature cases. Particularly, boxplots of the σ_D, σ_{D^*}, and the σ_f have the lowest median with the narrowest Interquartile Range (IQR) as shown in Table 8.4. Namely, the σ_D reduction of the proposed set of b-values compared to the other literature sets is of 38.86%, 22.97% and 28.30%, the σ_{D^*} reduction is of 80.02%, 52.69% and 42.51%, and the σ_f reduction is of 62.50%, 57.14% and 62.50%, for each of the entries of Table 8.4. The values of the boxplots were taken from the corresponding slice of the full liver coverage ROI.

8.4 Discussion

In this chapter, we derived the Cramér-Rao Lower Bound (CRLB) of the biexponential Intravoxel Incoherent Motion (IVIM) diffusion-weighted model under a realistic noise assumption. This formulation provides an optimized set of b-values that maximize the noise performance (i.e., maximize the precision and minimize the variance) of IVIM parametric D, D^*, and f maps for liver IVIM DWI. Optimized CRLB-based b-value sets are composed of four groups of b-values. In our in-vivo liver IVIM DWI experiment with one healthy volunteer, the optimized set of b-values under the Rician noise distribution assumption estimated the IVIM parametric maps with lower variability than other state-of-the-art b-value sets. However, compared to the Gaussian distribution assumption, the optimized set of b-values is identical due to the IVIM set of parameters and the SNR of the acquisition. Note

Table 8.4: Median (Interquartile Range (IQR)) of the σ_{D}, σ_{D^*}, and the σ_{f} of each of the set of b-values of Table 8.3 on a representative slice of the liver. σ_{D}, σ_{D^*}, and the σ_{f} were computed as described in experiment the experimental validation Subsection 8.2.3. The values considered for the computation of the medians and the IQRs were taken from the corresponding slice of the full liver coverage ROI. It is to be noted that the variances of the IVIM parametric maps obtained by the proposed optimized IVIM CRLB-based b-value set under the Rician noise assumption achieves the lowest median with the lowest dispersion (i.e., lowest IQR).

	Manuscript	σ_{D}	σ_{D^*}	σ_{f}
		Median (IQR) [$\times 10^{-3}$ mm^2/s]		
1)	Proposed optimized IVIM CRLB-based b-value set	0.114 (0.08)	66.21 (0.18)	0.03 (0.02)
2)	Lemke et al. (2011)	0.175 (1.27)	331.44 (0.62)	0.08 (0.05)
3)	Koh et al. (2011)	0.148 (0.07)	139.96 (0.33)	0.07 (0.03)
4)	Luciani et al. (2008)	0.159 (0.09)	114.46 (0.37)	0.08 (0.04)

that in Figure 8.1, for an SNR of 10 under the Rician noise distribution assumption, the optimized b-value sets of many parameter configuration resulted in repeated high b-values at the maximum b-value of the pool of candidates (i.e., b-value of 1000 s/mm^2). Thus, in order to obtain different optimized b-value sets for higher SNR levels or for the Gaussian noise distribution assumption, a higher maximum b-value from the pool of candidates would have been required. Nevertheless, the maximum b-value we used was of 1000 s/mm^2 because it is commonly used in the literature (Dijkstra et al., 2012; Koh et al., 2011).

The proposed approach to optimize the set of b-values may be helpful to increase the quality of the estimated IVIM parametric D, f, and D^* maps, particularly in IVIM of the liver, where the estimation of the pseudodiffusion coefficient has very low precision (Taouli et al., 2016) under clinical viable times. Additionally, it may also help standardization of body IVIM DWI acquisitions, where the multiple methodologies (and even terminology) employed hinder its widespread application and complicate the comparison between studies.

Simulations show the optimized b-value set depends on the D, f, D^*, SNR and on the minimization objective function (minimization of $\mathrm{CRLB}_{\mathrm{D}}$, $\mathrm{CRLB}_{\mathrm{f}}$, $\mathrm{CRLB}_{\mathrm{D}^*}$ or CRLB_{Γ}). Further, the optimized b-values can be grouped as the color-coded representation of Figure 8.1, which groups the b-values in four clusters. The number of k_0 and k_1 of the zero and low b-value groups is higher for the minimization of the $\mathrm{CRLB}_{\mathrm{D}^*}$, the number of k_2 of the middle group is higher for the minimization of the $\mathrm{CRLB}_{\mathrm{f}}$, and the number of k_3 of the high b-value group is higher for the minimization of the $\mathrm{CRLB}_{\mathrm{D}}$. Correspondingly, the number k_0, k_1, k_2, and of k_3 for the minimization of the CRLB_{Γ} is a mixture of the previous three minimizations as shown in Figure 8.2. In general, the proposed optimized CRLB-based set of b-values achieves IVIM parametric maps with lower voxelwise standard deviation than various sets of b-values proposed in the literature for in-vivo liver IVIM DWI ((Koh et al., 2011; Lemke et al., 2011; Luciani et al., 2008)) as shown in Figure 8.3.

This work has several limitations. We need to have prior knowledge of the target set of D, f, D^* and scan SNR. Nevertheless, IVIM parameters are tissue specific and the SNR can be computed from initial pre-scans (Saritas et al., 2011; Xing et al., 1997). On the other hand, the clinical relevance of the proposed method could not be established, since only one acquisition of a healthy volunteer, with a limited set of b-values, was available. Thus, further validation is still required with both in-vivo healthy and diseased subjects, and a larger pool of b-values.

8.5 Conclusion

We have derived the Cramér-Rao Lower Bound (CRLB) of the Intravoxel Incoherent Motion (IVIM) biexponential diffusion-weighted model under a Rician distribution noise assumption, and proposed a formulation to obtain the optimized set of b-values that maximize the noise performance of the estimated IVIM parametric maps (D, D^*, and f). b-Value optimization is crucial to reduce the estimation variance (i.e., maximize precision and noise performance) of IVIM parameters. Thus, the proposed approach may help optimize and standardize IVIM liver Diffusion-Weighted Magnetic Resonance Imaging (DW-MRI) acquisitions.

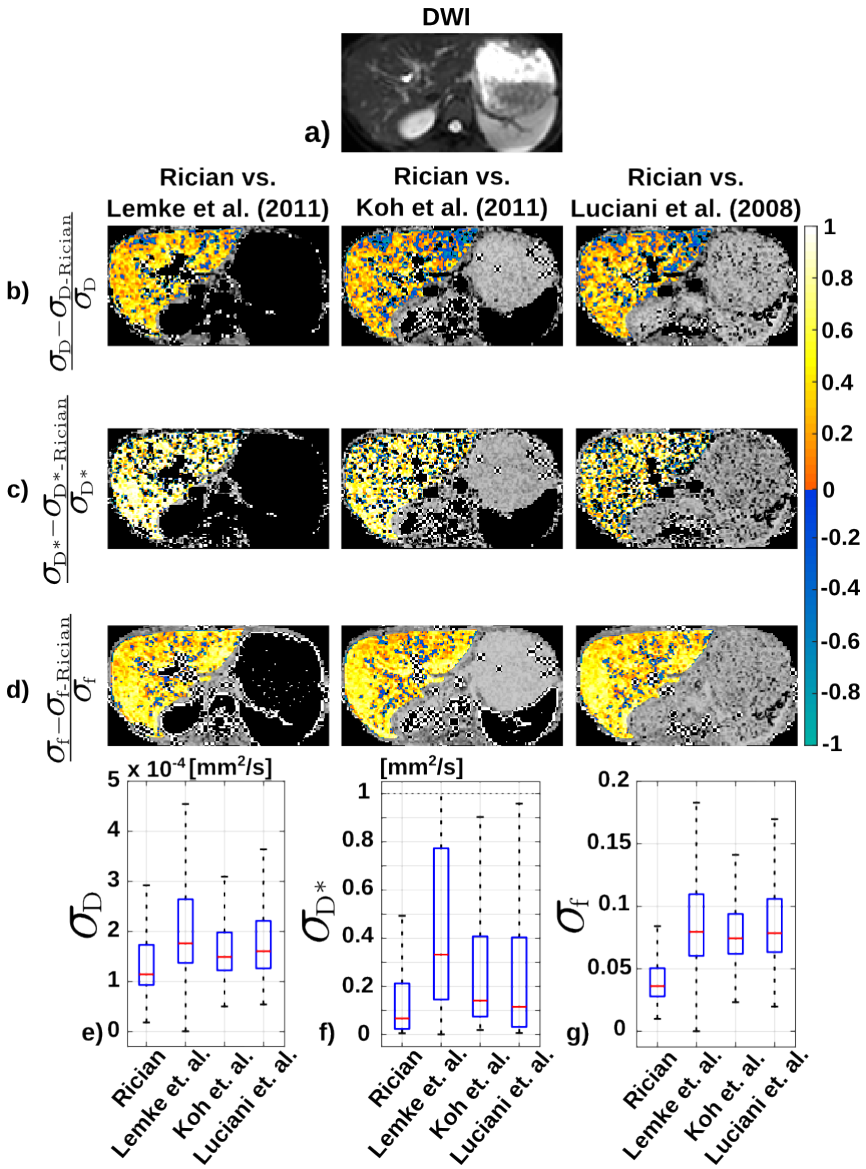

Figure 8.3: Performance comparison between the optimal b-value set obtained with the proposed approach minimizing the figure of merit (CRLB_Γ) and three sets of b-values found in the literature (see Table 2). (a) DWI with no weighting. (b-d) Voxel-wise standard deviation reductions for each of the estimated IVIM parameter maps. (e-g) Corresponding boxplots of the σ_D, σ_{D^*}, and σ_f of each b-value set on the corresponding slice of the liver. The proposed optimal b-value set achieves lower voxel-wise standard deviation on all estimated parameters than the literature sets.

Part IV

Backmatter

9

Conclusions, future work and contributions

Contents

9.1 Conclusions

DW-MRI was first introduced in the mid 80's as an imaging modality with poor quality due to its slowness and strong sensitivity to motion and other confounding factors. These drawbacks initially slowed down its utilization, but with the advancement of:

- Magnetic Resonance Imaging (MRI) hardware (i.e., the progress in gradient coils).
- Sequence acquisitions (i.e., rapid imaging techniques).
- Image postprocessing (i.e., reconstruction methods).
- Parameter estimation methods.

DW-MRI has gained considerable credit within the Magnetic Resonance (MR) community, and nowadays is an extensively used technique for diagnosis. Nevertheless, despite the multiple advances DWI, still remains technically challenging due to its multiple artefacts, limitations and pitfalls as shown in Section 2.4. Moreover, the

different MR scanners, acquisition sequences, and postprocessing and estimation methods introduce high variability to both the acquired images and the diffusion-related parametric maps, hindering their interpretation and the standardization of DWI. This Thesis dissertation addressed some of the issues concerning the optimization of the DWI acquisition sequence and estimation techniques of the diffusion-related parametric maps in order to grant viable quantitative imaging biomarkers computation.

A standard DWI sequence is based on a Spin Echo (SE) sequence in which powerful diffusion-weighting gradients have been introduced. These gradients, as well as making the sequence sensitive to Brownian motion, make it sensitive to physiological bulk motion (i.e., respiratory or cardiac motion), may introduce Eddy Currents (ECs) and Concomitant Gradients (CGs) artefacts and may stimulate peripheral nerves due to the large currents driven in the coils. Also, these gradients lengthen the DWI acquisition sequence (i.e., the TE) due to the hardware physical restrictions and the strong diffusion-weighting requirements. Note that nowadays the diffusion-weighting b-values can be up to several thousands [s/mm^2]. As a result, all these effects may contribute to undesired signal attenuation, may produce phase variations which could introduce image distortions and bias on the estimated diffusion-related parametric maps and may also cause patient discomfort. Consequently, there is an interest in designing diffusion-weighting gradients able to diminish the aforementioned artefacts, limitations and pitfalls. Thus, we have focused on comprehending the physical and physiological artefacts and limitations of DWI in whose origin the diffusion-weighting gradient waveforms take a key role in order to develop a formulation able to jointly diminish them through the witty design of such gradient waveforms. Thus, in Part II of this Thesis dissertation, with the objective of enhancing DW image quality and parametric map estimation, we have developed and validated a novel nonlinear formulation termed Optimized Diffusion-weighting Gradient Waveform Design (ODGD). It allows the design of optimized diffusion-weighting gradient waveforms based on the b-value formulation in which previous DWI artefacts and limitations can be directly reduced by adjusting the corresponding linear and/or nonlinear constraints. The proposed formulation has been proved to produce diffusion-weighting gradient waveforms that diminish bulk motion effects and null the Concomitant Gradient (CG) and Eddy Current (EC) effects while minimizing the TE of the diffusion-weighted acquisitions. Further, it has been shown to be implementable in MR scanners of two different vendors with different static magnetic field B_0 proving feasibility and reproducibility. Compared to the state-of-the-art waveforms, ODGD reduced or equalized the minimum TE for a given b-value while maintaining the waveform properties. The TE reduction is larger at higher b-values, k-space resolutions and high-order moment nulling. This TE reduction further translates into an SNR increase, which added to the motion compensation and the reduced image distortions provide the ODGD waveforms with outstanding capabilities for the application of DW-MRI in the clinical routine and the computation of quantitative imaging biomarkers.

The SE DWI sequence with monopolar diffusion-weighting gradient waveforms is presumably present in every MR scanner. The preparation of the DWI sequence

prior to the acquisition requires the selection of the TE, TR, diffusion-weightings, i.e., set of b-values, and other sequence parameters to be applied. However, the broad design flexibility of the DWI sequence introduces large variability in the set of b-values used for each target tissue among clinicians and scientists of different institutions. These variations complicate comparison between studies. In addition, the chosen set of b-values also affects the precision and the noise performance of the estimated diffusion-related parametric maps, which further complicates DWI interpretation. Consequently, there is an interest in standardizing DWI acquisitions by selecting the set of b-values that increase the noise performance of the estimated diffusion-related parametric maps. Thus, in Part III of this Thesis dissertation, with the objective of increasing the noise performance (i.e., increasing the precision and minimizing the variance) of the estimated diffusion-related parametric maps, we have developed and validated a formulation based on the CRLB and on the realistic Rician noise distribution assumption to optimize the set of b-values for a target tissue. These sets depends on its expected diffusion-related coefficient and the expected SNR of the DWI acquisition. The formulation has been developed for the two prevalent diffusion-weighting signal models in body DWI, namely, the monoexponential signal model and the IVIM biexponentical signal model. It is interesting to note that the optimized set of b-values tends to be composed of two groups of b-values for the estimation of the Apparent Diffusion Coefficient (ADC) of the monoexponential signal model, and of four groups for the estimation of the IVIM diffusion-related parameters. The location of these groups depends on the target SNR and on the diffusion parameters, but they will be closer together and closer the the 0 s/mm^2 b-value for lower SNR and larger diffusivities. The validity of the optimized set of b-values has been proven on two different in-vivo liver DWI acquisitions where the proposed optimized sets achieve higher or similar parametric maps precision than the state-of-the-art b-value sets. As a result, the proposed formulation for the optimization of the set of b-values might have important applications for the specialization and standardization of DWI as well as for the computation of quantitative diffusion-related imaging biomarkers.

9.2 Future work

Throughout this Thesis dissertation we have developed the ODGD formulation to increase image quality of the SE DWI sequence. With the proposed formulation, we have jointly tackled a number of artefacts and pitfalls common in liver DWI. However, the proposed formulation could still be extended to diminish other confounding factors such as the bright signal originating from blood vessels, as already tackled in our Zhang et al. (2019) continuation, the acoustic noise generated by the diffusion-weighting gradients or the power consumption of the MR scanner. Acoustic noise is generated by fast varying currents in the gradient coils, which generate Lorentz forces resulting in vibrations and acoustic noise. Particularly, each gradient coil has an specific acoustic response that depends on the frequency response function of the gradient. As such, acoustic noise could be limited or reduced by extending the ODGD formulation to design diffusion-weighting gradients to

have resonance frequencies on the minimums of the gradient frequency response function. The acoustic noise reduction may increase the usability of DWI in fetal imaging. On the other hand, the power consumption of the MR scan during the application of a DWI sequence is directly proportional to the current used to generate the diffusion-weighting gradient waveforms. As a result, reducing the strength of the gradients will inherently reduce power consumption. However, this straightforward reduction may create suboptimal diffusion-weighting gradient waveforms. Hence, power consumption could be limited or reduced by extending the ODGD formulation to design diffusion-weighting gradient waveforms with low energy consumption.

Importantly, we have aimed our attention at the optimization of the SE DWI sequence, but the proposed ODGD formulation could be adapted to optimize the diffusion-weighting gradient waveforms of other DWI sequences such as Twice Refocused Spin Echo (TRSE) or Stimulated Echo (STE). It could also be adapted to optimize the gradients of other imaging techniques such as the velocity encoding gradients of the flow and motion sensitive 4D Flow sequence. This extension may facilitate accurate control of the encoded phase shifts. Further, the ODGD formulation could also be extended to optimize any gradient used in MRI such as the imaging encoding gradients or the slice selection gradients, which might help reduce the scanning time of any MR sequence and increase their tolerance to artefacts. Finally, throughout the experiments of this Thesis dissertation the ODGD waveforms were pre-computed offline and then loaded into the MR scanner. However, in order to increase usability online implementation should be considered.

Another line of future work will be based on the applications of the proposed ODGD formulation. Despite having focused in this Thesis on liver DWI, the optimized waveforms could be applied to any target tissue. In particular it could be applied to those suffering from strong motion such as the heart or the fetus. In those, the application of the ODGD formulation may increase image quality by reducing motion-related artefacts and bias on the estimated ADC and Diffusion Tensor Imaging (DTI) maps. Additionally, the proposed formulation might achieve improvements on multi-shot DW-Echo Planar Imaging (EPI) due to the potential for reduced motion-induced phase variations across multiple shots.

Another significant future line of research will consist on the extension of the CRLB formulation for the optimization of the set of b-values of DWI. We have focused our attention on the traditional monoexponential diffusion-weighting signal model and the biexponential IVIM diffusion-weighting signal model. Nevertheless, the Kurtosis and the Stretched Exponential diffusion-weighting signal models are gaining popularity in liver DWI. These extensions would require the derivation of the CRLB of the corresponding model under a realistic noise assumption and the subsequent development of a formulation for the computation of the optimized set of b-values. Similarly, the derivation of the CRLB and the corresponding optimized set of b-values of the diffusion-weighting signal models for a joint estimation of the T_2 map and the corresponding diffusion-related parametric maps may be critical for their precise estimation in multiparametric MRI. It would also be of interest to extend the formulation to obtain the optimal set of b-values for heterogeneous

tissues or tissues where focal lesions are present. Nevertheless, the extension of the CRLB formulation to optimize sets of b-values under the assumption of DW images affected by more complex noise distributions (i.e., the non-central chi noise distribution present in the composite images of Generalized Autocalibrating Partially Parallel Acquisition (GRAPPA) acquisitions) might not be needed. This lack of necessity comes from the few expected differences we hypothesize may arise compared to the Rician noise distribution assumption.

We have studied the precision of the estimated diffusion-related parametric maps, but accuracy, repeatability and precision should be studied together in order to establish quantitative imaging biomarkers, specially for complex diffusion-weighting signal models. Also, in many cases radiologists base their diagnosis on the contrast between tissues, thus, the contrast-to-noise-ratio needs additional attention. Finally, the optimized set of b-values needs further research within more acquisitions both on healthy and diseased subjects, as well as within more target tissues in order to be able to obtain clinical viable conclusions.

Last unequivocal future line of research consists in the acquisition of DW images of the optimized set of b-values proposed by the CRLB-based approaches whose diffusion-weighting gradients have been designed with the proposed ODGD formulation. The joint application of both methods may increase DW image quality and increase the accuracy of the estimated diffusion-related parametric maps paving the way towards the development of quantitative diffusion imaging biomarkers and speeding the awaited standardization of DW-MRI.

9.3 Contributions

In this Thesis dissertation we have focused on the optimization of liver DWI acquisition sequence and estimation techniques to increase image quality and the precision of the estimated diffusion-related parametric maps.

The main scientific contributions are listed next:

1. Development of a formulation for the design of optimized diffusion-weighting gradient waveforms of the SE DWI sequence to increase DW image quality. The optimized diffusion-weighting gradient waveforms maximize the SNR of the acquisition by minimizing the TE of a given b-value, the bulk motion-related artefacts, CGs dephasing effects, ECs induced distortions and the Peripheral Nerve Stimulation (PNS).

2. Derivation of the CRLB of the monoexponential DWI signal model under a realistic noise assumption and development of a formulation for the determination of the optimized set of b-values that maximize the noise performance (i.e., minimize the variance and maximize the precision) of the estimated ADC maps.

3. Derivation of the CRLB of the biexponential IVIM signal model under a realistic noise assumption and development of a formulation for the determi-

nation of the optimized set of b-values that maximize the noise performance (i.e., minimize the variance and maximize the precision) of the estimated IVIM parametric diffusion, pseudodiffusion and perfusion fraction maps.

Bibliography

Abart, J., Eberhardt, K., Fischer, H., Huk, W., Richter, E., Storch, T., Zeitler, E., et al., 1997. Peripheral nerve stimulation by time-varying magnetic fields. Journal of Computer Assisted Tomography 21 (4), 532–538.

Adrion, W. R., 1993. Research methodology in software engineering. In: Summary of the Dagstuhl Workshop on Future Directions in Software Engineering" Ed. Tichy, Habermann, and Prechelt, ACM Software Engineering Notes, SIGSoft. Vol. 18. pp. 36–37.

Aja-Fernández, S., Pie, T., Vegas-Sánchez-Ferrero, G., et al., 2015. Spatially variant noise estimation in MRI: A homomorphic approach. Medical Image Analysis 20 (1), 184–197.

Aja-Fernández, S., Vegas-Sánchez-Ferrero, G., 2016. Statistical Analysis of Noise in MRI. Modeling, Filtering and Estimation. Springer International Publishing.

Alberich-Bayarri, A., Sanz-Requena, R., García-Martí, G., Martí-Bonmatí, L., et al., 2014. Optimisation of b-values in MR diffusion-weighted acquisitions through information theory: a mathematical justification for consensus. In: European Congress of Radiology 2014. European Society of Radiology, pp. B–0580.

Alexander, A. L., Tsuruda, J. S., Parker, D. L., 1997. Elimination of eddy current artifacts in diffusion-weighted echo-planar images: the use of bipolar gradients. Magnetic Resonance in Medicine 38 (6), 1016–1021.

Alexander, D. C., 2008. A general framework for experiment design in diffusion MRI and its application in measuring direct tissue-microstructure features. Magnetic Resonance in Medicine 60 (2), 439–448.

Aliotta, E., Moulin, K., Ennis, D. B., 2018. Eddy current–nulled convex optimized diffusion encoding (EN-CODE) for distortion-free diffusion tensor imaging with short echo times. Magnetic Resonance in Medicine 79 (2), 663–672.

Aliotta, E., Wu, H. H., Ennis, D. B., 2017. Convex optimized diffusion encoding (CODE) gradient waveforms for minimum echo time and bulk motion–compensated diffusion-weighted MRI. Magnetic Resonance in Medicine 77 (2), 717–729.

Anderson, A. W., Gore, J. C., 1994. Analysis and correction of motion artifacts in diffusion weighted imaging. Magnetic Resonance in Medicine 32 (3), 379–387.

Bammer, R., Markl, M., Barnett, A., Acar, B., Alley, M., Pelc, N., Glover, G., Moseley, M., 2003. Analysis and generalized correction of the effect of spatial gradient field distortions in diffusion-weighted imaging. Magnetic Resonance in Medicine 50 (3), 560–569.

Barbieri, S., Donati, O. F., Froehlich, J. M., Thoeny, H. C., 2016. Impact of the calculation algorithm on biexponential fitting of diffusion-weighted MRI in upper abdominal organs. Magnetic Resonance in Medicine 75 (5), 2175–2184.

Baron, C., Lebel, R., Wilman, A., Beaulieu, C., 2012. The effect of concomitant gradient fields on diffusion tensor imaging. Magnetic Resonance in Medicine 68 (4), 1190–1201.

Bennett, K. M., Schmainda, K. M., Bennett, R., Rowe, D. B., Lu, H., Hyde, J. S., 2003. Characterization of continuously distributed cortical water diffusion rates with a stretched-exponential model. Magnetic Resonance in Medicine 50 (4), 727–734.

Bernstein, M. A., King, K. F., Zhou, X. J., 2004. Handbook of MRI pulse sequences. Elsevier.

Bernstein, M. A., Zhou, X. J., Polzin, J. A., King, K. F., Ganin, A., Pelc, N. J., Glover, G. H., 1998. Concomitant gradient terms in phase contrast MR: analysis and correction. Magnetic Resonance in Medicine 39 (2), 300–308.

Birenbaum, D., Bancroft, L. W., Felsberg, G. J., 2011. Imaging in acute stroke. Western Journal of Emergency Medicine 12 (1), 67.

Blaimer, M., Breuer, F., Mueller, M., Heidemann, R. M., Griswold, M. A., Jakob, P. M., 2004. SMASH, SENSE, PILS, GRAPPA: how to choose the optimal method. Topics in Magnetic Resonance Imaging 15 (4), 223–236.

Bloch, F., 1946. Nuclear induction. Physical Review 70 (7-8), 460.

Brihuega-Moreno, O., Heese, F. P., Hall, L. D., 2003. Optimization of diffusion measurements using Cramer-Rao lower bound theory and its application to articular cartilage. Magnetic Resonance in Medicine 50 (5), 1069–1076.

Bruegel, M., Gaa, J., Waldt, S., Woertler, K., Holzapfel, K., Kiefer, B., Rummeny, E. J., 2008a. Diagnosis of hepatic metastasis: comparison of respiration-triggered diffusion-weighted echo-planar MRI and five T2-weighted turbo spin-echo sequences. American Journal of Roentgenology 191 (5), 1421–1429.

Bruegel, M., Holzapfel, K., Gaa, J., Woertler, K., Waldt, S., Kiefer, B., Stemmer, A., Ganter, C., Rummeny, E. J., 2008b. Characterization of focal liver lesions by ADC measurements using a respiratory triggered diffusion-weighted single-shot echo-planar MR imaging technique. European Radiology 18 (3), 477–485.

Buckler, A. J., Bresolin, L., Dunnick, N. R., Sullivan, D. C., Group, 2011. Quantitative imaging test approval and biomarker qualification: interrelated but distinct activities. Radiology 259 (3), 875–884.

Carr, H. Y., Purcell, E. M., 1954. Effects of diffusion on free precession in nuclear magnetic resonance experiments. Physical Review 94 (3), 630.

Chen, N.-k., Guidon, A., Chang, H.-C., Song, A. W., 2013. A robust multi-shot scan strategy for high-resolution diffusion weighted MRI enabled by multiplexed sensitivity-encoding (MUSE). Neuroimage 72, 41–47.

Chow, A. M., Gao, D. S., Fan, S. J., Qiao, Z., Lee, F. Y., Yang, J., Man, K., Wu, E. X., 2012. Liver fibrosis: an intravoxel incoherent motion (IVIM) study. Journal of Magnetic Resonance Imaging 36 (1), 159–167.

Cohen, J., 2013. Statistical power analysis for the behavioral sciences. Routledge.

Colagrande, S., Pasquinelli, F., Mazzoni, L. N., Belli, G., Virgili, G., 2010. MR-diffusion weighted imaging of healthy liver parenchyma: Repeatability and reproducibility of apparent diffusion coefficient measurement. Journal of Magnetic Resonance Imaging 31 (4), 912–920.

Constantinides, C. D., Atalar, E., McVeigh, E. R., 1997. Signal-to-noise measurements in magnitude images from NMR phased arrays. Magnetic Resonance in Medicine 38 (5), 852–857.

Den Boer, J., Bakker, R., Ham, C., Smink, J., 1999. Generalization to complex stimulus shape of the nerve stimulation threshold based on existing knowledge of its relation to stimulus duration for rectangular stimuli. In: Proceedings of the International Sociecty of Magnetic Resonace in Medicine. Vol. 7. International Society of Magnetic Resonance in Medicine, p. 108.

Den Boer, J. A., Bourland, J. D., Nyenhuis, J. A., Ham, C. L., Engels, J. M., Hebrank, F. X., Frese, G., Schaefer, D. J., 2002. Comparison of the threshold for peripheral nerve stimulation during gradient switching in whole body MR systems. Journal of Magnetic Resonance Imaging 15 (5), 520–525.

DeVore, M. D., Lanterman, A. D., O Sullivan, J. A., 2000. ATR performance of a Rician model for SAR images. In: Proceedings of the SPIE - The International Society for Optical Engineering. International Society for Optical Engineering, pp. 34–47.

Dijkstra, H., Baron, P., Kappert, P., Oudkerk, M., Sijens, P. E., 2012. Effects of microperfusion in hepatic diffusion weighted imaging. European Radiology 22 (4), 891–899.

Dolui, S., Kuurstra, A., Michailovich, O. V., 2012. Rician compressed sensing for fast and stable signal reconstruction in diffusion MRI. In: Medical Imaging 2012: Image Processing. Vol. 8314. International Society for Optics and Photonics, p. 83144Q.

Feldman, R. E., Hardy, C. J., Aksel, B., Schenck, J., Chronik, B. A., 2009. Experimental determination of human peripheral nerve stimulation thresholds in a 3-axis planar gradient system. Magnetic Resonance in Medicine 62 (3), 763–770.

Finsterbusch, J., 2009. Eddy-current compensated diffusion weighting with a single refocusing RF pulse. Magnetic Resonance in Medicine 61 (3), 748–754.

Finsterbusch, J., 2010. Double-spin-echo diffusion weighting with a modified eddy current adjustment. Magnetic Resonance Imaging 28 (3), 434–440.

Fleysher, R., Fleysher, L., Gonen, O., 2008. The optimal MR acquisition strategy for exponential decay constants estimation. Magnetic Resonance Imaging 26 (3), 433–435.

Geethanath, S., Vaughan Jr, J. T., 2019. Accessible magnetic resonance imaging: a review. Journal of Magnetic Resonance Imaging 49 (7), e65–e77.

Glass, R. L., 1995. A structure-based critique of contemporary computing research. Journal of Systems and Software 28 (1), 3–7.

Glover, P., 2009. Interaction of MRI field gradients with the human body. Physics in Medicine & Biology 54 (21), R99.

Goshima, S., Kanematsu, M., Kondo, H., Yokoyama, R., Kajita, K., Tsuge, Y., Watanabe, H., Shiratori, Y., Onozuka, M., Moriyama, N., 2008. Diffusion-weighted imaging of the liver: optimizing b value for the detection and characterization of benign and malignant hepatic lesions. Journal of Magnetic Resonance Imaging 28 (3), 691–697.

Gourtsoyianni, S., Papanikolaou, N., Yarmenitis, S., Maris, T., Karantanas, A., Gourtsoyiannis, N., 2008. Respiratory gated diffusion-weighted imaging of the liver: value of apparent diffusion coefficient measurements in the differentiation between most commonly encountered benign and malignant focal liver lesions. European Radiology 18 (3), 486–492.

Griswold, M. A., Jakob, P. M., Heidemann, R. M., Nittka, M., Jellus, V., Wang, J., Kiefer, B., Haase, A., 2002. Generalized autocalibrating partially parallel acquisitions (GRAPPA). Magnetic Resonance in Medicine 47 (6), 1202–1210.

Guiu, B., Cercueil, J.-P., 2011. Liver diffusion-weighted MR imaging: the tower of Babel? European Radiology 21 (3), 463–467.

Güllmar, D., Haueisen, J., Reichenbach, J. R., 2005. Analysis of b-value calculations in diffusion weighted and diffusion tensor imaging. Concepts in Magnetic Resonance Part A 25 (1), 53–66.

Guo, Y., Cai, Y.-Q., Cai, Z.-L., Gao, Y.-G., An, N.-Y., Ma, L., Mahankali, S., Gao, J.-H., 2002. Differentiation of clinically benign and malignant breast lesions using diffusion-weighted imaging. Journal of Magnetic Resonance Imaging 16 (2), 172–178.

Haider, M. A., Van Der Kwast, T. H., Tanguay, J., Evans, A. J., Hashmi, A.-T., Lockwood, G., Trachtenberg, J., 2007. Combined T2-weighted and diffusion-weighted MRI for localization of prostate cancer. American Journal of Roentgenology 189 (2), 323–328.

Ham, C., Engels, J., Van de Wiel, G., Machielsen, A., 1997. Peripheral nerve stimulation during MRI: effects of high gradient amplitudes and switching rates. Journal of Magnetic Resonance Imaging 7 (5), 933–937.

Hamilton, G., Middleton, M. S., Hooker, J. C., Haufe, W. M., Forbang, N. I., Allison, M. A., Loomba, R., Sirlin, C. B., 2015. In vivo breath-hold 1H MRS simultaneous estimation of liver proton density fat fraction, and T1 and T2 of water and fat, with a multi-TR, multi-TE sequence. Journal of Magnetic Resonance Imaging 42 (6), 1538–1543.

Hanson, L. G., 2008. Is quantum mechanics necessary for understanding magnetic resonance? Concepts in Magnetic Resonance Part A 32 (5), 329–340.

Harvey, P. R., Mansfield, P., 1994. Avoiding peripheral nerve stimulation: gradient waveform criteria for optimum resolution in echo-planar imaging. Magnetic Resonance in Medicine 32 (2), 236–241.

Haselgrove, J. C., Moore, J. R., 1996. Correction for distortion of echo-planar images used to calculate the apparent diffusion coefficient. Magnetic Resonance in Medicine 36 (6), 960–964.

Herrmann, C., Annekristin, R., 2012. Magnetic resonance equipment (MRI)-study on the potential for environmental improvement by the aspect of energy efficiency. PE INTERNATIONAL AG, Report.

Herrmann, J., Schoennagel, B. P., Roesch, M., Busch, J. D., Derlin, T., Doh, L. K., Petersen, K. U., Graessner, J., Adam, G., Habermann, C. R., 2013. Diffusion-weighted imaging of the healthy pancreas: ADC values are age and gender dependent. Journal of Magnetic Resonance Imaging 37 (4), 886–891.

Hidalgo-Tobon, S., 2010. Theory of gradient coil design methods for magnetic resonance imaging. Concepts in Magnetic Resonance Part A 36 (4), 223–242.

Holdsworth, S. J., Skare, S., Newbould, R. D., Guzmann, R., Blevins, N. H., Bammer, R., 2008. Readout-segmented EPI for rapid high resolution diffusion imaging at 3T. European Journal of Radiology 65 (1), 36–46.

Hoult, D., Lauterbur, P. C., 1979. The sensitivity of the zeugmatographic experiment involving human samples. Journal of Magnetic Resonance 34 (2), 425–433.

Hutter, J., Price, A. N., Cordero-Grande, L., Malik, S., Ferrazzi, G., Gaspar, A., Hughes, E. J., Christiaens, D., McCabe, L., Schneider, T., et al., 2018. Quiet echo planar imaging for functional and diffusion MRI. Magnetic Resonance in Medicine 79 (3), 1447–1459.

Imaging, B., 1997. 150028 USA Instruments INC. SNR Phantom for GE MRI. https://parts.blockimaging.com/150028-USA-Instruments--INC.-SNR-Phantom-for-GE-MRI-for-GE--Closed-MRI/, [Online; accessed 07-January-2018].

Jalnefjord, O., Montelius, M., Starck, G., Ljungberg, M., 2019. Optimization of b-value schemes for estimation of the diffusion coefficient and the perfusion fraction with segmented intravoxel incoherent motion model fitting. Magnetic Resonance in Medicine 82 (4), 1541–1552.

Jambor, I., Merisaari, H., Aronen, H. J., Järvinen, J., Saunavaara, J., Kauko, T., Borra, R., Pesola, M., 2014. Optimization of b-value distribution for biexponential diffusion-weighted MR imaging of normal prostate. Journal of Magnetic Resonance Imaging 39 (5), 1213–1222.

Janke, A., Zhao, H., Cowin, G. J., Galloway, G. J., Doddrell, D. M., 2004. Use of spherical harmonic deconvolution methods to compensate for nonlinear gradient effects on MRI images. Magnetic Resonance in Medicine 52 (1), 115–122.

Jensen, J. H., Helpern, J. A., Ramani, A., Lu, H., Kaczynski, K., 2005. Diffusional kurtosis imaging: the quantification of non-gaussian water diffusion by means of magnetic resonance imaging. Magnetic Resonance in Medicine 53 (6), 1432–1440.

Jeong, W. K., Jamshidi, N., Felker, E. R., Raman, S. S., Lu, D. S., 2019. Radiomics and radiogenomics of primary liver cancers. Clinical and Molecular Hepatology 25 (1), 21.

Jezzard, P., Barnett, A. S., Pierpaoli, C., 1998. Characterization of and correction for eddy current artifacts in echo planar diffusion imaging. Magnetic Resonance in Medicine 39 (5), 801–812.

Jones, D. K., Alexander, D. C., Bowtell, R., Cercignani, M., Dell'Acqua, F., McHugh, D. J., Miller, K. L., Palombo, M., Parker, G. J., Rudrapatna, U., et al., 2018. Microstructural imaging of the human brain with a 'super-scanner': 10 key advantages of ultra-strong gradients for diffusion mri. NeuroImage 182, 8–38.

Jones, D. K., Horsfield, M. A., Simmons, A., 1999. Optimal strategies for measuring diffusion in anisotropic systems by magnetic resonance imaging. Magnetic Resonance in Medicine 42 (3), 515–525.

Karlsen, O. T., Verhagen, R., Bovee, W. M., 1999. Parameter estimation from Rician-distributed data sets using a maximum likelihood estimator: Application to T1 and perfusion measurements. Magnetic Resonance in Medicine 41 (3), 614–623.

Kay, S. M., 1993. Fundamentals of statistical signal processing. Prentice Hall PTR.

Kaya, B., Koc, Z., 2014. Diffusion-weighted MRI and optimal b-value for characterization of liver lesions. Acta Radiologica 55 (5), 532–542.

Kim, T., Murakami, T., Takahashi, S., Hori, M., Tsuda, K., Nakamura, H., 1999. Diffusion-weighted single-shot echoplanar MR imaging for liver disease. American Journal of Roentgenology 173 (2), 393–398.

Kingsley, P. B., Monahan, W. G., 2004. Selection of the optimum b factor for diffusion-weighted magnetic resonance imaging assessment of ischemic stroke. Magnetic Resonance in Medicine 51 (5), 996–1001.

Koay, C. G., Özarslan, E., Basser, P. J., 2009. A signal transformational framework for breaking the noise floor and its applications in MRI. Journal of Magnetic Resonance 197 (2), 108–119.

Koc, Z., Erbay, G., 2014. Optimal b Value in Diffusion-Weighted Imaging for Differentiation of Abdominal Lesions. Journal of Magnetic Resonance Imaging 40 (3), 559–566.

Koch, M., Norris, D. G., 2000. An assessment of eddy current sensitivity and correction in single-shot diffusion-weighted imaging. Physics in Medicine & Biology 45 (12), 3821.

Koh, D.-M., Collins, D. J., 2007. Diffusion-weighted MRI in the body: applications and challenges in oncology. American Journal of Roentgenology 188 (6), 1622–1635.

Koh, D.-M., Collins, D. J., Orton, M. R., 2011. Intravoxel incoherent motion in body diffusion-weighted MRI: reality and challenges. American Journal of Roentgenology 196 (6), 1351–1361.

Koh, D.-M., Thoeny, H. C., 2010. Diffusion-weighted MR imaging: applications in the body. Springer Science & Business Media.

Lauterbur, P. C., 1973. Image formation by induced local interactions: examples employing nuclear magnetic resonance. nature 242 (5394), 190–191.

Le Bihan, D., 2007a. Le Bihan, Denis: Diffusion MRI: A Historical Account. eMagRes.

Le Bihan, D., 2007b. The 'wet mind': water and functional neuroimaging. Physics in Medicine and Biology 52 (7), R57.

Le Bihan, D., 2013. Apparent diffusion coefficient and beyond: what diffusion MR imaging can tell us about tissue structure.

Le Bihan, D., Breton, E., 1985. Imagerie de diffusion in vivo par résonance magnétique nucléaire. Comptes rendus de l'Académie des sciences. Série 2, Mécanique, Physique, Chimie, Sciences de l'univers, Sciences de la Terre 301 (15), 1109–1112.

Le Bihan, D., Breton, E., Lallemand, D., Aubin, M., Vignaud, J., Laval-Jeantet, M., 1988. Separation of diffusion and perfusion in intravoxel incoherent motion MR imaging. Radiology 168 (2), 497–505.

Le Bihan, D., Breton, E., Lallemand, D., Grenier, P., Cabanis, E., Laval-Jeantet, M., 1986. MR imaging of intravoxel incoherent motions: application to diffusion and perfusion in neurologic disorders. Radiology 161 (2), 401–407.

Le Bihan, D., Poupon, C., Amadon, A., Lethimonnier, F., 2006. Artifacts and pitfalls in diffusion MRI. Journal of Magnetic Resonance Imaging 24 (3), 478–488.

Le Bihan, D., Turner, R., Moonen, C. T., Pekar, J., 1991. Imaging of diffusion and microcirculation with gradient sensitization: design, strategy, and significance. Journal of Magnetic Resonance Imaging 1 (1), 7–28.

Lee, S. S., Byun, J. H., Park, B. J., Park, S. H., Kim, N., Park, B., Kim, J. K., Lee, M.-G., 2008. Quantitative analysis of diffusion-weighted magnetic resonance imaging of the pancreas: usefulness in characterizing solid pancreatic masses. Journal of Magnetic Resonance Imaging 28 (4), 928–936.

Lemke, A., Stieltjes, B., Schad, L. R., Laun, F. B., 2011. Toward an optimal distribution of b values for intravoxel incoherent motion imaging. Magnetic Resonance Imaging 29 (6), 766–776.

Leporq, B., Saint-Jalmes, H., Rabrait, C., Pilleul, F., Guillaud, O., Dumortier, J., Scoazec, J.-Y., Beuf, O., 2015. Optimization of intra-voxel incoherent motion imaging at 3.0 Tesla for fast liver examination. Journal of Magnetic Resonance Imaging 41 (5), 1209–1217.

Lewin, M., Poujol-Robert, A., Boëlle, P.-Y., Wendum, D., Lasnier, E., Viallon, M., Guéchot, J., Hoeffel, C., Arrivé, L., Tubiana, J.-M., et al., 2007. Diffusion-weighted magnetic resonance imaging for the assessment of fibrosis in chronic hepatitis c. Hepatology 46 (3), 658–665.

Liau, J., Lee, J., Schroeder, M. E., Sirlin, C. B., Bydder, M., 2012. Cardiac motion in diffusion-weighted MRI of the liver: artifact and a method of correction. Journal of Magnetic Resonance Imaging 35 (2), 318–327.

Luciani, A., Vignaud, A., Cavet, M., Tran Van Nhieu, J., Mallat, A., Ruel, L., Laurent, A., Deux, J.-F., Brugieres, P., Rahmouni, A., 2008. Liver cirrhosis: intravoxel incoherent motion MR imaging—pilot study. Radiology 249 (3), 891–899.

Luna, A., Martín, T., González, J. S., 2012. Diffusion-weighted imaging in the evaluation of lung, mediastinum, heart, and chest wall. In: Diffusion MRI Outside the Brain. Springer, pp. 279–306.

Ma, D., Gulani, V., Seiberlich, N., Liu, K., Sunshine, J. L., Duerk, J. L., Griswold, M. A., 2013. Magnetic resonance fingerprinting. Nature 495 (7440), 187–192.

Malyarenko, D. I., Ross, B. D., Chenevert, T. L., 2014. Analysis and correction of gradient nonlinearity bias in apparent diffusion coefficient measurements. Magnetic Resonance in Medicine 71 (3), 1312–1323.

Mansfield, P., 1977. Multi-planar image formation using NMR spin echoes. Journal of Physics C: Solid State Physics 10 (3), L55.

Mansfield, P., Grannell, P. K., 1973. NMR'diffraction'in solids? Journal of Physics C: Solid State Physics 6 (22), L422.

Matoba, M., Tonami, H., Kondou, T., Yokota, H., Higashi, K., Toga, H., Sakuma, T., 2007. Lung carcinoma: diffusion-weighted MR imaging—preliminary evaluation with apparent diffusion coefficient. Radiology 243 (2), 570–577.

McKenzie, C. A., Yeh, E. N., Ohliger, M. A., Price, M. D., Sodickson, D. K., 2002. Self-calibrating parallel imaging with automatic coil sensitivity extraction. Magnetic Resonance in Medicine 47 (3), 529–538.

Meier, C., Zwanger, M., Feiweier, T., Porter, D., 2008. Concomitant field terms for

asymmetric gradient coils: Consequences for diffusion, flow, and echo-planar imaging. Magnetic Resonance in Medicine 60 (1), 128–134.

Merisaari, H., Jambor, I., 2015. Optimization of b-value distribution for four mathematical models of prostate cancer diffusion-weighted imaging using b-values up to 2000 s/mm2: Simulation and repeatability study. Magnetic Resonance in Medicine 73 (5), 1954–1969.

Michailovich, O., Rathi, Y., Dolui, S., 2011. Spatially regularized compressed sensing for high angular resolution diffusion imaging. IEEE Transactions on Medical Imaging 30 (5), 1100–1115.

Moseley, M., Kucharczyk, J., Mintorovitch, J., Cohen, Y., Kurhanewicz, J., Derugin, N., Asgari, H., Norman, D., 1990. Diffusion-weighted MR imaging of acute stroke: correlation with T2-weighted and magnetic susceptibility-enhanced MR imaging in cats. American Journal of Neuroradiology 11 (3), 423–429.

Moya-Sáez, E., Peña-Nogales, Ó., Sanz-Estébanez, S., de Luis-Garcia, R., Alberola-López, C., 2020. CNN-based synthesis of T1, T2 and PD parametric maps of the brain with a minimal input feeding. In: Proceedings of the International Sociecty of Magnetic Resonace in Medicine. International Society of Magnetic Resonance in Medicine, p. 3806.

Murphy, P., Wolfson, T., Gamst, A., Sirlin, C., Bydder, M., 2013. Error model for reduction of cardiac and respiratory motion effects in quantitative liver DW-MRI. Magnetic Resonance in Medicine 70 (5), 1460–1469.

Murtz, P., Flacke, S., Traber, F., van den Brink, J. S., Gieseke, J., Schild, H. H., 2002. Abdomen: diffusion-weighted MR imaging with pulse-triggered single-shot sequences. Radiology 224 (1), 258–264.

Namimoto, T., Yamashita, Y., Sumi, S., Tang, Y., Takahashi, M., 1997. Focal liver masses: characterization with diffusion-weighted echo-planar MR imaging. Radiology 204 (3), 739–744.

Nomori, H., Mori, T., Ikeda, K., Kawanaka, K., Shiraishi, S., Katahira, K., Yamashita, Y., 2008. Diffusion-weighted magnetic resonance imaging can be used in place of positron emission tomography for N staging of non–small cell lung cancer with fewer false-positive results. The Journal of Thoracic and Cardiovascular Surgery 135 (4), 816–822.

Norris, D. G., 2001. Implications of bulk motion for diffusion-weighted imaging experiments: Effects, mechanisms, and solutions. Journal of Magnetic Resonance Imaging 13 (4), 486–495.

Norris, D. G., Hutchison, J. M., 1990. Concomitant magnetic field gradients and their effects on imaging at low magnetic field strengths. Magnetic Resonance Imaging 8 (1), 33–37.

Ozaki, M., Inoue, Y., Miyati, T., Hata, H., Mizukami, S., Komi, S., Matsunaga, K., Woodhams, R., 2013. Motion artifact reduction of diffusion-weighted MRI of the liver: Use of velocity-compensated diffusion gradients combined with tetrahedral gradients. Journal of Magnetic Resonance Imaging 37 (1), 172–178.

Padhani, A. R., Liu, G., Mu-Koh, D., Chenevert, T. L., Thoeny, H. C., Takahara, T., Dzik-Jurasz, A., Ross, B. D., Van Cauteren, M., Collins, D., et al., 2009a. Diffusion-weighted magnetic resonance imaging as a cancer biomarker: consensus and recommendations. Neoplasia 11 (2), 102–125.

Padhani, A. R., Liu, G., Mu-Koh, D., Chenevert, T. L., Thoeny, H. C., Takahara, T., Dzik-Jurasz, A., Ross, B. D., Van Cauteren, M., Collins, D., et al., 2009b. Diffusion-weighted magnetic resonance imaging as a cancer biomarker: consensus and recommendations. Neoplasia 11 (2), 102–125.

Papoulis, A., 1977. Generalized sampling expansion. IEEE Transactions on Circuits and Systems 24 (11), 652–654.

Papoulis, A., Pillai, S. U., 2002. Probability, random variables, and stochastic processes. Tata McGraw-Hill Education.

Parikh, T., Drew, S. J., Lee, V. S., Wong, S., Hecht, E. M., Babb, J. S., Taouli, B., 2008. Focal liver lesion detection and characterization with diffusion-weighted MR imaging: comparison with standard breath-hold T2-weighted imaging. Radiology 246 (3), 812–822.

Park, B. K., Lee, H. M., Kim, C. K., Choi, H. Y., Park, J. W., 2008. Lesion localization in patients with a previous negative transrectal ultrasound biopsy and persistently elevated prostate specific antigen level using diffusion-weighted imaging at three Tesla before rebiopsy. Investigative Radiology 43 (11), 789–793.

Peña-Nogales, Ó., Ellmore, T. M., de Luis-García, R., Suescun, J., Schiess, M. C., Giancardo, L., 2019a. Longitudinal connectomes as a candidate progression marker for prodromal Parkinson's disease. Frontiers in Neuroscience 12, 967.

Peña-Nogales, Ó., Hernando, D., Aja-Fernández, S., de Luis-Garcia, R., 2020. Determination of optimized set of b-values for Apparent Diffusion Coefficient mapping in liver Diffusion-Weighted MRI. Journal of Magnetic Resonance 310, 106634.

Peña-Nogales, Ó., Zhang, Y., Wang, X., de Luis-Garcia, R., Aja-Fernández, S., Holmes, J. H., Hernando, D., 2019b. Optimized Diffusion-Weighting Gradient Waveform Design (ODGD) formulation for motion compensation and concomitant gradient nulling. Magnetic Resonance in Medicine 81 (2), 989–1003.

Planchuelo-Gómez, Á., García-Azorín, D., Guerrero, Á. L., Aja-Fernández, S., Rodríguez, M., de Luis-García, R., 2020. Structural connectivity alterations in chronic and episodic migraine: A diffusion magnetic resonance imaging connectomics study. Cephalalgia 40 (4), 367–383.

Poot, D. H., Arnold, J., Achten, E., Verhoye, M., Sijbers, J., 2010. Optimal experimental design for diffusion kurtosis imaging. IEEE Transactions on Medical Imaging 29 (3), 819–829.

Pruessmann, K. P., Weiger, M., Scheidegger, M. B., Boesiger, P., 1999. SENSE: sensitivity encoding for fast MRI. Magnetic Resonance in Medicine 42 (5), 952–962.

Purcell, E. M., Torrey, H. C., Pound, R. V., 1946. Resonance absorption by nuclear magnetic moments in a solid. Physical Review 69 (1-2), 37.

Ravi, K., Geethanath, S., Vaughan, J., 2019. PyPulseq: A Python Package for MRI Pulse Sequence Design. Journal of Open Source Software 4 (42), 1725.

Ravi, K. S., Potdar, S., Poojar, P., Reddy, A. K., Kroboth, S., Nielsen, J.-F., Zaitsev, M., Venkatesan, R., Geethanath, S., 2018. Pulseq-Graphical Programming Interface: Open source visual environment for prototyping pulse sequences and integrated magnetic resonance imaging algorithm development. Magnetic resonance imaging 52, 9–15.

Reese, T., Heid, O., Weisskoff, R., Wedeen, V., 2003. Reduction of eddy-current-induced distortion in diffusion MRI using a twice-refocused spin echo. Magnetic Resonance in Medicine 49 (1), 177–182.

Reilly, J. P., 1989. Peripheral nerve stimulation by induced electric currents: exposure to time-varying magnetic fields. Medical and Biological Engineering and Computing 27 (2), 101.

Roy, S., Carass, A., Bazin, P.-L., Resnick, S., Prince, J. L., 2012. Consistent segmentation using a Rician classifier. Medical Image Analysis 16 (2), 524–535.

Saritas, E. U., Lee, J. H., Nishimura, D. G., 2011. SNR dependence of optimal parameters for apparent diffusion coefficient measurements. IEEE Transactions on Medical Imaging 30 (2), 424–437.

Schulte, R. F., Noeske, R., 2015. Peripheral nerve stimulation-optimal gradient waveform design. Magnetic Resonance in Medicine 74 (2), 518–522.

Senegas, J., Perkins, T. G., Keupp, J., Stehning, C., Hussain, S., 2012. Organ-specific optimization of b-values for the simplified IVIM model of diffusion. In: Proceedings of the 29th ESMRMB - The European Society for Magnetic Resonance in Medicine and Biology. European Society for Magnetic Resonance in Medicine and Biology, p. 45196.

Shinya, S., Sasaki, T., Nakagawa, Y., Guiquing, Z., Yamamoto, F., Yamashita, Y., 2009. The efficacy of diffusion-weighted imaging for the detection and evaluation of acute pancreatitis. Hepato-gastroenterology 56 (94-95), 1407–1410.

Sica, C. T., Meyer, C. H., 2007. Concomitant gradient field effects in balanced steady-state free precession. Magnetic Resonance in Medicine 57 (4), 721–730.

Sijbers, J., den Dekker, A. J., Scheunders, P., Van Dyck, D., 1998. Maximum-likelihood estimation of Rician distribution parameters. IEEE Transactions on Medical Imaging 17 (3), 357–361.

Simonetti, O. P., Wendt, R. E., Duerk, J. L., 1991. Significance of the point of expansion in interpretation of gradient moments and motion sensitivity. Journal of Magnetic Resonance Imaging 1 (5), 569–577.

Smith, J. J., Sorensen, A. G., Thrall, J. H., 2003. Biomarkers in imaging: realizing radiology's future. Radiology 227 (3), 633–638.

Stejskal, E. O., Tanner, J. E., 1965. Spin diffusion measurements: spin echoes in the presence of a time-dependent field gradient. The Journal of Chemical Physics 42 (1), 288–292.

Stoeck, C. T., Von Deuster, C., Genet, M., Atkinson, D., Kozerke, S., 2016. Second-order motion-compensated spin echo diffusion tensor imaging of the human heart. Magnetic Resonance in Medicine 75 (4), 1669–1676.

Tan, E. T., Marinelli, L., Slavens, Z. W., King, K. F., Hardy, C. J., 2013. Improved correction for gradient nonlinearity effects in diffusion-weighted imaging. Journal of Magnetic Resonance Imaging 38 (2), 448–453.

Taouli, B., Beer, A. J., Chenevert, T., Collins, D., Lehman, C., Matos, C., Padhani, A. R., Rosenkrantz, A. B., Shukla-Dave, A., Sigmund, E., et al., 2016. Diffusion-weighted imaging outside the brain: Consensus statement from an ISMRM-sponsored workshop. Journal of Magnetic Resonance Imaging 44 (3), 521–540.

Taouli, B., Koh, D.-M., 2009. Diffusion-weighted MR imaging of the liver 1. Radiology 254 (1), 47–66.

Taouli, B., Vilgrain, V., Dumont, E., Daire, J.-L., Fan, B., Menu, Y., 2003. Evaluation of liver diffusion isotropy and characterization of focal hepatic lesions with two single-shot echo-planar MR imaging sequences: prospective study in 66 patients. Radiology 226 (1), 71–78.

Thunberg, P., Zetterberg, P., 2007. Noise distribution in SENSE-and GRAPPA-reconstructed images: a computer simulation study. Magnetic Resonance Imaging 25 (7), 1089–1094.

Trouard, T. P., Sabharwal, Y., Altbach, M. I., Gmitro, A. F., 1996. Analysis and comparison of motion-correction techniques in diffusion-weighted imaging. Journal of Magnetic Resonance Imaging 6 (6), 925–935.

Van den Bos, A., 2007. Parameter estimation for scientists and engineers. John Wiley & Sons.

Wang, X., Reeder, S. B., Hernando, D., 2017. An acetone-based phantom for quantitative diffusion MRI. Journal of Magnetic Resonance Imaging 46 (6), 1683–1692.

Weissenberger, V., Jan. 1 2002. Method of acquiring eddy currents that are caused by switched magnetic field gradients of a magnetic resonance apparatus and that contain cross-terms. US Patent 6,335,620.

Welsh, C. L., DiBella, E. V., Hsu, E. W., 2015. Higher-order motion-compensation for in vivo cardiac diffusion tensor imaging in rats. IEEE Transactions on Medical Imaging 34 (9), 1843–1853.

Woodhams, R., Matsunaga, K., Kan, S., Hata, H., Ozaki, M., Iwabuchi, K., Kuranami, M., Watanabe, M., Hayakawa, K., 2005. ADC mapping of benign and malignant breast tumors. Magnetic Resonance in Medical Sciences 4 (1), 35–42.

Wu, X., Bricq, S., Collet, C., 2011. Brain MRI segmentation and lesion detection using generalized Gaussian and Rician modeling. In: Medical Imaging 2011: Image Processing. Vol. 7962. International Society for Optics and Photonics, p. 796236.

Xing, D., Papadakis, N. G., Huang, C. L.-H., Lee, V. M., Carpenter, T. A., Hall, L. D., 1997. Optimised diffusion-weighting for measurement of apparent diffusion coefficient (ADC) in human brain. Magnetic Resonance Imaging 15 (7), 771–784.

Xu, D., Maier, J. K., King, K. F., Collick, B. D., Wu, G., Peters, R. D., Hinks, R. S., 2013. Prospective and retrospective high order eddy current mitigation for diffusion weighted echo planar imaging. Magnetic Resonance in Medicine 70 (5), 1293–1305.

Yamada, I., Aung, W., Himeno, Y., Nakagawa, T., Shibuya, H., 1999. Diffusion coefficients in abdominal organs and hepatic lesions: evaluation with intravoxel incoherent motion echo-planar MR imaging. Radiology 210 (3), 617–623.

Zhang, B., Yen, Y.-F., Chronik, B. A., McKinnon, G. C., Schaefer, D. J., Rutt, B. K., 2003. Peripheral nerve stimulation properties of head and body gradient coils of various sizes. Magnetic Resonance in Medicine 50 (1), 50–58.

Zhang, J. L., Sigmund, E. E., Rusinek, H., Chandarana, H., Storey, P., Chen, Q., Lee, V. S., 2012. Optimization of b-value sampling for diffusion-weighted imaging of the kidney. Magnetic Resonance in Medicine 67 (1), 89–97.

Zhang, Y., Peña-Nogales, Ó., Holmes, J. H., Hernando, D., 2019. Motion-robust and blood-suppressed M1-optimized diffusion MR imaging of the liver. Magnetic Resonance in Medicine 82 (1), 302–311.

Zhou, X., Jun. 23 1998. Method for measuring and compensating for spatially and temporally varying magnetic fields induced by eddy currents. US Patent 5,770,943.

Zhou, X., Maier, J. K., Reynolds, H. G., Jan. 26 1999. Method to reduce eddy current effects in diffusion-weighted echo planar imaging. US Patent 5,864,233.

Zhou, X. J., Tan, S. G., Bernstein, M. A., 1998. Artifacts induced by concomitant magnetic field in fast spin-echo imaging. Magnetic Resonance in Medicine 40 (4), 582–591.